

**Quantitative analysis of Förster resonance energy transfer
from spectrally resolved fluorescence measurements**

PhD Thesis

in partial fulfilment of the requirements
for the degree “Doctor of Philosophy (PhD)”
in the Neuroscience Program
at the Georg August University Göttingen,
Faculty of Biology

submitted by

Andrew T. Woehler

born in

Phoenix, Arizona, USA

Goettingen, 2010

Supervisor, PhD committee member: Prof. Dr. Erwin Neher

Supervisor, PhD committee member: Prof. Dr. Evgeni Ponimaskin

PhD committee member: Prof. Dr. Dr. Detlev Schild

Date of submission of the PhD thesis: March 17, 2010

I hereby declare that I prepared this PhD thesis, entitled “Quantitative analysis of Förster resonance energy transfer from spectrally resolved fluorescence measurements”, on my own and with no other sources and aids than those cited.

Andrew T. Woehler
Göttingen, March 17, 2010

To my parents and grandparents

Contents

1	Introduction	1
1.1	Description of fluorescence	1
1.2	General description of FRET.....	3
1.3	Development of Förster’s theories	6
1.4	Methods in FRET analysis.....	8
1.4.1	Analysis of donor fluorescence lifetime.....	8
1.4.2	Steady state fluorescence	9
1.5	Aim of the study.....	11
1.6	Theoretical considerations.....	12
1.6.1	Generalized solution for apparent FRET efficiency from spectral measurements	12
1.6.2	Considerations for incomplete labeling	18
1.6.3	Application to microscopy - alternative analysis modes	19
1.6.4	Noise propagation.....	20
2	Materials and Methods.....	25
2.1	Cell culture and transient transfection	25
2.2	Fluorescence spectroscopy.....	25
2.3	Cell lysate preparation and pH titration	26
2.4	Fluorescence lifetime FRET measurements.....	26
2.5	Imaging setup.....	27
2.6	Live cell imaging	27
2.7	lux-FRET image analysis	28
2.8	Determination of apparent single photon signal.....	29
3	Results.....	30
3.1	Calibrations for luxFRET measurements	30
3.2	Determination of FRET efficiency	32
3.3	Influence of fractional occupancy and partial acceptor photobleaching	35
3.4	pH sensitivity of YFP and its influence on FRET analysis.....	37
3.5	Identification of intermolecular interaction	39
3.6	Spectral imaging and implementation of luxFRET to microscopy	41
3.7	Analog detector calibration - determination of apparent single photons signal	45
3.8	Characterization of noise in unmixed apparent concentrations	48
3.9	Use of error propagation to predict SNR^2 of FRET estimators.....	51
3.9.1	FRET imaging of an Epac-based cAMP sensor.....	51

3.9.2 Dependence of SNR^2 of FRET estimators on the number of detected photons & FRET efficiency	54
3.9.3 Time series measurements of select FRET estimators	57
3.9.4 Effect of FRET change and bleaching on E_{p_a} and its SNR^2	58
3.9.5 Estimation of Ligand concentration	59
3.9.6 Biasing resulting from Error propagation	62
3.9.7 Comparison of dynamic range to noise	65
3.10 Optimization of additional imaging parameters.....	67
3.10.1 Optimal localization of emission channel boundaries.....	67
3.10.2 Optimization of excitation wavelengths.....	71
4 Discussion.....	75
4.1 Implementation and validation of a novel spectral FRET method	75
4.2 Considerations for fluorophore bleaching and protonation	76
4.3 Identification of intermolecular interaction	78
4.4 Application to microscopy and consideration for noise propagation	81
4.5 Optimization of spectral resolution and excitation wavelength	86
5 Summary	91
6 References	94
7 Appendices.....	100
7.1 Appendix 1 – Abbreviations and symbols.....	100
7.2 Appendix 2 – Full derivation of error propagation equations	102
Acknowledgements.....	106
Curriculum Vitae	107

1 Introduction

Förster resonance energy transfer (FRET) is a physical process in which the excited state energy of a chromophore molecule is non-radiatively transferred to a neighboring chromophore while in its ground state. This physical process is often used in experimental methods which aim at investigating the interaction of molecules at distances beyond diffraction limited resolution. Several experimental methods utilizing FRET have become invaluable tools for the analysis of interactions among biological molecules. These methods, generally applied to spectroscopy and microscopy, allow for the investigation of the formation of protein complexes as well as conformation changes of single proteins. Accordingly FRET methods have been used in the characterization of spatial and temporal dynamics of a large number of cellular signaling processes.

1.1 Description of fluorescence

Although fluorescence is not required for the FRET to occur, the experimental methods which take advantage of FRET generally involve fluorescence or some luminescent process. Luminescence is the emission of light (photons) resulting from the relaxation of a system from an excited state to its ground state. If the transition occurs for an electron in the excited singlet state (with spin opposite of that of a paired electron in the ground state), the emission is denoted as fluorescence. If this transition occurs from an excited triplet state, in which the spin of the electron matches that of the paired ground state electron, the emission is known as phosphorescence.

Fluorescence often occurs in aromatic molecules (generally molecules with a closed loop of electrons with $4n+2$ pi-electrons) (Lakowicz 2006). Subsequent to the absorption of the energy of an incident photon by the molecule, numerous processes can occur. Often times the fluorescent molecule is excited to either the S_1 or S_2 excited state. In most cases there is rapid relaxation to the lowest vibrational level of the first excited state, a process known as internal conversion. This process usually occurs on the order of 10^{-12} s and results in some of the energy loss from the system

responsible for the energy difference (Stokes' Shift) between the absorption and emission spectra. The transition to the ground state from the first excited state occurs on the order 10^{-9} s and can result in the emission of a photon. The energy of the emitted photon is dependent upon the vibration level of the ground state to which the transition occurs. The spacing of vibrational levels at the S_0 and S_1 levels is similar and responsible for the mirroring of absorption and emission spectra.

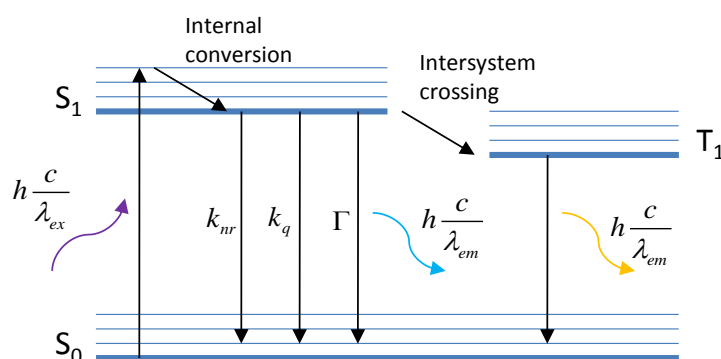


Figure 1.1 | Jablonski diagram. This diagram illustrates the ground, S_0 , and first excited state, S_1 , of a molecule. Upon absorption of the energy of an incident photon, hc/λ , or from some other source, the molecule transitions to an excited state. There is internal conversion of energy and relaxation to the lowest vibrational level of the first excited state. From S_1 there are multiple de-excitation pathways including, the emission of a photon, collisional quenching, spin conversion to triplet state, T_1 , and other non-radiative processes (adapted from Lakowicz 2006).

Additionally, the excited state molecule can undergo a spin conversion, leading to intersystem crossing to the first triplet state. Relaxation from the first triplet state to the ground state, phosphorescence, generally occurs on the order of ms - s and can result in the emission of a photon at longer wavelength. This is due to the additional energy loss from the system resulting from intersystem crossing and additional vibrational relaxation. It is possible for relaxation also to occur through non-radiative processes such as collisional quenching. The Jablonski diagram shown in figure 1.1 illustrates the balance of energy throughout the excitation - relaxation cycle. The energy absorbed from an incident photon, hc/λ_{ex} , is eventually used through the emission of a photon the emitted photon, hc/λ_{em} , heat exchange from internal conversion, or other non-radiative processes.

Each of these processes has a rate or probability at which it occurs which is used to determine the efficiency of that process, i.e. quantum yield.

1.2 General description of FRET

FRET poses an additional possible relaxation pathway for an excited state molecule, which only under certain conditions becomes available. First, this form of energy transfer occurs in the near field, non-radiatively. In order for this pathway to be available, the distance between the excited molecule and a suitable partner must be on the order of hundreds of angstroms. Secondly, as the acronym suggests, the transfer of energy is achieved between molecules with resonant oscillation dipole moments (overlapping wave functions). This requires that the emission spectrum of the energy donating molecule (from here on denoted as the 'donor') must overlap with the excitation spectrum of the energy accepting molecule (hence forth denoted as 'acceptor'). The last criterion which must be fulfilled in order for resonant energy transfer to occur, is that the emission dipole moment of the donor must be appropriately oriented with the excitation dipole moment of the acceptor.

The efficiency with which energy transfer occurs can be defined as the ratio of the relaxation rate due to energy transfer divided by the sum of all relaxation rates.

$$E = \frac{k_T(r)}{\tau_D^{-1} + k_T(r)} \quad 1.1$$

The rate of energy transfer is often defined as a function of inverse sixth power of distance between the two molecules.

$$k_T(r) = \frac{1}{\tau_D} \left(\frac{R_0}{r} \right)^6 \quad 1.2$$

In the above equations, τ_D is the excited state lifetime of the donor (in absence of acceptor) and R_0 is the Förster radius. This constant represents the distance between the two molecules at which the

efficiency of energy transfer is 50% (or when the rate of energy transfer is equal to the rate of fluorescence). Using equations 1.1 and 1.2, the transfer efficiency can be defined as a function of the Förster constant and the interaction distance.

$$E = \frac{R_0^6}{R_0^6 + r^6} \quad 1.3$$

This relationship can easily be used to estimate the distance of interaction from a measured FRET efficiency if the Förster radius is known.

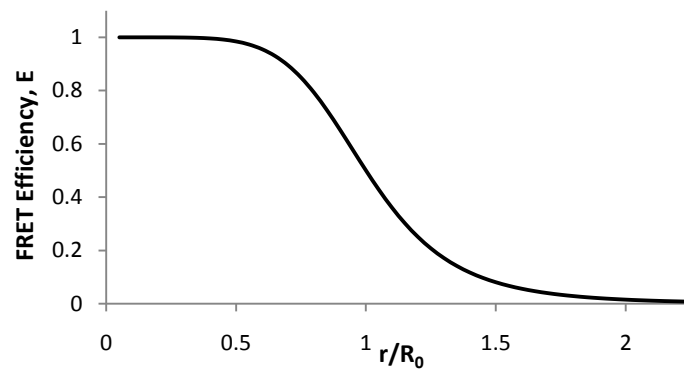


Figure 1.2 | FRET efficiency as a function of interaction distance. The FRET efficiency, E , can be characterized as a function of the interaction distance r by eq. 1.3. In this figure the r is normalized to the Förster radius, R_0 , such that FRET efficiency is equal to 50% when this ratio equals 1.

The Förster radius is defined as

$$R_0^6 = \frac{9000(\ln 10)\kappa^2 Q_D}{128\pi^5 N n^4} \cdot J(\lambda) , \quad 1.4$$

where Q_D is the donor quantum efficiency, N is the Avogadro constant, n is the refractive index of the medium, κ^2 is the orientation factor and $J(\lambda)$ is the donor emission / acceptor excitation spectral overlap.

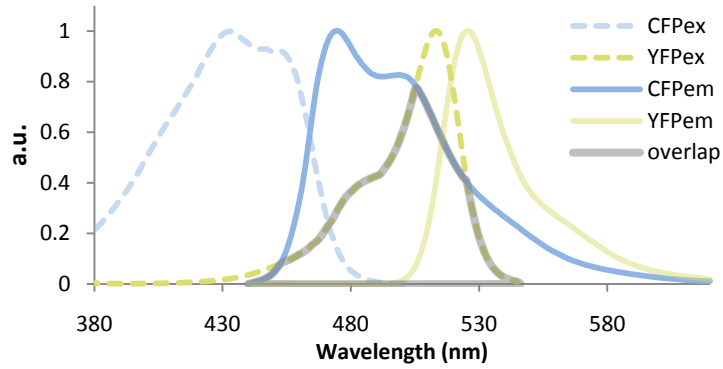


Figure 1.3 | Overlap Integral. The overlap between the normalized donor emission spectra and the acceptor excitation spectra characterized by eq. 1.5 is bound by the grey semi-transparent line.

The overlap integral $J(\lambda)$ illustrated above, can be calculated as

$$J(\lambda) = \int_0^{\infty} F_D(\lambda) \varepsilon_A(\lambda) \lambda^4 d\lambda . \quad 1.5$$

The orientation factor, κ^2 , is dependent upon the relative orientation of the donor emission dipole moment with the acceptor excitation dipole moment and can have a value of 0 to 4.

$$\kappa^2 = (\cos \theta_T - 3 \cos \theta_D \cos \theta_A)^2 = (\sin \theta_D \sin \theta_A \cos \phi - 2 \cos \theta_D \cos \theta_A)^2 \quad 1.6$$

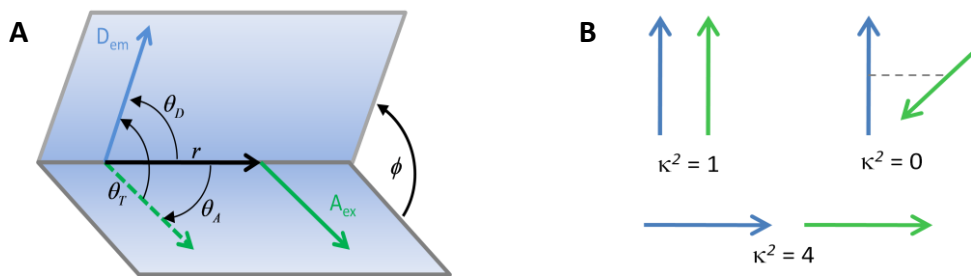


Figure 1.4 | Characterization of the orientation factor k^2 . The relative orientation of the donor emission dipole moment and the acceptor excitation dipole moment affects the Förster radius of a given FRET pair. A) The orientation factor k^2 is defined by eq. 1.6 with the characterizes the relative orientation as functions of the angles between the moments. B) The value of k^2 ranges from 0 to 4, with perfectly aligned dipole moments resulting in a factor of 4, parallel moments, 1, and orthogonal moments resulting in k^2 equal to 0. (Adapted from Lakowicz 2006).

The efficiency of energy transfer between the two molecules is dependent on the degree to which the mentioned criteria are fulfilled. The spectral overlap is generally a constant. Certain assumptions regarding the rotational freedom of the molecules are usually applied so that an average orientation factor can be estimated (i.e. $k^2 = 2/3$ for a system with completely randomized orientation) (Eisinger and Dale 1974; Dale et al. 1979). The efficiency of energy transfer, measured experimentally through various fluorescence and/or luminescence techniques, is most often used to estimate the distance of interaction or at least to distinguish between two states with different interaction distances and/or orientations.

1.3 Development of Förster's theories

Often times the acronym FRET is designated as fluorescence resonance energy transfer (Sekar and Periasamy 2003; Ponsioen et al. 2004). Some argue that this is justified when describing an experimental method using fluorescence methods to assay FRET (Van Der Meer 1994). In the context of this thesis, however, the acronym FRET will be used to describe the physical process of resonance energy transfer characterized by Förster and care will be given to distinguish this from the experimental methods in which it is used. Emphasis is given to this nomenclature to give credit where credit is due and to recognize the contributions made by Theodor Förster, not only for his quantitative treatment which characterizes FRET but also in the development of its use in experimental methods (Clegg 1996).

While emphasizing the importance of appropriately recognizing the important contributions to this field, it is essential also to discuss several of the foundations of fluorescence and even energy transfer upon which Förster's work was based. The first few reports of energy transfer at distances larger than those expected for collisional processes were reported up to two decades before Förster's work. In 1922, Cario and Frank observed sensitized emission in a Thallium – Mercury vapor (Cario and Franck 1922). Their work indicated that when mercury vapor was excited at 253nm and emission from Thallium was measured, that the radius of interaction was larger than the

spectroscopic cross section predicted by the theories of gas dynamics (Cario and Franck 1922; Clegg 2006). Concurrent to these measurements others reported measuring concentration dependent decreases in the polarization of fluorescence emission from molecules in solution. Interestingly the intensity of the fluorescence emission was not quenched and continued to increase linearly with concentration (Weigert 1920; Gaviola and Pringesheim 1924).

In 1925 Jean-Baptiste Perrin used classical mechanics to develop a model explaining the observations of concentration dependent fluorescence polarization in a condensed system (Perrin 1926). He concluded that energy transfer could be non-radiative. However, his theory required exact resonance, a criteria which would later prove impractical. Soon after, Kallmann and London provided a theoretical framework to explain the observations of energy transfer in atomic vapors based on quantum mechanics (Kallmann and London 1928). Kallmann and London's treatment included the $1/r^6$ relationship however, their work focused on the cross section of fluorophores they were studying. Based on the work performed by Kallman and London, Francis Perrin provided a description of energy transfer in condensed systems based on quantum mechanics (Perrin 1933). Similarly to the work of his father however, F. Perrin's treatment required that the two oscillating dipoles be in exact resonance. This resulted in the same $1/r^3$ dependence of efficiency, which resulted in interaction distances that they themselves pointed out were known to be too large.

Theodor Förster became interested in energy transfer because of the high efficiency of energy transfer during photosynthesis (Clegg 1996). By the time Förster began his work on energy transfer quantum mechanics had become well established. Förster was well acquainted with the relatively new theories and was familiar with the work of the Jean and Francis Perrin. In his first few papers dealing with FRET, Förster reviewed the theoretical background of FRET and the mechanisms previously proposed, and most importantly proposed several additions which served to complete a quantitative theory of FRET (Förster 1946; Förster 1948; Förster 1993; Clegg 1996; Clegg 2006). Most importantly he corrected the previous requirement of exact resonance. He realized that the

interaction of oscillating dipoles responsible for energy transfer was similar to the excitation transition dipole in the oscillating electric field of an incident photon. He compensated for the expected frequency spread that the Perrin's had neglected, by calculating the probability that the donor frequency was suitable for acceptor excitation (spectral overlap). He then multiplied this probability by the probability that the energy of interaction was within this range. This resulted in a rate of energy transfer with a $1/r^6$ dependency and half transfer interaction distances on the order of several nanometers (Förster 1946; Clegg 2006). He later published derivations in which he used quantum mechanics to arrive at the same solution (Förster 1948; Clegg 2006).

1.4 Methods in FRET analysis

1.4.1 Analysis of donor fluorescence lifetime

Among the most direct ways of measuring FRET is to measure the excited state lifetime of a molecule. In the case that energy transfer occurs, an additional relaxation pathway becomes available, resulting in a reduced excited state lifetime. Several procedures have been described in which FRET efficiency, and/or the relative abundance of donor-acceptor complexes are quantified through the analysis of donor fluorescence lifetimes (Gadella and Jovin 1995; Ng et al. 1999; Gerritsen et al. 2002; Tramier et al. 2003; Becker et al. 2004; Peter et al. 2005; Wallrabe and Periasamy 2005). Generally the measurement of fluorescence lifetime is accomplished in two ways (fig. 1.5). In the first method, a short excitation pulse excites a fluorescent sample. The time between the excitation pulse and the arrival of the first emitted photon is measured and the process repeated. A histogram of photon arrival times is collected and using Poisson statistics the fluorescent lifetime computed as the decay constant of an exponential fit. This method, time correlated single photon counting (TCSPC), is fast in that it requires measuring events occurring on the nanosecond scale sometimes with resolution on the order of tens of picoseconds. However, the time required to gather enough information to build the appropriate statistics (i.e. photon arrival histogram), often limits the use of these methods when investigating dynamic events in live cells.

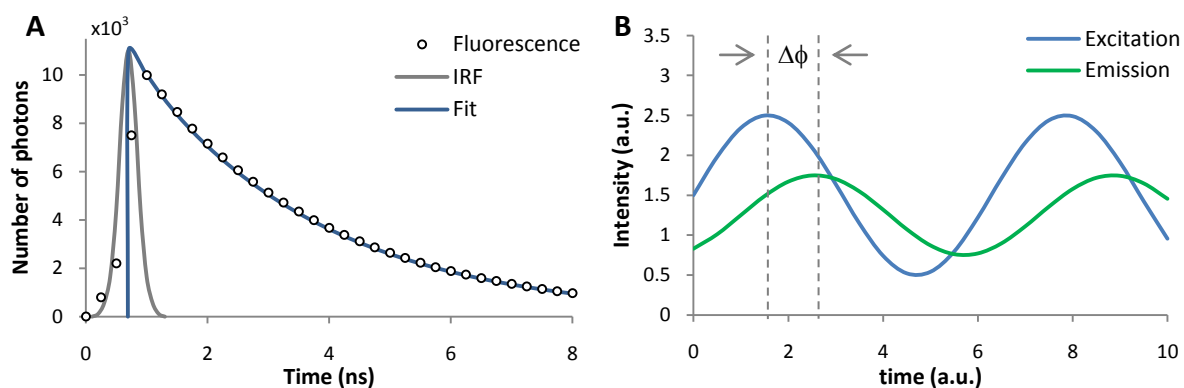


Figure 1.5 | Methods for measuring fluorescent lifetimes. A) Time correlated single photon counting is used to create a histogram of arrival times of leading photons, represented by the open circles, following a pulsed excitation. The fit to the measured decay represented by the blue curve is often created through the convolution of an exponential function with the instrument response function represented by the gray trace. B) The fluorescent sample is excited with a modulated source. This results in a modulated in the emission. The phase shift between the two signals, as well as their demodulation, can be used to determine the fluorescence lifetime.

A second popular method to determine the fluorescence lifetime uses an amplitude modulated excitation source and records similarly modulated emission from the sample. A lock-in amplifier is used to determine the phase shift between the two signals. This phase shift can then be used to determine the fluorescence lifetime. Additional information can be retrieved from measuring the relative changes in the amplitude of the collected emission signal.

1.4.2 Steady state fluorescence

While fluorescence lifetimes measurements obtain information regarding the depopulation rate of the donor excited state which can be used to measure FRET, there are many methods which use only the intensity of emission. These methods generally come in two flavors. Measurements of donor quenching compare the intensity of the quenched donor to that of the free, unquenched donor. One problem which arises with these measurements is the requirement of equimolar samples. This is less of a problem for in-vitro investigations where donor absorption can be used to measure concentration; however ensuring equal concentration in-vivo is not trivial. One way in which this problem has been addressed is to perform a measurement of fluorescence of donor in presence of acceptor and then essentially remove the acceptor molecules from the system through

photobleaching (Wouters et al. 1998; Llopis et al. 2000; Kenworthy 2001; Lippincott-Schwartz et al. 2001). Acceptor photobleaching is a well established method for identifying FRET and even quantifying it in the case of known expression ratios (i.e. tandem constructs)(Gu et al. 2004). Unfortunately this method is destructive and thus often can only be used once per sample, making it impractical for measurements of dynamic processes. Adaptations of this method using photo-switchable acceptors have provided the possibility for repeated measurements (Giordano et al. 2002; Song et al. 2002). These methods require the use of additional excitation wavelengths for photo-activation of bleached species. If an additional wavelength and filter set is to be used, there are other, possibly more favorable methods which can be utilized and will be discussed later. Furthermore, this general approach does not provide any quantitative information regarding the expression ratio of the donor and acceptor molecules, so its use in quantitative intermolecular FRET is limited.

The other approach often used in measuring FRET from steady state emission intensity is to measure changes in acceptor intensity resulting from sensitized emission. These methods compare the intensity of acceptor when, preferably, only donor is excited, to the intensity of the acceptor when it is directly excited. These methods rarely aim at quantifying the efficiency of energy transfer but rather identifying FRET. These methods often implement different corrections for simultaneous excitation of donor and acceptor molecules (excitation crosstalk) and donor emission bleed through into the acceptor channel (Graham et al. 2001). Several methods also consider various normalizations for fluorophore concentration (Youvan 1997; Sorkin et al. 2000; Xia and Liu 2001; Hailey et al. 2002; Zal and Gascoigne 2004). These methods are reviewed in more detail in Berny et al 2003 and are shown to be nonlinearly dependent with respect to both FRET efficiency and fractional labeling by Hoppe et al 2002.

Several methods have been proposed which not only have the ability to measure apparent FRET but also quantify the fractional abundances of the donor and acceptor molecules (Hoppe et al.

2002; Thaler et al. 2005; Chen et al. 2006; Meyer et al. 2006; Wlodarczyk et al. 2008). These measurements are generally performed by exciting the sample at two different wavelengths and measuring fluorescence in at least two spectral windows. Whenever any unpaired or self associated donor and acceptor molecules are present in a FRET sample, such methods do not provide absolute values for the FRET efficiency, E . Rather, these methods quantify the product of the efficiency of energy transfer E and the fractional occupancies, f_D and f_A . We denote these quantities as apparent FRET efficiencies.

1.5 Aim of the study

In this study, yet another spectral FRET method will be presented. It will be demonstrate that this method can accurately measure the apparent FRET efficiency and stoichiometry of donor and acceptor molecules present in a sample. It will be shown that these quantities can be derived from equations which describe all the factors which contribute to the emission spectra of a fluorescent sample composed of both free and interacting donor and acceptor molecules. Initial implementation of this method to spectroscopy will be demonstrated. The efficacy of the method will be evaluated through the use of CFP-YFP tandem construct as a FRET standard and comparison of results with established methods. It will be shown that the additional information that this method provides allows for the correction of two of the most common sources of artifacts in FRET measurements, photobleaching and fluorophore protonation. Furthermore the application of this method to quantitatively evaluate intermolecular interaction will be presented.

Next the application of this method to microscopy will be addressed. With the transition to microscopy other considerations must be made. Different analysis modes will be derived such that quantitative measurements can be performed on ranging microscope configurations. In the transition to microscopy, the SNR of the measurements and propagation of photon shot noise will also be considered. Models will be developed for the various proposed analysis modes to characterize the SNR as a function of the number of collected photon during each excitation and the

FRET efficiency. These models will be used to optimize efficient photon use within dual excitation measurements. Furthermore the application of this method to dynamic measurements of FRET changes will be presented. The ability of the developed models to predict the SNR of the FRET estimators due to changes in the number of collected photons as well as changes in FRET efficiency will be demonstrated. The different analysis modes will be compared and the mode which provides the best sensitivity to changes in FRET will be identified.

Simulations will be performed such that additional imaging parameters, including the two wavelengths at which the sample is excited and the placement and resolution of spectral channels from which emission is collected, can be optimized. Combined, these investigations aim at defining the type of information that can be gathered from a FRET system with this method, how well this method performs at quantifying this information compared to other methods, and the minimal requirements for its implementation.

1.6 Theoretical considerations

1.6.1 Generalized solution for apparent FRET efficiency from spectral measurements

Several recent studies have used two excitation wavelength measurements of fluorescence intensity to address the problem of determining the apparent FRET efficiency, Ef_D or Ef_A . (Erickson et al. 2001; Hoppe et al. 2002; Chen et al. 2006; Meyer et al. 2006). Aside from the short comings of exhaustive calibrations and requirement of, sometimes multiple, known FRET reference which will be discussed later, these studies often use exclusive notation which makes comparison between the quantities and evaluation of underlying assumptions difficult. In the following, the collaborative work presented in Wlodarczyk et al. 2008 is recapitulated. Here we introduce yet another notation is used when addressing the problem of quantifying apparent FRET efficiencies from spectral measurements. This notation, however, is similar to that used in spectroscopy (Lakowicz 2006) and, as we will show, allows us to address the problem in a rather generalized manner. That is to say the

relationships presented here have cross-platform application and are less constrained than those presented in previous studies.

To begin we provide a general definition of fluorescence emission from fluorophore C,

$$F_C^i(\lambda) = I^i \varepsilon_C^i Q_C \eta^i(\lambda) e_C(\lambda) [C] \quad 1.7$$

where I^i is the excitation intensity at wavelength i , ε_C^i is the extinction coefficient at wavelength i , Q_C is the quantum efficiency of fluorophore C, $\eta^i(\lambda)$ is the device response function (i.e. detection efficiency), $e_C(\lambda)$ is the characteristic emission spectra of the fluorophore (can be considered as probability density function of emission wavelength), and $[C]$ is the concentration of fluorophore.

In the case of multiple fluorescent species, the fluorescence emission is the linear superposition of the individual emission spectra.

$$F_{C_{1...j}}^i(\lambda) = \sum_{n=1}^j I^i \varepsilon_{C_n}^i Q_{C_n} \eta^i(\lambda) e_{C_n}(\lambda) [C_n] \quad 1.8$$

We now consider the case in which resonance energy transfer occurs. Figure 1.6 provides an illustration of an experimental system in which FRET may be utilized. In this example we have two proteins of interest, or interactors, which can be present either as individual molecules at chemical concentrations $[d]$ and $[a]$ or as a complex at chemical concentration $[da]$. We distinguish between the actual chemical concentrations of the interactors, $[d]$ and $[a]$, and the apparent concentrations $[D]$ and $[A]$ of the fluorescent labels, so that we may later address the possibility of incomplete labeling of the interactors.

Figure 1.6 part B illustrates the contributions to fluorescence which we would detect. There can be considered to be five separate sources of fluorescence emission, two of which have donor emission characteristics (contributions from free and the partially quenched interacting donor). The remaining three contributions have acceptor emission characteristics and arise from the direct

excitation of free acceptor, the direct excitation of interacting acceptor and from sensitized emission from donor.

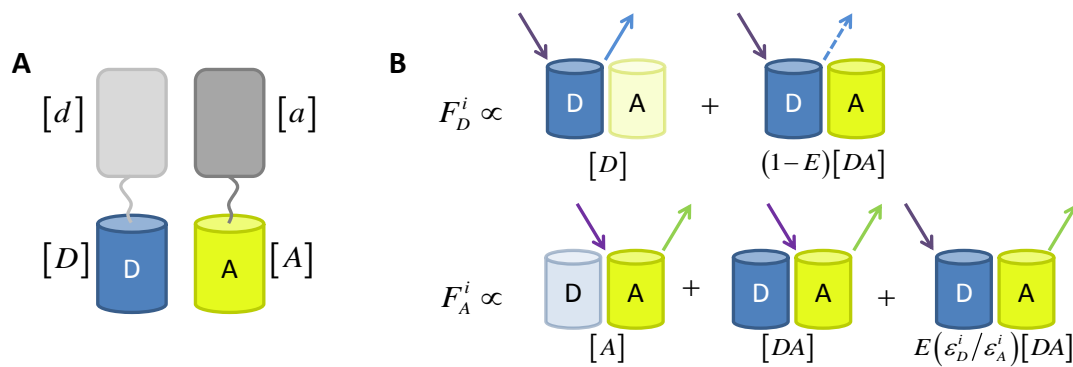


Figure 1.6 | Nomenclature and fluorescence properties of interacting molecules. A) In the case of investigating intermolecular FRET we have two labeled interactors present at chemical concentrations $[d]$ and $[a]$ but detected at apparent concentrations $[D]$ and $[A]$, respectively. B) The fluorescence detected in such a case is the sum of 5 contributions; direct excitation of free donor, direct excitation of partially quenched interacting donor, direct excitation of free acceptor, direct excitation of interacting acceptor, and from sensitized acceptor emission.

Taking these sources of fluorescence into consideration we can characterize the total detected fluorescence from a measured FRET sample as,

$$F^i(\lambda) = I^{(i)}\eta^{(i)}(\lambda) \left(\epsilon_D^{(i)} Q_D e_D(\lambda) ([D] + (1-E)[DA]) + \epsilon_A^{(i)} Q_A e_A(\lambda) \left([A] + \left(1 + E \frac{\epsilon_D^{(i)}}{\epsilon_A^{(i)}} \right) [DA] \right) \right). \quad 1.9$$

From samples expressing exclusively donor and acceptor molecules we can define reference spectra as

$$F_D^{i,ref}(\lambda) = I^{i,ref} \epsilon_D^{(i)} Q_D \eta^{(i)}(\lambda) e_D(\lambda) [D^{ref}] \quad 1.10$$

and

$$F_A^{i,ref}(\lambda) = I^{i,ref} \epsilon_A^{(i)} Q_A \eta^{(i)}(\lambda) e_A(\lambda) [A^{ref}]. \quad 1.11$$

Using the reference spectra we can eliminate the common constants and spectral parameters in eq. 1.9 and obtain:

$$F^i(\lambda) = \frac{I^i}{I^{i,ref}} \left(F_D^{i,ref}(\lambda) \frac{([D] + (1-E)[DA])}{[D^{ref}]} + F_A^{i,ref}(\lambda) \frac{([A] + (1+E \varepsilon_D^{(i)}/\varepsilon_A^{(i)})[DA])}{[A^{ref}]} \right). \quad 1.12$$

The emission spectra from a sample containing both donor and acceptor molecules can be described as a linear combination of the respective reference spectra,

$$F^i(\lambda) = \delta^{i*} F_D^{i,ref}(\lambda) + \alpha^{i*} F_A^{i,ref}(\lambda). \quad 1.13$$

Comparing Eq.1.12 with 1.13 we note that

$$\delta^{(i)*} = \frac{I^i}{I^{i,ref}} \frac{([D] + (1-E)[DA])}{[D^{ref}]} \quad \text{and} \quad \alpha^{(i)*} = \frac{I^i}{I^{i,ref}} \frac{([A] + (1+E \varepsilon_D^i/\varepsilon_A^i)[DA])}{[A^{ref}]}. \quad 1.14,1.15$$

We denote δ^i and α^i (scaled δ^{i*} and α^{i*} to correct for $I^i/I^{i,ref}$) as apparent relative acceptor and donor concentrations, respectively. With two measurements, at different excitation wavelengths, eqs. 1.14 and 1.15 represent three independent equations. These equations describe four unknown quantities of interest, [D], [A], [DA] and E. It should be noted that Eq. 1.14 does not include any wavelength dependent parameters (i.e. extinction coefficients) and thus is identical at different excitation wavelengths. Although we cannot solve for all unknown quantities, we can define three of the quantities of interest as functions of the fourth, such that,

$$[D] = [D^{ref}] \left(\delta^{(1)} - \frac{\Delta\alpha}{\Delta r} \frac{1-E}{E} \right), \quad 1.16$$

$$[A] = \frac{[A^{ref}]}{\Delta r} \left(\alpha^{(2)} r^{ex,1} - \alpha^{(1)} r^{ex,2} + \frac{\Delta\alpha [D^{ref}]}{E [A^{ref}]} \right), \quad 1.17$$

$$[DA] = [D^{ref}] \frac{\Delta\alpha}{E \Delta r}. \quad 1.18$$

Where

$$\Delta\alpha = \alpha^{(2)} - \alpha^{(1)}, \quad 1.19$$

$$\Delta r = r^{ex,2} - r^{ex,1}, \quad 1.20$$

with,

$$r^{ex,i} = \frac{\varepsilon_D^{(i)} [D^{ref}]}{\varepsilon_A^{(i)} [A^{ref}]} \quad 1.21$$

$r^{ex,i}$ is a calibration constant which is empirically determined and will be discussed later. Eqs. 1.16 and 1.17 can be combined with 1.18 such that E cancels out and we are left with equations describing the total FRET corrected concentration of donor and acceptor molecules.

$$[D^t] \equiv [D] + [DA] = [D^{ref}] \left(\delta^{(1)} + \frac{\Delta\alpha}{\Delta r} \right), \quad 1.22$$

$$[A^t] \equiv [A] + [DA] = [A^{ref}] \frac{\left(\alpha^{(1)} r^{ex,2} - \alpha^{(2)} r^{ex,1} \right)}{\Delta r} \quad 1.23$$

The product of E[DA] derived from eq. 1.18 is divided by the total concentrations to arrive at definitions for the apparent FRET efficiencies,

$$Ef_D \equiv E \frac{[DA]}{[D^t]} = \frac{\Delta\alpha}{\Delta r \delta^{(1)} + \Delta\alpha}, \quad 1.24$$

$$Ef_A \equiv E \frac{[DA]}{[A^t]} = \frac{[D^{ref}]}{[A^{ref}]} \frac{\Delta\alpha}{\alpha^{(1)} r^{ex,2} - \alpha^{(2)} r^{ex,1}} \quad 1.25$$

These apparent FRET efficiencies, Ef_D and Ef_A , correspond to estimates measured from donor quenching and from acceptor sensitization, respectively. E is the characteristic FRET efficiency and f_D and f_A represent the fractions of donor and acceptor molecules participating in FRET complexes (fractional occupancies).

Using the definitions for the FRET corrected total concentrations, Eqs. 1.22 and 1.23, we can define the corrected total acceptor to total donor concentration as,

$$R^t \equiv \frac{[A^t][D^{ref}]}{[D^t][A^{ref}]} = \frac{\alpha^{(1)} r^{ex,2} - \alpha^{(2)} r^{ex,1}}{\Delta r \delta^{(1)} + \Delta\alpha} \quad 1.26$$

These three equations (1.24-1.26) which allow one to quantify the donor quenching related and acceptor sensitization related apparent FRET efficiencies as well as the corrected concentration ratio contain two quantities that must be determined empirically through calibration measurements. First, the excitation ratio $r^{ex,i}$ (Eq. 1.21), which describes the ratio of extinction coefficient of our donor and acceptor molecules at excitation wavelength i , must be determined through the use of the four reference spectra measured from the samples containing exclusively donor and acceptor molecules. By multiplying the unit area normalized emission spectra (characteristic spectra) by the corresponding donor or acceptor quantum efficiencies, $Q_{CFP}0.40$ (Patterson et al. 2000) and $Q_{YFP}0.61$ (Su 2005), the spectral probability distributions of emission for an excited donor or acceptor molecule can be determined. By dividing a reference measurement by the corresponding donor or acceptor probability distribution we can determine a quantity proportional to the number excitation events occurring during the measurement. This quantity is also proportional to the extinction coefficient and the respective donor or acceptor concentration present in the reference sample. By dividing this quantity for the donor by that of the acceptor, we can cancel out the common spectral parameters and determine $r^{ex,i}$.

$$r^{ex,i} = \frac{F_D^{i,ref}(\lambda) \cdot Q_A e_A(\lambda)}{Q_D e_D(\lambda) \cdot F_A^{i,ref}(\lambda)} = \frac{\varepsilon_D^{(i)} [D^{ref}]}{\varepsilon_A^{(i)} [A^{ref}]} \quad 1.27$$

Additionally, we see that the total concentration ratio, eq. 1.26, and the acceptor dependent apparent FRET efficiency, eq. 1.25 are scaled by a reference concentration ratio. This missing piece of information can be determined from the measurement of sample of known donor to acceptor ratio, most conveniently a donor-acceptor tandem construct, such that $[A^t]/[D^t]=1$.

$$R_{TC} = \frac{\alpha^{(1)} r^{ex,2} - \alpha^{(2)} r^{ex,1}}{\Delta r \delta^{(1)} + \Delta \alpha} = \frac{[D^{ref}]}{[A^{ref}]} \quad 1.28$$

The method outlined above has been denote this method as ‘luxFRET’, as it relies on linear unmixing for the separation of the spectral components used in the determination of apparent FRET efficiency (Wlodarczyk et al. 2008).

1.6.2 Considerations for incomplete labeling

In the equations presented above, we have assumed that all interacting molecules are labeled with intact fluorophores. Returning to the nomenclature presented in figure 1.5, we reiterate that we are measuring the quantities represented by the uppercase concentrations [D], [A], and [DA] in order to investigate those represented the lower case concentrations [d], [a], and [da]. In practice there are many reasons in which these two concentrations are not equivalent: Chemical labeling is often incomplete (Griffin et al. 1998; Zhang et al. 2002; Meyer et al. 2006), fluorescent proteins can be misfolded (Shaner et al. 2005; Su 2005), and all fluorophores eventually bleached (Periasamy et al. 1996). Additionally, investigations involving the expression of fusion proteins are often performed with a background of interacting endogenous proteins. In practice, we are unable to distinguish between the modes of non-functional labeling described above. For simplicity, we consider the general labeling probabilities, p_d and p_a , with which we can write the apparent concentrations as functions of the chemical concentrations.

$$[D] = p_d ([d] + (1 - p_a)[da]) \quad 1.29$$

$$[A] = p_a ([a] + (1 - p_d)[da]) \quad 1.30$$

$$[DA] = p_d p_a [da] \quad 1.31$$

$$[D^t] = p_d [d^t] \quad 1.32$$

$$[A^t] = p_a [a^t] \quad 1.33$$

We can use these equations to solve for the apparent fractional occupancies included within equations 1.24 and 1.25.

$$f_D = [DA]/([D]+[DA]) = p_a [da]/[d^t] = p_a f_d \quad 1.34$$

$$f_A = [DA]/([A]+[DA]) = p_d [da]/[a^t] = p_d f_d \quad 1.35$$

In any case that the tandem construct is used to correct Ef_A or R^t , any estimate of p_d will be dependent on the labeling probabilities of the donor and acceptor in the tandem construct. In these cases p_d' will be used to express this dependency.

$$p_d' = \frac{P_d P_{a,tc}}{P_{d,tc}} \quad 1.36$$

1.6.3 Application to microscopy - alternative analysis modes

Taking the above into consideration, we can modify the equations derived for our apparent FRET efficiencies (1.24 and 1.25). In the case that a tandem construct is measured, it can be assumed that $[a^t] = [d^t]$ and both f_d and f_a are equal to 1. This allows us to define a quantity equal to the FRET efficiency, E , multiplied by the donor or acceptor labeling probability.

$$Ep_d' = R_{TC} \frac{\Delta\alpha}{\alpha^{(1)} r^{ex,2} - \alpha^{(2)} r^{ex,1}} \quad 1.37$$

$$Ep_a = \frac{\Delta\alpha}{\Delta r \delta^1 + \Delta\alpha} \quad 1.38$$

With the reasonable assumption that the total acceptor to total donor ratio is uniform throughout the sample, the latter equation simplifies to

$$Ep_a = \frac{\alpha^{(i)} / \delta^{(1)} - R^t}{\alpha^{(i)} / \delta^{(1)} + r^{ex,i}} \quad 1.39$$

Eq. 1.37 can be simplified, since $r^{ex,2}$ is usually very small, such that the first term in the denominator can be neglected. We then obtain

$$Ep_d' = \frac{R_{TC}}{r^{ex,1}} \left(\frac{\alpha^{(1)}}{\alpha^{(2)}} - 1 \right). \quad 1.40$$

Eqs. 1.37 and 1.40 do not contain apparent donor concentrations but only those of acceptors, measured at 2 excitation wavelengths. The additional parameters are calibration constants. It is possible to determine the product Ep_d' or else $Ef_a p_d'$ from a single emission window in the range of acceptor fluorescence, using alternating dual excitation. If such alternating excitation is available, the measurements can be very conveniently performed with a standard camera or photometric device, since they require neither switching of emission filters.

Eq. 1.39 requires the measurement of a fluorescence ratio (either $\alpha^{(1)}/\delta^{(1)}$ or else $\alpha^{(2)}/\delta^{(1)}$) and the quantity R^t , which is proportional to the ratio of total acceptor over total donor concentrations. This ratio can be calculated for a tandem construct from $\delta^{(1)}$, $\alpha^{(1)}$ and $\alpha^{(2)}$, using equation Eq.1.28. For a tandem construct this ratio is constant except for differential bleaching. For dynamic FRET-measurements it is possible to determine it once before a measurement series and once afterwards (to check for constancy or else to reveal differential bleaching effects). Dynamic measurements can be performed by determining either $\alpha^{(1)}/\delta^{(1)}$ ($i = 1$ in Eq. 1.39) or else $\alpha^{(2)}/\delta^{(1)}$ ($i = 2$ in Eq. 1.39). The first version needs only one short wavelength excitation measurement. It basically determines the ratio of sensitized emission relative to the emission of partially quenched donor and represents the standard ratio method. It can be performed with a beam splitter and a split screen camera (Boehning et al. 2003). Both the second version of this mode and the mode proposed by Eq. 1.41 need dual excitation and spectrally resolved emission.

1.6.4 Noise propagation

It should be noted that Eq. 1.39, for both $i = 1$ and $i = 2$, and Eq. 1.40 represent three different ways to evaluate the FRET-efficiency, each based on a single ratio of apparent fluorophore concentrations. These equations suggest that once the calibration constants and the quantity R^t have been determined, any ratio of the three apparent concentrations can be used to evaluate either Ep_d' or Ep_a for a tandem construct. It is reasonable to assume that the apparent concentrations are not equally resolved and that these equations each propagate error differently. This considered it

becomes of interest to explore which of the analysis modes will result in the best signal to noise ratio. The apparent concentrations are closely related to the leakage and bleed-through corrected fluorescence readings obtained in standard 3-cube measurements. Therefore, the considerations made here should also be relevant for the majority of spectral FRET studies.

Considering that the relative noise of a ratio is the rms-sum of the relative noises of the numerator and denominator, the first strategy for noise optimization should be to achieve high and about equal signal resolution for those two apparent fluorophore concentrations, which are selected for the analysis. Likewise, in the standard ratiometric method (Miyawaki et al. 1999) the two signals $F^{(1,1)}$ and $F^{(1,2)}$ should be optimized. On laser scanning microscopes which will be utilized in the measurements presented below, the noise is dominated by photon shot noise. Since the variance of such noise is proportional to the number of photons collected, the rule stated above suggests that one should obtain an equal and as large as possible number of photons in the two relevant spectral components. This calls for as high as possible signal intensity, which of course is limited by photobleaching.

This fairly intuitive approach should be considered a ‘rule of thumb’ only, since it does not account for the reduced information content of photons due to the overlap of spectral components (Neher and Neher 2004) and for noise propagation, when converting apparent concentrations into E-values, according to Eq. 1.39 - 1.40, or when converting $F^{(1,2)}/F^{(1,1)}$ or E values into an ligand concentrations (Grynkiewicz et al. 1985).

Under the conditions of the measurements presented below, the noise of fluorescence signals is dominated by shot noise, which for Poisson statistics leads to the following expression for the variance of the fluorescence reading in wavelength channel i:

$$\text{Var}(F(\lambda_k)) = s' F(\lambda_k) + \sigma_{o,k}^2 \tag{1.41}$$

Here s' is the apparent peak amplitude of the single photon signal and $\sigma_{o,i}^2$ is the background noise of channel i . For simplicity, we assume s' to be wavelength-independent, which is sufficient for most experiments, although photophysics would predict this to be inversely proportional to wavelength (Neher and Neher 2004). For later use we state that for a photomultiplier-based measurement s' is given by:

$$s' = \frac{s(1 + CV^2)}{2} \quad 1.42$$

where s is the amplitude of the single photon signal, CV^2 represents the dispersion of its amplitude distribution, and the factor $1/2$ is the shape-factor of the single photon signal, assuming a single exponential decay from a peak value of s . In practice the variance is also influenced by the filtering of the signal. The dispersion of the peak amplitude of the photon signal, as well as the effect of filtering, is not readily measured on a given microscope. The apparent single photon signal, s' , however, can be determined as the slope of the mean-variance relationship and, if used consistently, should still allow us to compare our theory with our measurements.

The variance of the fitting coefficients $\delta^{(1*)}$ and $\alpha^{(i*)}$ can be obtained from the diagonal elements h_{kk}^* of the covariance matrix H

$$H = (C^T C)^{-1} \quad 1.43$$

C is the matrix with elements

$$c_{kj} = a_{kj} / \sqrt{\text{Var}(F(\lambda_j))} \quad 1.44$$

where a_{kj} represents reference spectra ($k = 1$ for donor, $k = 2$ for acceptor).

Finally, the variance of the apparent concentrations, which are scaled versions of $\delta^{(1*)}$ and $\alpha^{(i*)}$, are obtained as

$$\begin{pmatrix} \text{Var}(\alpha) \\ \text{Var}(\delta) \end{pmatrix} = h_{kk}^* \begin{pmatrix} I^{(i)} \\ I^{(i,ref)} \end{pmatrix} \quad 1.45$$

Here $I^{(i)}$ and $I^{(i,ref)}$ are excitation intensities during the test- and reference-measurements, respectively.

For the analysis of the expected noise of Ep_a and Ep'_d , as defined by eqs. 1-3, and 6 we consider calibration constants and the quantity R^t to be constant and we use Gaussian error propagation (see Appendix 2 for the complete derivations). We provide the equations for the square of the coefficient of variation ($CV^2 = \text{Var}/\text{Mean}^2$), which yield simple expressions and in the results sections we mostly use the square of the signal to noise ratio (SNR^2), which is the inverse of CV^2 :

For Ep'_d (Eq. 1.37):

$$CV_{Ep'_d}^2 = \frac{(\alpha^{(1)})^2 (\alpha^{(2)})^2 (\Delta r)^2}{(\alpha^{(1)} r^{ex,(2)} - \alpha^{(2)} r^{ex,(1)})^2 (\alpha^{(2)} - \alpha^{(1)})^2} \cdot (CV_{\alpha^{(1)}}^2 + CV_{\alpha^{(2)}}^2) \quad 1.46$$

For Ep_a (Eq. 1.38):

$$CV_{Ep_a}^2 = \frac{(\Delta r)^2 (\delta^{(1)})^2}{(\Delta \alpha)^2 (\Delta r \delta^{(1)} + \Delta \alpha)^2} (\text{var}(\alpha^{(1)}) + \text{var}(\alpha^{(2)}) + (\Delta \alpha)^2 CV_{\delta^{(1)}}^2) \quad 1.47$$

For Ep_a (Eq. 1.39):

$$CV_{Ep_a}^2 = \frac{(\alpha^{(i)})^2 (\delta^{(1)})^2 (r^{ex,(i)} + R^t)^2}{(\alpha^{(i)} + \delta^{(1)} r^{ex,i})^2 (\alpha^{(i)} - \delta^{(1)} R^t)^2} (CV_{\alpha^{(i)}}^2 + CV_{\delta^{(1)}}^2) \quad 1.48$$

For Ep'_d (Eq. 1.40):

$$CV_{Ep'_d}^2 = \frac{(\alpha^{(1)})^2}{(\alpha^{(1)} - \alpha^{(2)})^2} (CV_{\alpha^{(1)}}^2 + CV_{\alpha^{(2)}}^2) \quad 1.49$$

For the measurements of the emission ratio, the CV^2 is simply the sum of the CV^2 values of the numerator ($F^{1,2}$) and the denominator ($F^{1,1}$). Ligand concentration can be estimated from the emission ratio measurements (Grynkiewicz et al. 1985) well as from FRET measurements. The estimated variance of ligand concentration computed from FRET efficiency is

$$CV_{[X]}^2 = \left(\frac{E}{(E - E_o)} \cdot \frac{(E_{\max} - E_o)}{(E_{\max} - E)} \right)^2 CV_E^2$$

1.50

and from emission ratio measurements the

$$CV_{[X]}^2 = \left(\frac{R}{(R - R_o)} \cdot \frac{(R_{\max} - R_o)}{(R_{\max} - R)} \right)^2 (CV_{F_1}^2 + CV_{F_2}^2).$$

1.51

2 Materials and Methods

2.1 Cell culture and transient transfection

N1E-115, HEK-293, or tsA-201 cells from the American Type Culture collection (ATCC) were grown in Dulbecco's modified Eagle's medium (DMEM) containing 10% fetal calf serum (FCS) and 1% penicillin/streptomycin at 37 °C under 5% CO². For transient transfection, cells were seeded at low-density in 60-mm dishes (1×10⁶), 35-mm dishes (2.5×10⁵) or on 10-mm cover-slips (5×10⁴) and transfected with appropriate vectors using Lipofectamine2000 Reagent (Invitrogen) according to the manufacturer's instruction. Four hours after transfection, the transfection medium was exchanged and the cells were serum starved over night before analysis. The Cerulean-Epac-Citrine FRET construct was a kind gift from Dr. Marcus Niebert from the Department of Neuro and Sensory Physiology, University of Göttingen, and was based on the CFP-Epac-YFP construct presented in Ponsioen et al. 2004.

2.2 Fluorescence spectroscopy

Mouse N1E-115 neuroblastoma cells were co-transfected with the appropriate plasmid DNAs. 24-48 hours after transfection, cells were resuspended in Dulbecco's phosphate buffered solution (DPBS). All measurements were performed in 10 mm pathway quartz cuvettes using a spectrofluorometer (Fluorolog, Horiba Jobin Yvon, Unterhaching, Germany) equipped with a 450 W xenon lamp and the photomultiplier working at 950 V. The cell suspension was continuously perturbed with a magnetic stirrer while the temperature was maintained at 37 °C during the experiment. For calibration measurements, cells were transfected with plasmids encoding a single fluorophore. Excitation was performed at 458 nm and 488 nm with 5 nm spectral width and emission was collected from 468 to 620 nm in 1nm increments with a 0.5 s integration time. The spectral contributions due to light scattering and non-specific fluorescence of the cells were taken into account by unmixing the emission spectra of non-transfected cells (background) from each measured spectra. Before each

measurement, the spectrofluorometer was calibrated for the xenon-lamp spectrum and Raman scattering peak position.

2.3 Cell lysate preparation and pH titration

N1E-115 mouse neuroblastoma cells were plated in 35 mm dishes and transfected with the CFP-YFP tandem construct as described above. 24 -48 hours after transfection, cells were washed 3 times and suspended in intercellular solution. The cells were then lysed using a motorized tissue homogenizer (15x at 2,500rpm). The cell lysate was then centrifuged at 14,000 rpm for 1 min. The supernatant was removed and used for the fluorescence measurements. HCL and NaOH were used for titration to the desired pH. Two-excitation luxFRET measurement performed on Fluorolog. Measurements were performed on the same lysate with pH ranging from 5.0 to 9.5. The initial pH measured was 7.4 then the pH was titrated to 7.0, then down to 5.0 in 0.5 steps with 0.1N HCl. The pH was then titrated to 9.5 in 0.5 increments with 0.1N or 1N NaOH and back down to 7.4 with HCl. The luxFRET quantities calculated that were found to be pH dependent were fitted with a modified Hill equation.

$$E_f^D = (E_{f_{D,\max}}^D - E_{f_{D,o}}^D) \frac{[10^{pH}]^n}{[10^{pK_a}]^n + [10^{pH}]^n} + E_{f_{D,o}}^D \quad 2.1$$

2.4 Fluorescence lifetime FRET measurements

Fluorescence lifetime decays were obtained by time-correlated single photon-counting measurements of fluorescence using a Fluorolog-3 spectrofluorometer (Horiba Jobin Yvon, München, Germany). Samples were placed in 10-mm pathway quartz cuvettes (10×10 mm²) and continuously perturbed with a magnetic stirrer. Emission was collected in right angle geometry. Excitation was performed with a 460nm nanoLED (Horiba Jobin Yvon) with a 440/40 nm transmission filter (Semrock, Tubingen, Germany). Fluorescence intensity was measured in the wavelength band

from 468 nm to 482 nm to avoid excitation scattering and acceptor fluorescence. Typical fluorescence decays were fit with the resulting sum of one, two, or three exponentials, iteratively convolved with the instrument response function using the standard Decay Analysis Software 6 (Horiba Jobin Yvon) and CFS_LS software (available from Center for Fluorescence spectroscopy at <http://cfs.umbi.umd.edu/cfs/>). The quality of the fits was evaluated by the structure observed in the plots of residuals and by the reduced chi-square values.

$$F(t) = \sum_i F_{i,o} \cdot e^{-t/\tau}$$

2.2

The mean fluorescence lifetimes were calculated as the amplitude-weighted lifetimes and used in the following equation to estimate the efficiency of energy transfer.

$$E = 1 - \frac{\tau_{DA}}{\tau_D}$$

2.3

2.5 Imaging setup

All images were acquired on a Zeiss LSM 510-Meta confocal microscope (Carl Zeiss, Jena, Germany) with a 40x oil-immersion objective (NA 1.3). For excitation of CFP or cerulean, the 458 nm line of a 40mW Argon laser was used with a 458 nm dichroic mirror. For excitation of YFP or citrine, the 488 nm laser line of the Argon laser was used with a 488 nm dichroic mirror. Fluorescence was generally detected over eight channels over, for the short wavelength excitation from 468 – 636nm, and for the long wavelength excitation 509 – 594nm . All images were digitized/collected with 12 bit resolution.

2.6 Live cell imaging

For imaging of live cells, cover slips were placed in custom made image acquisition chambers with 2 ml of D-PBS. In the measurements on the CFP-YFP tandem construct for establishing a relationship between excitation intensity and variance of the apparent concentrations, the 458 nm line of the

Argon laser was used as the first excitation wavelength, $i = 1$, at 25% power and with transmission varied within the range of 5-20%. For the second excitation wavelength, $i = 2$, the 488 nm laser line was used at 25% power, with transmission ranging from 1 to 6%. Appropriate excitation intensities for donor and acceptor fluorophores were tested on a cell other than the one used for the subsequent measurements. Intensities were adjusted to obtain less than 1% of bleaching per exposure. Using a 172 μm confocal pinhole, fluorescence emission was acquired from individual fluorophore over 8 λ channels, each 21.4 nm in width, covering a spectral band from 464 to 636 nm.

The imaging parameters were set such that SNR of the measurement was maximized within the constraint that bleaching of either fluorophores did not exceed approximately 1% per acquisition. For dynamic measurements of the Epac FRET sensor, image acquisitions with excitation at 488 nm preceded and followed a series of 61 images acquired at 10 second intervals with excitation at 458 nm. After the 21st image acquisition of a given series either forskolin was added to the bath solution to a final concentration of 10 μM or an equal volume of control delivery vehicle was applied. For the dynamic FRET measurements of an Epac based cAMP sensor, the power of the Argon laser was set to 25%. For excitation with the 458 nm laser line, transmission was set to 20% and emission collected through a 74 μm confocal pinhole over 8 channels spanning 464 nm – 636nm. For excitation with the 488 nm laser line, transmission was set to 3.5% while the pinhole was adjusted to 172 μm and the emission window was shifted to 497 nm – 583 nm. The scanning pixel dwell time was set to 12.8 μs .

2.7 lux-FRET image analysis

All analysis discussed in this paper was performed using Matlab 7.2 (The MathWorks, Natick, MA). Prior to 2-excitation luxFRET analysis, images were spatially aligned in order to minimize effects of object movement during acquisition and/or misalignment of dichroic mirrors. Alignment is performed by a custom Matlab script by shifting one image to minimize the summed squared

difference of normalized images from each acquisition and usually requires less than a 2 pixel shift in the x-y plane. The reference fluorescence spectra were obtained from user-selected regions of interest (ROI) of reference images of cells expressing either donor or acceptor alone. The background spectra was similarly measured from the same images and subtracted from the reference spectra. These images were acquired with the same excitation and detection parameters as used for the FRET image acquisition. In each FRET measurement, linear unmixing, with non-negativity constraints, was performed pixel by pixel using background subtracted reference spectra. Background correction of the FRET sample was performed either through the subtraction of unmixing of a background spectra sampled as described for the reference measurements. The apparent concentrations resulting from the linear unmixing were then used according to eqs. 1.37-1.40 to calculate the apparent FRET efficiencies.

2.8 Determination of apparent single photon signal

Multiple images of a fluorescent polymer slide (Chroma Technology, Rockingham, VT, USA) were acquired with the 458nm line of an argon laser with increasing excitation intensity. A dark current recording with the excitation shutter closed was made preceding the measurement series to measure the background noise of the detectors, permitting correction for dark current and stray-light. Emission was collected over the same 8 channels spanning 464 – 636 and at the same detector gain as used in the FRET measurements. The mean and variance of the measured fluorescence from emission channels were calculated. The apparent single photon signal (s') and the background noise of channel (σ_i^2) were then calculated using equation 1.41. The apparent single photon signal was calculated for detector gains ranging from 300 to 700V in 50V increments.

3 Results

3.1 Calibrations for luxFRET measurements

To begin the calibration necessary for luxFRET analysis, we need to measure the complete emission spectra of the donor and acceptor fluorophores. In this case, emission spectra were collected from suspensions of N1E-115 cells expressing exclusively CFP or YFP. Excitation was performed at wavelengths shorter than any emission, 420 and 458nm, respectively. Emission was collected with 1nm resolution from 430 to 620nm for CFP and 468 to 620nm for YFP (see methods and materials). Characterization of emission was performed by normalizing each complete emission spectrum to unit area. This creates probability distributions of emission for CFP and YFP which we designated as $e_D(\lambda)$ and $e_A(\lambda)$, with subscripts D and A referring to donor and acceptor, respectively. These spectra will be denote as ‘characteristic spectra’.

In addition to the characteristic spectra, we measure reference spectra from the donor and acceptor samples at the wavelengths with which the FRET sample will be measured. The short wavelength excitation was performed at 458nm and the long wavelength excitation was performed at 488nm. The excitation wavelengths were chosen to correspond to popular argon laser lines to investigate the feasibility of eventually adapting this method to microscopy. These spectra are not normalized and will hence forth be denoted as ‘reference spectra’ using the following nomenclature, $F_D^{(i),ref}(\lambda)$ and $F_A^{(i),ref}(\lambda)$, for donor (CFP) and acceptor (YFP), respectively, at the i^{th} (1 or 2) excitation wavelength. It should be emphasized that the excitation wavelengths used in the acquisition of the reference spectra and in the measurement of the FRET sample need not be the same as those used in the definition of the characteristic spectra.

Together, the characteristic and reference spectra are used to quantify the excitation ratios, $r^{ex,i}$, defined by eq. 1.27. This quantity is a measure of the ratio of donor and acceptor extinction coefficients, scaled by the reference concentration ratio. By multiplying the probability distribution

of emission of a fluorescent molecule (characteristic spectrum) by its quantum efficiency, we define the probability distribution of emission per excitation event. Dividing the reference spectrum by this distribution (appropriately sampled to match the window over which the reference spectra were measured) we can obtain a quantity which is proportional to the number of excitation events occurring during the fluorescence acquisition. Taking the ratio of these quantities for the donor and acceptor references, we cancel all instrument dependent factors such as excitation intensity, detector efficiency and effect of digitization, leaving us with the ratio of extinction coefficients scaled by the reference concentration ratio. Accurate estimation of this ratio has been a hurdle for many other FRET methods and is often the reason for exhaustive calibration procedures (Hoppe et al. 2002; Thaler et al. 2005).

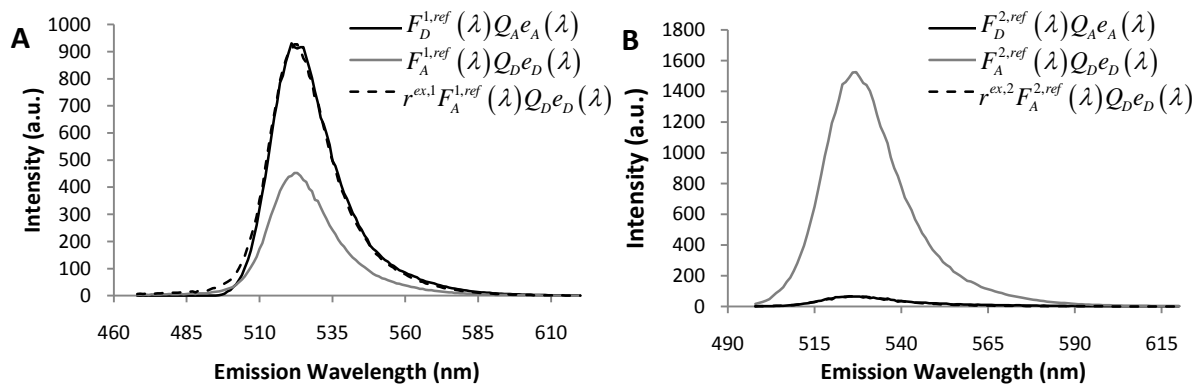


Figure 3.1 | Calculation of excitation ratio, $r^{ex,i}$. Donor fluorescence reference spectra, scaled by the acceptor quantum efficiency and the acceptor characteristic spectra, (numerator of eq. 1.27) are fitted to acceptor fluorescence reference spectra, scaled by the donor quantum efficiency and the donor characteristic spectra (denominator of eq. 1.27). A) For CFP and YFP with excitation at 458 nm a $r^{ex,1}$ of 2.05 results in the best fit. B) For CFP and YFP with excitation at 488nm a $r^{ex,2}$ of 0.04 results in the best fit.

Using the measured characteristic and reference spectra, along with quantum efficiency values from literature, $Q_D = 0.40$ (Patterson et al. 2000) and $Q_A = 0.61$ (Su 2005), the excitation ratios at $\lambda^{(1)} = 458$ nm and $\lambda^{(2)} = 488$ nm were determined, as $r^{ex,1} = 2.05$ and $r^{ex,2} = 0.04$, respectively. By

directly solving eq. 1.27, $r^{ex,i}$ can be determined as a function of emission wavelength. It should, however, be constant with respect to wavelength and equal to the scaling factor resulting from the fitting of the denominator with the numerator of Eq. 1.27, as illustrated by figure 3.1.

3.2 Determination of FRET efficiency

In order to estimate the FRET efficiency of a CFP-YFP tandem construct, fluorescence emission spectra were measured at the same intensity and wavelength as the reference measurements used to determine $r^{ex,i}$. Least square fitting of the reference spectra to the spectra measured from the FRET sample was performed. The donor and acceptor apparent concentrations were determined from the weights of the donor and acceptor reference spectra at which the best fit occurs. A third apparent concentration is also 'unmixed' from the FRET sample spectra to account for any background, scattering (Raman and excitation), or auto-fluorescence. In the example of the fitting of reference spectra to the tandem construct FRET sample, shown in figure 3.2, the unmixed apparent concentrations, or weights resulting in the best fit, were $\alpha^{(1)}=4.48$, $\delta^{(1)}=1.72$, and $\alpha^{(2)}=2.05$. $\delta^{(2)}$ is not determined as donor emission from the long wavelength excitation and is often negligible. Conveniently this term is not required for the analysis. Using the apparent concentrations, as well as the calibration terms ($r^{ex,i}$), we can determine the apparent FRET efficiency, Ef_D , from eq. 1.24, as 0.41. A closer look at Eq. 1.25 shows that this estimate for apparent FRET efficiency, Ef_A , is scaled by the reference concentration ratio. Correct determination of Ef_A requires an additional calibration. Using Eq. 1.26 we can calculate the FRET corrected total acceptor donor ratio. In this case $R^t=0.68$. This quantity is also scaled by the reference concentration ratio. With the acceptor to donor ratio of a tandem construct, safely assumed to be 1, we can there determine the reference concentration ratio and correct the acceptor apparent FRET efficiency. By necessity of definitions, if $[A^t]/[D^t]=1$, Ef_A equals Ef_D .

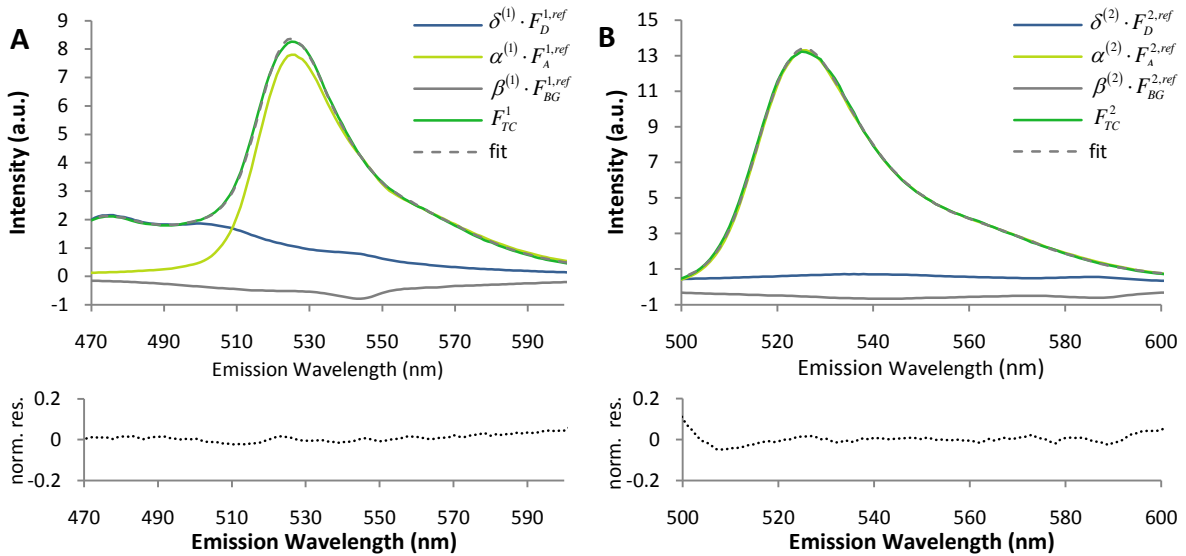


Figure 3.2 | Spectral analysis of fluorescence from a cytosolic CFP-YFP tandem construct. A) Fluorescence collected from the CFP-YFP tandem construct with excitation at 458nm is unmixed into the weighted components from CFP, YFP and background reference spectra. The grey dashed line represents the sum of the scaled reference spectra. B) Spectral decomposition is performed for the spectra collected from the FRET sample with excitation at 488nm. The lowermost traces of each subfigure represent the normalized residuals of the FRET spectra and their respective fits.

This cytosolic construct provides a FRET standard that can be used across several platforms to evaluate the accuracy of the FRET efficiency estimate shown above. To verify that our method accurately measures apparent FRET efficiency, we performed measurements utilizing two established, yet less flexible, methods. First, acceptor photobleaching was performed on fixed and live N1E-115 cells expressing the CFP-YFP tandem construct with a confocal laser scanning microscope. Figure 3.3 shows an example of the photobleaching experiments performed. The intensity of the partially quenched CFP emission is measured using 458nm excitation. Using high intensity 514nm excitation YFP is selectively and completely bleached. Following the YFP bleaching, the fluorescence intensity of the now de-quenched CFP is measured. The apparent FRET efficiency, E_{fD} , can be determined from the pre and post bleach CFP intensities according to $E = 1 - F_{DA}/F_D$ and was determined to be 0.37. During these experiments it was observed that the apparent FRET measured in the fixed cells was significantly less than in live cells. Live cell acceptor photobleaching is

often not performed due to the requirement of whole cell bleaching to prevent artifacts resulting from diffusion between bleached and unbleached regions.

An additional verification of the FRET efficiency of the CFP-YFP tandem construct determined from the proposed method was performed through the analysis of donor fluorescence lifetime decays. In the presence of a FRET acceptor an additional de-excitation pathway is created. This shortens the excited state lifetime of the donor. This can be directly measured and the efficiency of energy transfer can be calculated through the determination of the fluorescence lifetime of the donor in presence and absence of acceptor. Because the fluorescence lifetime is concentration independent, the measurements can be performed on separate samples, unlike in the case of acceptor photobleaching.

Fluorescence lifetimes of free CFP and CFP in the CFP-YFP tandem construct were measured by time correlated single photon counting (TCSPC) as described in Methods. The fluorescence decay histograms were fit through the iterative convolution of a biexponential decay function with the instrument response function. A mean lifetime was calculated as a contribution-weighted average of the two individual decay time constants. The average fluorescence lifetime of CFP in the absence of YFP was found to be 2.44 ns ($\chi^2 = 1.24$). The average fluorescence lifetime of CFP in the tandem Construct was found to be 1.46 ns ($\chi^2 = 1.31$). Using Eq. 2.3 we can calculate a FRET efficiency of 0.40. As this was calculated from average fluorescence lifetimes of the FRET sample which can include 'free' CFP, resulting from incomplete labeling, misfolding, partial bleaching, we cannot state that this estimate is the characteristic efficiency of energy transfer. CFP has a bi-exponential decay and it can be assumed that in a partially quenched sample there are as many as four exponential components which are usually not resolved (Millington et al. 2007). Therefore, estimates which use average decay lifetimes can be considered as apparent FRET efficiencies and are comparable to the other efficiencies measured by acceptor photobleaching and luxFRET.

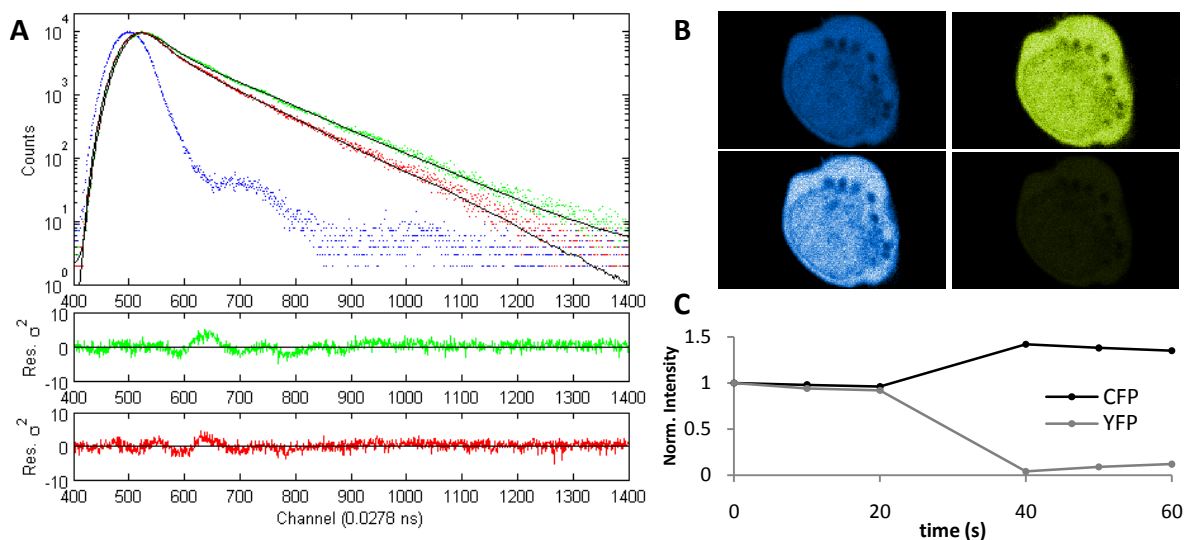


Figure 3.3 | Verification of computed apparent FRET efficiency with established methods. A) Time correlated single photon counting (TCSPC) was used to measure the lifetime of the free donor, green histogram, and the donor in the CFP-YFP tandem construct configuration, red histogram. The decay histograms were fit through iterative convolution of exponential functions with the instrument response function (blue histogram). The average fluorescence lifetimes of free and acceptor labeled donor were found to be 2.44 ns ($\chi^2=1.24$) and 1.46 ns ($\chi^2=1.31$) respectively, implying a FRET efficiency of 0.40. B) Acceptor photobleaching was used as an additional method to verify the FRET efficiency of the tandem construct. The pre and post bleach images of the unmixed acceptor and donor show the coordinated de-quenching of CFP with the bleaching of YFP. C) The fluorescence intensities sampled from the bleached region of interest is quantified and used to calculate a FRET efficiency of 0.37.

3.3 Influence of fractional occupancy and partial acceptor photobleaching

The apparent FRET efficiencies that we measure, E_{fD} and E_{fA} , are the products of the characteristic efficiency of energy transfer, E , and the apparent fractional occupancy of the donor or acceptor. We consider the apparent fractional occupancy as the product of the chemical fractional occupancy and the probability of correct labeling (discussed previously). To evaluate the effect of a change in the apparent fractional occupancy, or more appropriately the probability of correct labeling, on the quantities measured by luxFRET several acquisition were performed as described above. These measurements were performed with intermittent bleaching cycles. The bleaching cycles should effectively decrease the donor quenching estimated apparent FRET efficiency, E_{fD} , by decreasing p_a

included in the apparent fractional occupancy (Eq. 1.34). No effect should be observed in the acceptor sensitization-estimated apparent FRET efficiency nor the apparent acceptor fractional occupancy.

After acquisition of the two emission spectra required for luxFRET analysis, N1E-115 cells expressing the CFP-YFP tandem construct were exposed to high intensity excitation at 514nm (peak absorption of YFP) for 2 hours. This cycle was repeated five times until approximately half of the acceptor had been bleached.

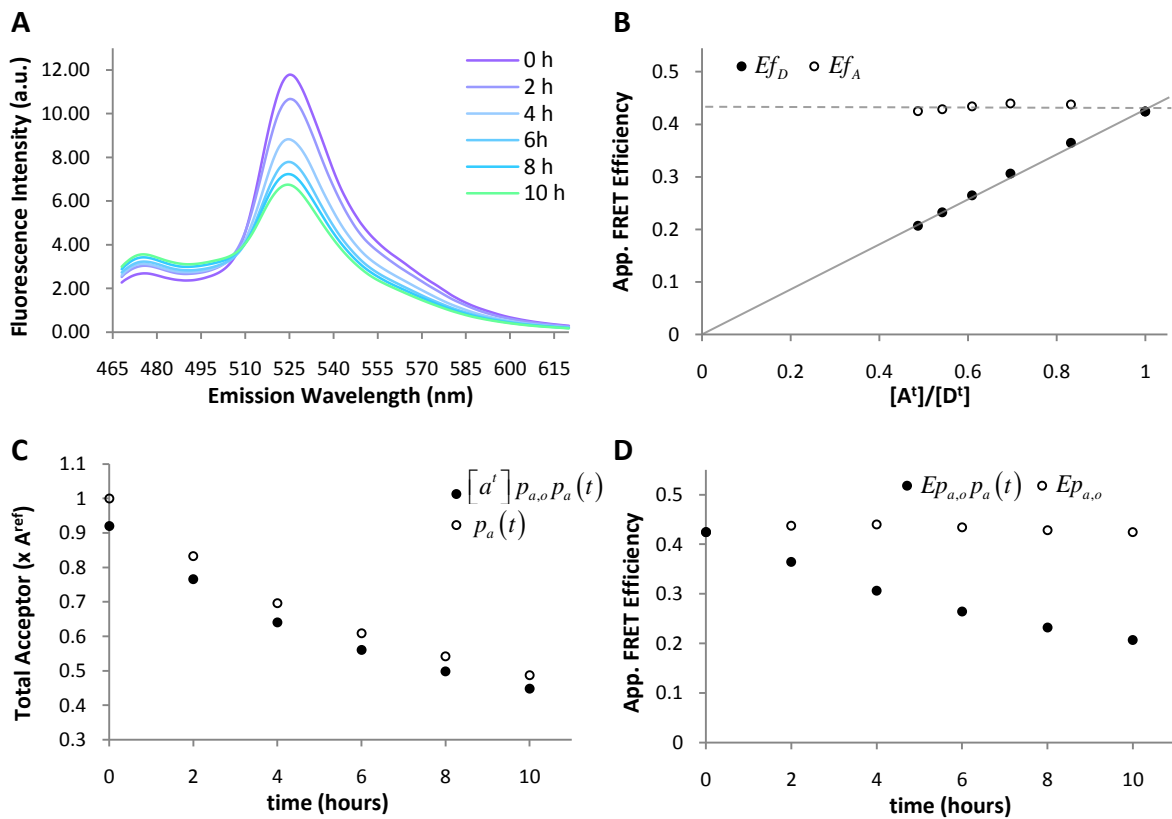


Figure 3.4 | Partial acceptor photobleaching of the cytosolic CFP-YFP tandem construct. A) Emission spectra from the CFP-YFP construct measured during the 458nm excitation. Corresponding to the decrease in the peak at 525nm resulting from the YFP bleaching, a increase in the peak at 475nm is observed due to the de-quenching of CFP. B) Ef_D and Ef_A were measured in between each 2 hour bleaching interval. By definition of the quantities for a tandem construct, the initial values for Ef_D and Ef_A are equal and $R^{\dagger} = 1$. Over the course of the bleaching a decrease in Ef_D is observed while Ef_A remains unaffected by the bleaching. C) The time course of the total acceptor is normalized to determine the time dependent component of acceptor labeling probability. D) By dividing $Ef_D p_a$ by $p_a(t)$ we can define $Ef_D p_{a,o}$ and correct for bleaching.

Taking into consideration the definitions of the apparent fractional occupancy, and assuming that the initial chemical fractional labeling of the tandem construct is 1, we can conclude that the quantities measured are the characteristic efficiency of energy transfer scaled by the functional probability (properly folded, unbleached...). By assuming that $[A^t]/[D^t] = 1$ for the first measurement we see that the donor and acceptor apparent FRET efficiencies are equal. Over the course of the experiment these two measurements diverge, with the apparent FRET efficiency containing the acceptor functional probability ($Ef_d p_a$) decreasing with continued acceptor bleaching. Figure 3.4 shows a decrease, not only in this apparent FRET efficiency, but also in the acceptor to donor ratio. Ef_A remains unaffected by bleaching over time.

In addition to the apparent FRET efficiencies, luxFRET provides the ability to measure the FRET corrected total acceptor and donor concentrations. Figure 3.4 panel C shows the time-course of $[A^t]$ throughout the bleaching measurements. By assuming that the total chemical concentration of acceptor, $[a^t]$, is not changing, we can attribute any change in the apparent total concentration, $[A^t]$, to a time dependant functional probability term such that $[A^t] = [a^t] p_{a,o} p_a(t)$. By normalizing $[a^t] p_{a,o} p_a(t)$ to its initial value, $[a^t] p_{a,o}$, the time dependent component can be characterized. This functional probability is same as that included in Ef_D and thus by dividing the apparent FRET efficiency by this term we can correct for acceptor photobleaching as indicated by figure 3.4 panel D.

3.4 pH sensitivity of YFP and its influence on FRET analysis

Ambient factors such as pH have been shown to influence the fluorescent properties of many fluorophores (Griesbeck et al. 2001) and to have effects on FRET efficiency measurements (Salonikidis et al. 2008). To evaluate the effect of pH on the luxFRET quantities, measurements at varied pH values were performed. In order to directly modulate the ambient pH and prevent cellular buffering processes, cells expressing the cytosolic tandem construct were lysed. The lysate was then spun down and the supernatant used for the measurements. The FRET measurements were performed as previously described. The initial measurement was performed at pH 7.4, then in 0.5 pH

point increments while adjusting pH with HCl or NaOH. pH was increased to 9.5, then reduced to 5.0, and returned to 7.4, to test for the reversibility of any effects.

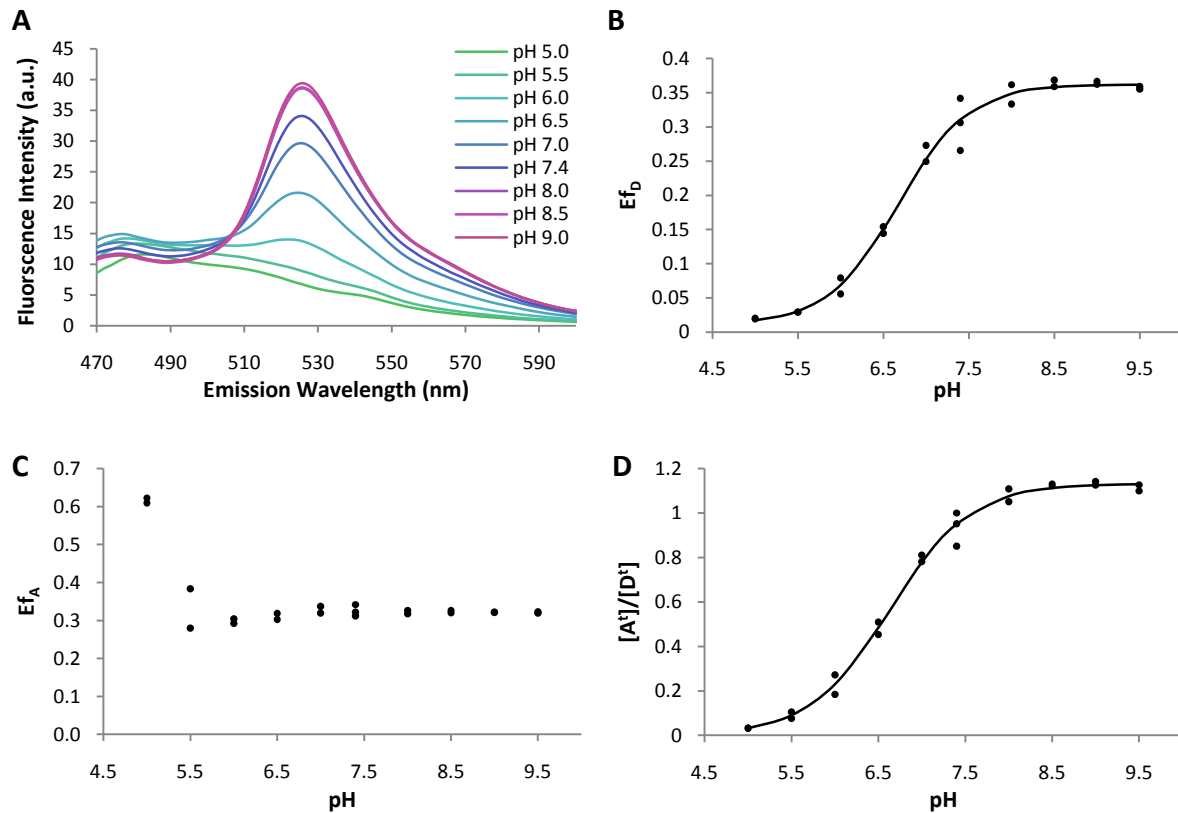


Figure 3.5 | pH dependence of lux-FRET quantities. A) Emission spectra of the CFP-YFP for the range of pH. With a decrease in pH, the contribution to emission of YFP is greatly decreased. There also seems to be a de-quenching of CFP. At the lowest pH value the contribution of YFP seems negligible and there also seems to be a decrease in the fluorescence of CFP. B) There is a clear relationship between the measured Ef_D and pH. Fitting of the data with the Hill equation, Eq. 2.1, to the Ef_D vs. pH data resulted in a $pK_a = 6.7$ and a Hill coefficient $n = 1.1$, with an $R^2 = 0.99$. C) No pH dependency on Ef_A is indicated. D) The FRET corrected ratio, R^t , shows the same dependence as Ef_D , $pK_a = 6.6$ and $n = 0.9$ when fit with the same model. At the low pH extreme the ratio approaches 0, indicating that nearly no emission from YFP occurs.

A strong dependence of YFP emission on pH was observed. Figure 3.5 indicates a decrease in YFP emission as well as a de-quenching of CFP as pH was decreased from 9.0 to 5.0. This dependency is reflected in the Ef_D value shown in panel B. Fitting the Ef_D data to the Hill equation presented as eq. 2.1 indicates a pK_a of 6.7 and a Hill coefficient 1.1 (suggesting no cooperativity). The Ef_A quantity,

which we have shown not to be affected by YFP bleaching, is not affected by changes in pH as well. Panel C of figure 3.5 shows that at the low pH extreme the measured E_{f_A} becomes unstable, indicated by inconsistent values at pH 5.5 and unreasonable values at pH 5.0. The total acceptor to total donor ratio shows a dependency similar to that of E_{f_D} . The fitted parameters of the Hill equation are similar, with $pK_a = 6.6$, $n=0.9$. Also apparent in this figure, the emission of YFP is almost completely abolished, as the ratio approaches 0 at pH 4.5.

3.5 Identification of intermolecular interaction

In the case of homo-oligomeric interaction, the apparent fractional occupancies, f_D and f_A are dependent on expression ratio of the donor and acceptor. As the donor fraction of a sample is decreased, the probability of donor-donor complex formation also decreases. In the case of high affinity interactions (K_d much less than total concentration) it would be expected that all donor molecules are occupied with acceptors at the lower limit of donor fraction values. In this case it can be assumed that $f_d=1$ and the apparent FRET efficiency measured estimates E_{p_a} . In the case of lower affinity interaction (i.e. K_d near the total concentration) we would expect a combination of donor molecules occupied with acceptors as well as free donors but no donor-donor interaction. For this reason, it is important to measure and take into consideration the relative abundances of donor and acceptor molecules when comparing apparent FRET efficiencies between samples.

The apparent FRET efficiencies, E_{f_D} and E_{f_A} , were measured from N1E-115 cells co-expressing 5HT_{1A}-CFP and 5HT_{1A}-YFP. Similar measurements of CD28 and CD86 were used as controls for discrimination between specific and non-specific interaction. CD28 is an immune-receptor that has been shown to form covalent dimers in the plasma membrane (Greene et al. 1996; Lazar-Molnar et al. 2006). CD86, a receptor also found at the immunological synapse, is a monomeric ligand of the CD28 complex (Sansom et al. 2003; James et al. 2006). Both of these proteins have been used as positive and negative controls in methods which study protein-protein interaction with fluorescence and bioluminescence techniques (James et al. 2006; Bouvier et al. 2007; Dorsch et al. 2009).

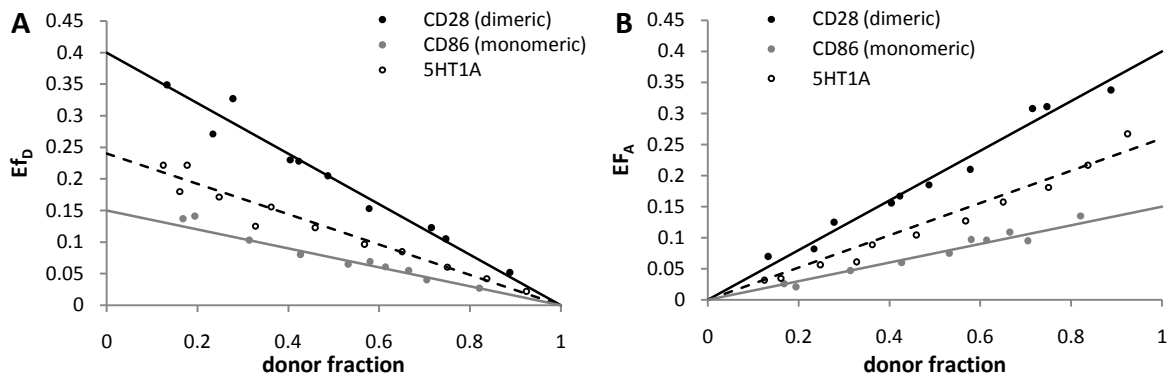


Figure 3.6 | Identification of intermolecular interaction. The donor quenching related and sensitized emission related apparent FRET efficiencies, Ef_D and Ef_A , were measured from expression of CFP and YFP labeled samples. The first sample, CD28, is a covalently linked homodimer that is localized in the plasma membrane and serves as a positive control for complete dimerization of surface receptors. The second sample, CD86, is a monomeric transmembrane receptor that serves as a control for stochastic interaction of plasma membrane localized receptors. The third sample is the 5HT_{1A} receptor. A) The donor quenching related apparent FRET efficiency, Ef_D , is plotted against donor fraction. For the entire range of donor fractions, the Ef_D measured from the coexpression of 5HT_{1A}-CFP and 5HT_{1A}-YFP is between that measured for the two controls. B) Similarly to the measurements of Ef_D , Ef_A values measured from the 5HT_{1A}-CFP/5HT_{1A}-YFP co-expression are between the two controls.

To compare measurements between these samples, the apparent FRET efficiencies were plotted as functions of the corresponding donor fraction measured in each sample in figure 3.6. Because the apparent FRET efficiencies are also dependent on the expression ratio, comparison of efficiencies without quantification of the expression ratio (or fraction) would not yield any information regarding the relative degree of self association between two samples. The apparent FRET efficiency measured from the samples expressing the monomeric control, CD86, suggest a significant amount of stochastic interaction. Assuming that the total concentration of CFP and YFP tagged receptors is equivalent in all samples, the apparent FRET efficiencies measured from 5HT_{1A}-CFP and 5HT_{1A}-YFP suggest that the degree of interaction surpasses that of stochastic interaction. However, figure 3.6 also shows that high affinity constitutive dimerization of 5HT_{1A} is unlikely. The increase in apparent FRET efficiency above the level measured for stochastic interaction for the

covalently dimerized CD28 is more than double that of the 5HT_{1A} receptor. This could be due to the adoption of a conformation more favorable to FRET in the case of the CD28 tagged constructs. This conformation could result in a closer interaction or a more favorable orientation of the fluorescent proteins. However, assuming that these factors are equal between the CD28 and 5HT_{1A} constructs, it can be concluded there is some self association between 5HT_{1A} receptors with a substantial portion, >50%, existing in a monomeric configuration.

3.6 Spectral imaging and implementation of luxFRET to microscopy

The method presented above is one of many methods categorized as spectral FRET methods due to the requirement of at least two distinct spectral channels from which donor and acceptor emission is collected. Although two channels are sufficient for the separation of two fluorescent contributions, when implementing this method to microscopy, the Zeiss LSM510 Meta system was used to measure fluorescence at a spectral resolution of up to 10.7nm over eight channels simultaneously. Implementation of luxFRET to spectral microscopy can be performed analogously to its implementation to spectroscopy, shown above, although at a lower spectral resolution.

To perform the excitation ratio calibration, two reference samples are measured with the same excitation and emission parameters as the FRET sample. These reference samples express CFP or YFP exclusively. Reference emission spectra are measured as the mean intensity from the same region of interest sampled across the entire spectral stack, as illustrated in figure 3.7. The characteristic (unit area normalized) emission spectra is sampled according to the spectral channels with which the measurements are performed. Analogously to the application to spectroscopy shown in figure 3.1, figure 3.7 illustrates how this sampled characteristic emission spectra is then used with the measured reference spectra and the donor and acceptor quantum efficiencies to determine the excitation ratios, $r^{ex,i}$.

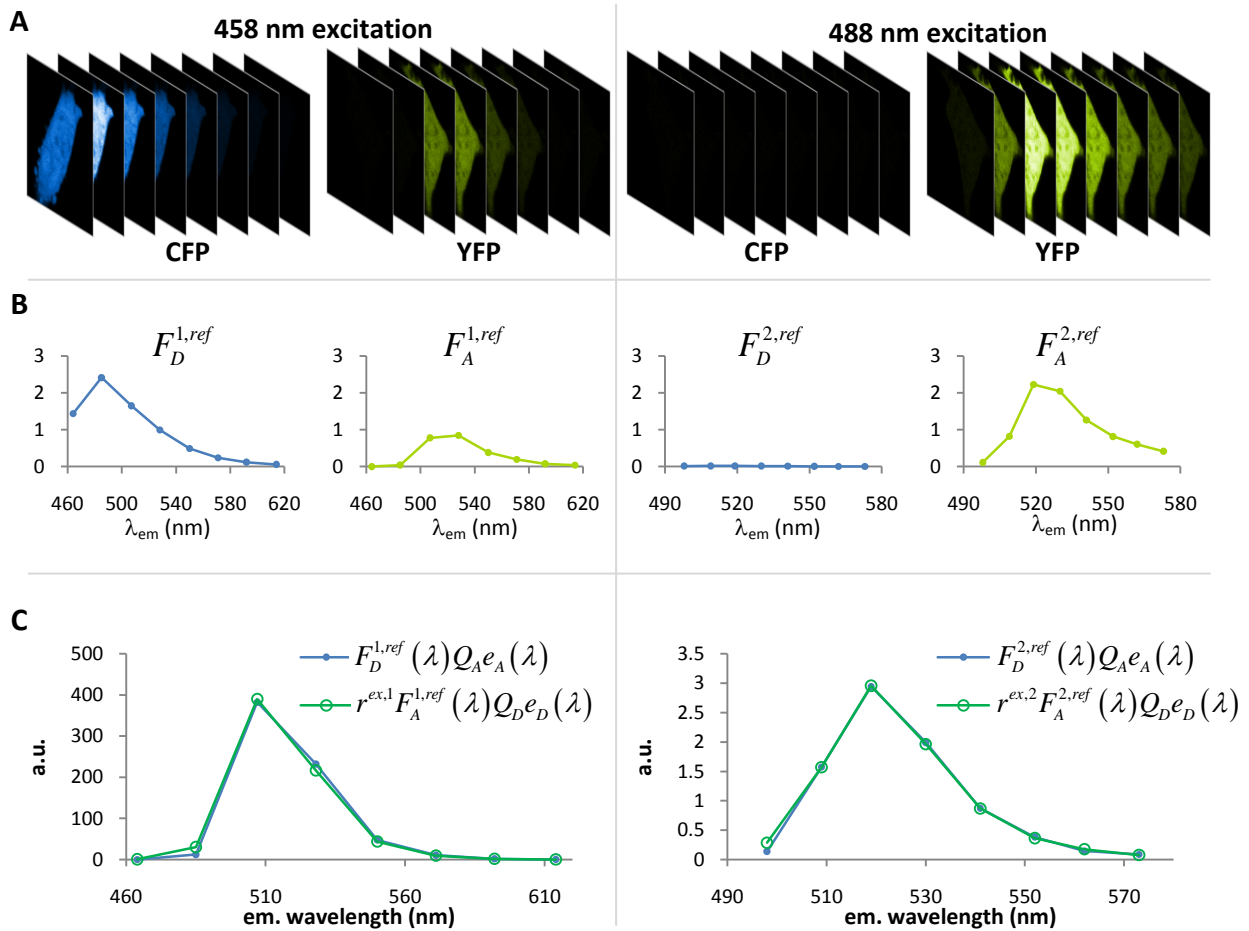


Figure 3.7 | Excitation ratio calibration from spectral images. A) Spectral image of reference samples expressing exclusively CFP or YFP are acquired with excitation at 458nm and at 488nm. B) The mean intensities measured from the same region of interest across the spectral stack are used to construct reference spectra. C) Using the measured reference spectra, appropriately sampled characteristic spectra and the donor and acceptor quantum efficiencies, the excitation ratios, $r^{ex,1}$ can be determined.

In the case of spectral imaging of a FRET sample, each pixel corresponds to an emission spectra from which donor and acceptor contributions can be separated. Using the donor and acceptor reference emission spectra defined within figure 3.8, linear unmixing of the FRET sample spectral image is performed on a per pixel basis. Figure 3.8 part A illustrates two spectral images of the CFP-YFP tandem construct FRET reference. The first spectral stack corresponds to the emission collected over 464 – 635nm at 21.4nm resolution using 458nm excitation wavelength. The second stack corresponds to the emission collected over 498 – 584nm at 10.7nm resolution using 488nm excitation wavelength. Part B provides an example of the linear unmixing of the FRET sample spectra

performed at lower spectral resolution. Linear unmixing is performed on a per pixel basis resulting in spatial maps of apparent concentrations shown in figure 3.8 part C.

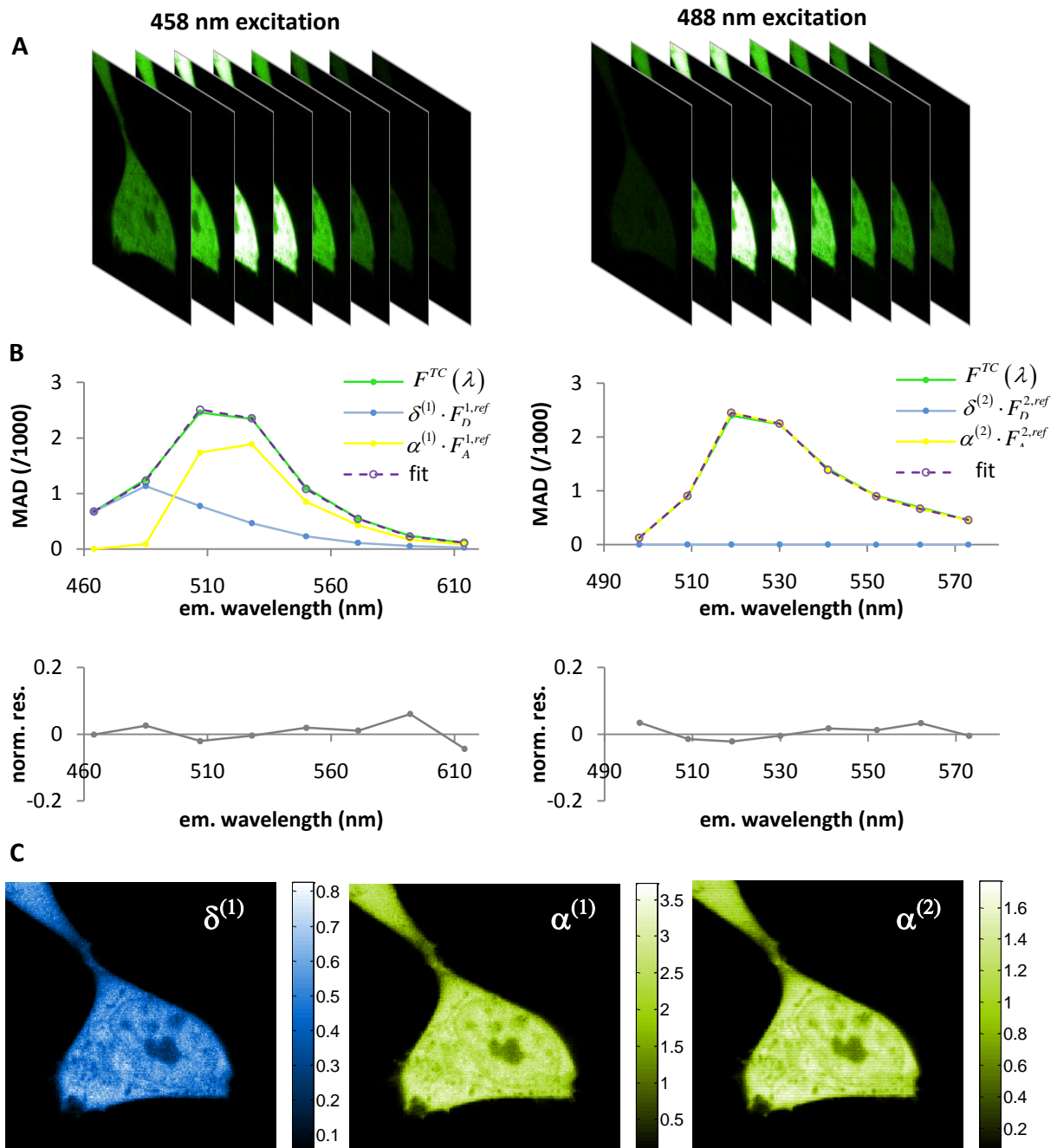


Figure 3.8 | Per pixel linear unmixing and determination of apparent concentration maps. A) Spectral images of the CFP-YFP FRET reference were measured with excitation at 458nm and at 488nm. B) Emission spectra constructed for each pixel. Separation of donor and acceptor contributions is performed using linear unmixing of the donor and acceptor reference spectra. C) From the unmixing procedure, donor and acceptor apparent concentrations are determined for each pixel of the image.

The apparent concentrations can be used along with the calibrated excitation ratios to determine the luxFRET quantities according to equations 1.24 - 1.26. Performing this on a per pixel basis allows for the computation of spatial maps of all the luxFRET values. Figure 3.9 parts A and B represent the spatial distributions of the apparent FRET efficiencies E_{f_D} and E_{f_A} . Part C illustrates the map of FRET corrected total acceptor to total donor ratio values. Part D and E show the FRET corrected total donor and total acceptor concentrations as factors of the corresponding reference concentrations.

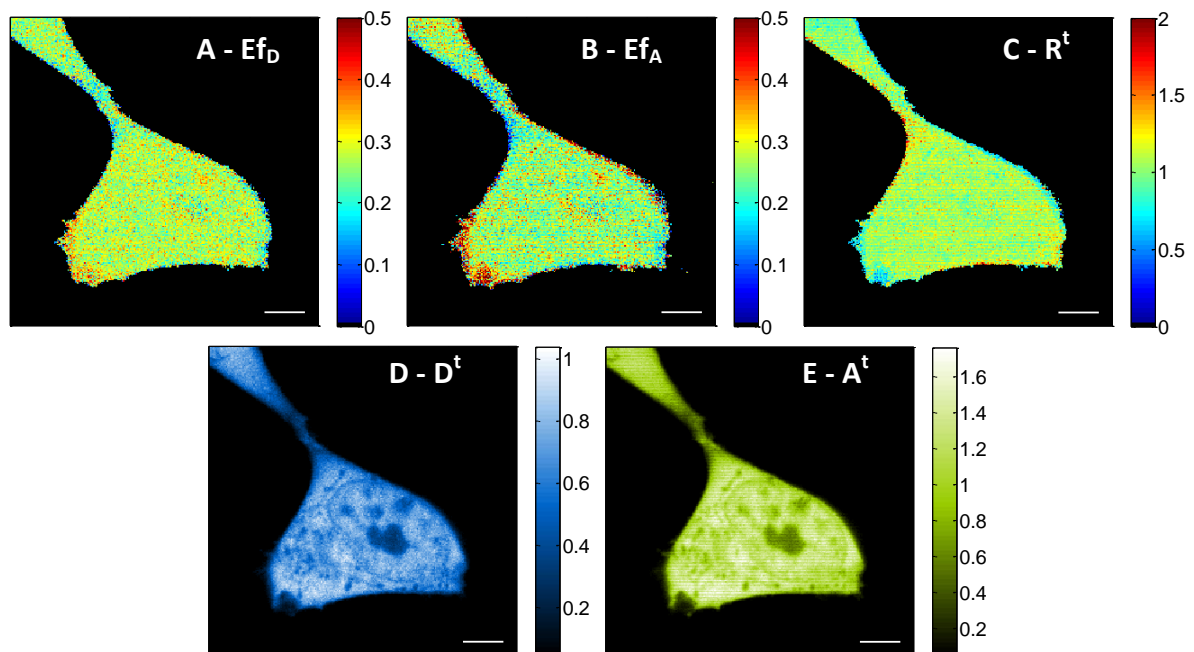


Figure 3.9 | Determination of luxFRET quantities. Using the spatial distribution of apparent concentrations, the luxFRET quantities can be determined on a per pixel basis. A) The donor quenching related apparent FRET efficiency, E_{f_D} , is calculated from equation 1.24. B) The acceptor sensitization related apparent FRET efficiency, E_{f_A} , is determined from eq. 1.25. C) The map of FRET corrected total acceptor to total donor ratio values is calculated from eq. 1.26. D) and E) show the FRET corrected total donor and total acceptor concentrations as factors of the corresponding reference concentrations determined from eq. 1.22 and 1.23, respectively. The scale bar represents 5 μ m.

3.7 Analog detector calibration - determination of apparent single photons signal

In the following investigations we will explore the performance of different FRET estimators. We will also explore the propagation of photon shot noise through the different analysis methods. In order to perform this analysis such that inferences can be made regarding performance on various platforms, the SNR of the FRET estimators will be characterized for a given amount of collected photons. It is possible to estimate the number of photons collected by an analog detector through the analysis of the noise of the measured signal. Assuming the noise of fluorescence signals is dominated by photon shot noise, we can use Poisson statistics to develop a linear relationship between the variance of the intensity of detected fluorescence emission and the mean intensity (eq. 41). The mean and variance of detected fluorescence emission were measured from images of a uniform fluorescent polymer slide (see Methods). In consecutive measurements the excitation intensity was increased and the variance was determined for a range of mean intensities. This protocol was repeated for detector gains ranging from 300-700V in 50V increments.

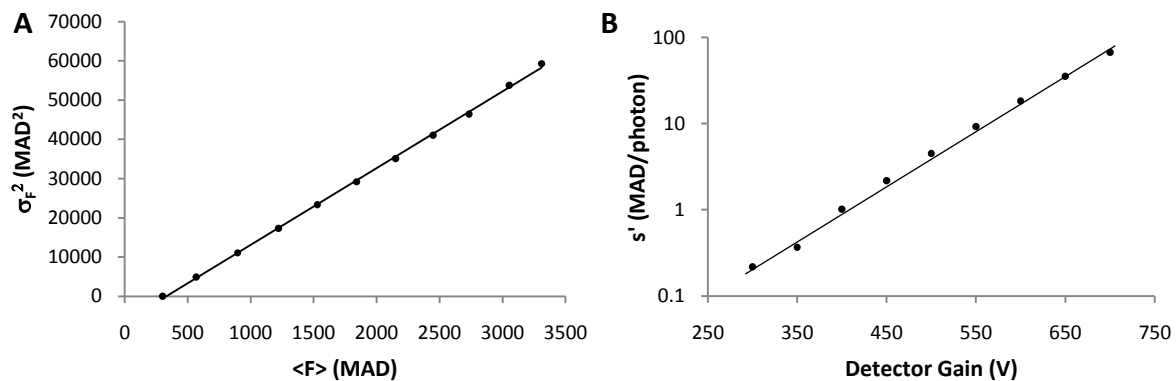


Figure 3.10 | Estimation of the apparent single photon signal. A) The mean and variance of the measured fluorescence emission intensity from the same region of interest in consecutive measurements are represented as solid circles. Values were obtained experimentally from multiple images of a fluorescent polymer microscope slide acquired with increasing 458nm excitation intensity and collection of emission from 464nm - 485nm wavelength. The solid line represents a linear fit to the model Eq. 1.41, with fitted parameters $s' = 18.3$. $\sigma_{o,i}^2 = 9.72$ was determined from the dark current measurement. The slope s' represents the apparent single photon signal and $\sigma_{o,i}^2$ is the background noise of channel used for a detector gain of 600 and a pixel dwell time of 12.80 μ s. B) The apparent single photon signal, s' , as a function of detector gain.

Figure 3.10 shows the best fit of eq. 1.41 to the measured variance of fluorescence intensities between 300 and 3500 Microscope AD-units (denoted as MADs below) for a detector gain of 600V. The slope of the linear fit to this data provides a value for the apparent single photon signal, $s' = 18.28$ MADs/photon. The first point, at the lowest intensity, was performed without excitation. It is a measurement of the dark current with its x-value representing the detector offset, 286 MADs, and the y-value represents the background detector noise, $\sigma_{o,i}^2 = 9.72$ MAD². Panel B of this figure shows s' as a function of detector gain.

Table 3.1 | Emission channel properties.

Channel (nm)	Offset (MADs)	σ_o^2 (MADs ²)	s' (MADs/photon)
464 - 485	296.04	9.66	18.29
486 - 507	300.57	11.57	19.56
508 - 528	293.66	10.51	19.27
529 - 550	300.10	9.92	19.31
551 - 571	296.37	8.94	16.10
572 - 592	291.78	8.79	15.80
593 - 614	297.24	7.74	17.68
615 - 636	290.21	10.65	20.26
Mean	295.75	9.72	18.28

The offset and background variance were determined from measurements of dark current (no excitation). The apparent single photon signal was determined from the mean – variance relationship of measurements of the uniform fluorescent polymer slide.

Similar results were obtained from measurements performed on N1E-115 cells expressing the CFP-YFP tandem construct. In these measurements an apparent single photon signal was determined for each emission channel used in the single excitation wavelength FRET measurements. Although photophysics would predict s' to be inversely proportional to wavelength (Neher and Neher 2004), s' and $\sigma_{o,i}^2$ were found to be relatively wavelength invariant as shown in table 3.1. For the luxFRET measurements presented later, the detector gain was typically set to 550 or 600V,

resulting in an apparent single photon signal of 9.2 or 18.3 MADs per photon, allowing for the detection of a maximum of approximately 225 or 500 photons per channel per 12-bit acquisition, respectively.

It was observed during preliminary measurements that there was a dependency of the apparent single photon signal on pixel dwell time (scan speed) used during the image acquisition. Generally higher apparent single photons signals were measured at faster scan speeds. It is assumed that the manufacture intended for this relationship so that the user could increase the SNR of a measurement by changing the pixel dwell time, collect more photons, without reconfiguring the detector gain and/or excitation intensity. It is not clear how this processing is handled however we have no evidence that it affects our analysis.

One feature that was uncovered that most certainly affects our estimation of the apparent single photon signal is a scan speed dependent correlation between pixels. Panel A of the figure 3.11 shows a background (without excitation) acquisition at a pixel dwell time of 0.80 us and gain of 700V. The detected speckles are assumed to be the result of collection of stray photons. As can clearly be seen in the image, a high intensity pixel often has a tail extending to the right, in the scan direction. Below this image, in panel B, a trace of a single line of the image is plotted. Just as in the image, the decay after initial peak is apparent in the scan direction. Autocorrelation of pixel intensities was measured. No correlation was measured in the y-dimension, however in the x-dimension, particularly in the scan direction a strong correlation between pixels was measured for fast scan speeds. The autocorrelation function in the scan direction is shown in figure 3.11 panel C for multiple pixel dwell times. The correlation was strongest with a pixel dwell time of 0.80 us and completely disappeared when measuring with a pixel dwell time of 12.8 us. It should be noted that the same correlation-pixel dwell time relationship was determined from measurements at lower detector gains using emission collected from a fluorescent polymer slide (fixed fluorescence reference sample, no autocorrelation from diffusion). The correlation of the signal effectively

distributes the signal resulting from a single photon detection over several pixels, blurring the acquired image, reducing the measured noise, and preventing one from determining an accurate estimate for the apparent single photon signal using photon statistics. In order to more correctly estimate the number of photons collected during an image acquisition. For these reasons a pixel dwell time no faster than 12.80 μs was used in further measurements.

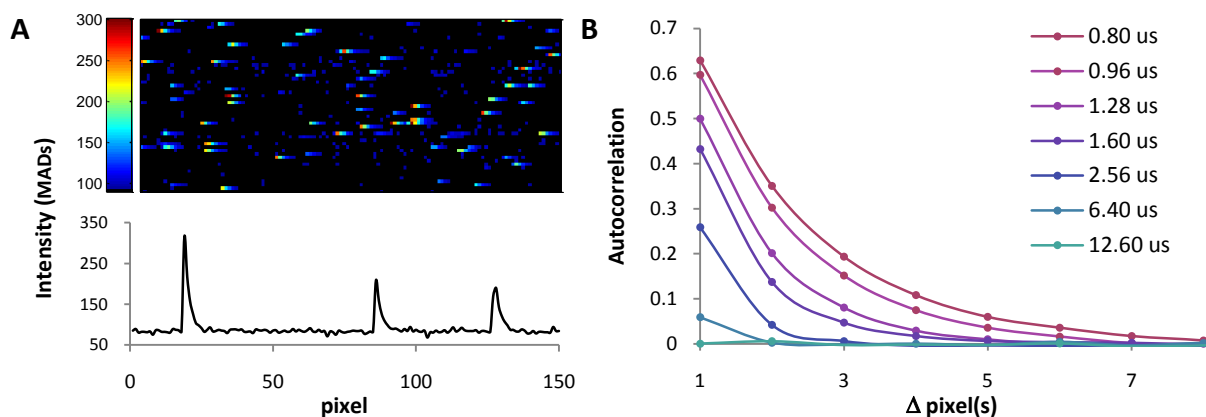


Figure 3.11 | Decay of single photon detection over multiple pixels – Autocorrelation of signal. A) An image of stray photons detected was acquired without illumination with a pixel dwell time of 0.80 μs . The intensity values of the center row of pixels of the image are plotted, showing that the signal resulting from a single photon detection decays over multiple pixels. B) Autocorrelation functions were determined for multiple pixel dwell times in the scan direction. Pixel 1 (x-axis) represents the nearest neighbor.

3.8 Characterization of noise in unmixed apparent concentrations

From photon statistics we would expect the SNR^2 of fluorescence intensity, whether it is photon number or MADs, to be linearly proportional to the mean of the intensity. This relationship is maintained through the spectral decomposition of fluorescence (eqs. 1.12 and 1.13) such that the SNR^2 of an unmixed apparent concentration is linearly proportional to the number of photons collected. As is shown in the error propagation equations (eqs. 1.46 - 1.51), many of the luxFRET quantities have CV^2 values which are linearly proportional to the sum of the CV^2 of the apparent concentrations used in their computation. By establishing the relationship between the SNR^2 of a

given apparent concentration and the number of photons at which it was detected, we should be able to make predictions about the SNR^2 of the luxFRET quantities at varied photon collection levels.

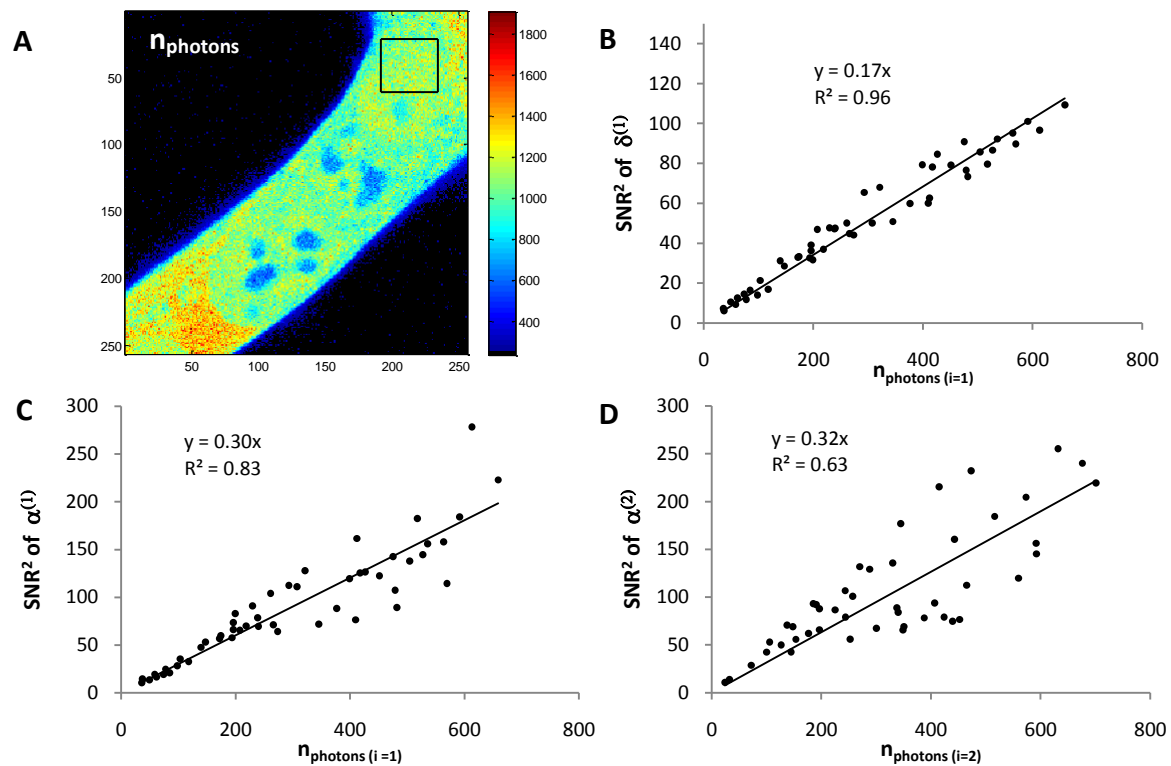


Figure 3.12 | SNR^2 of the apparent concentrations unmixed from the fluorescent emission as functions of the total number of collected photons. A) Regions of interests of uniform fluorescence intensity were sampled to determine the mean total number of photons collected as well as the SNR^2 of the unmixed apparent concentrations. B-D) The SNR^2 of the apparent concentrations were fit as a linear functions of the mean number of detected photons. The data was fit with a linear regression with the intercept fixed at 0.

Five HEK-293 cells expressing the fixed FRET efficiency CFP-YFP tandem construct were measured at five different excitation intensities over the emission channels used in the FRET measurements. Two regions of interest of seemingly uniform concentration were sampled from each cell for analysis. An example of a ROI from which quantities are measured is shown in figure 3.12 panel A. The number of detected photons is estimated by summing the ROI mean intensity of each channel and dividing by the apparent single photon signal. Linear unmixing was the performed on a per pixel basis, as described previously, such that images of the apparent concentrations are obtained. The mean and variance of the apparent concentrations were sampled from the same ROIs

as the raw fluorescence signal. The resulting SNR^2 of the apparent concentrations were then plotted against the estimated number of photons collected in figure 3.12 panels B-D. The data were then fit with a linear regression with the intercept fixed at the origin. The relationships indicated by these regressions (in figure 3.12) were inverted to characterize the CV^2 of the apparent concentrations, such that they could be used directly in the error propagation equations.

$$CV_{\delta^{(1)}}^2 = 5.88 \cdot n_{p,1}^{-1}, \quad CV_{\alpha^{(1)}}^2 = 3.33 \cdot n_{p,1}^{-1}, \quad CV_{\alpha^{(2)}}^2 = 3.13 \cdot n_{p,2}^{-1}. \quad 3.1, 3.2, 3.3$$

The variances of the unmixed apparent concentrations can also be predicted from a single set of reference spectra and a single sample spectrum according to eqs. 1.43 – 1.45 (Neher and Neher 2004). The mean ROI intensity of each channel of the samples used above were used to make a sample spectrum. Together with the same reference spectra, these sample spectra were used to predict the variance of the apparent concentrations. In figure 3.13 panel A, the measured and estimated variance of $\alpha^{(1)}$ are plotted against the estimated number of photons collected. These data indicate that the measured variance is greater than the estimated. Figure 3.13 panel B-D, show the correlation between the measured and estimated variance of $\alpha^{(1)}$, $\delta^{(1)}$, and $\alpha^{(2)}$, respectively.

These figure show that, as would be expected, the measured variance is slightly greater than the estimated variance. Taking a closer look at this, we see a very strong correlation between the measured and estimated variance in figure 3.13. In the case of $\alpha^{(1)}$ we see that the estimated variance is consistently 73.2% that of the measured. In the case of $\delta^{(1)}$ the estimated variance is 83.3% that of the measured variance. The same comparison was performed for the unmixing of the acceptor apparent concentration from the emission detected during the 488nm excitation. Donor emission with excitation at 488nm is negligible, is not necessary for luxFRET analysis, and thus was not considered. There seems to be much more variance in $\alpha^{(2)}$ at larger photons counts than is expected, leading to a loss of linear correlation compared to the previous cases. These measurements verify that the estimates may be used to predict the noise expected in the apparent concentrations and thus in the FRET estimators without the need of multiple sample measurements.

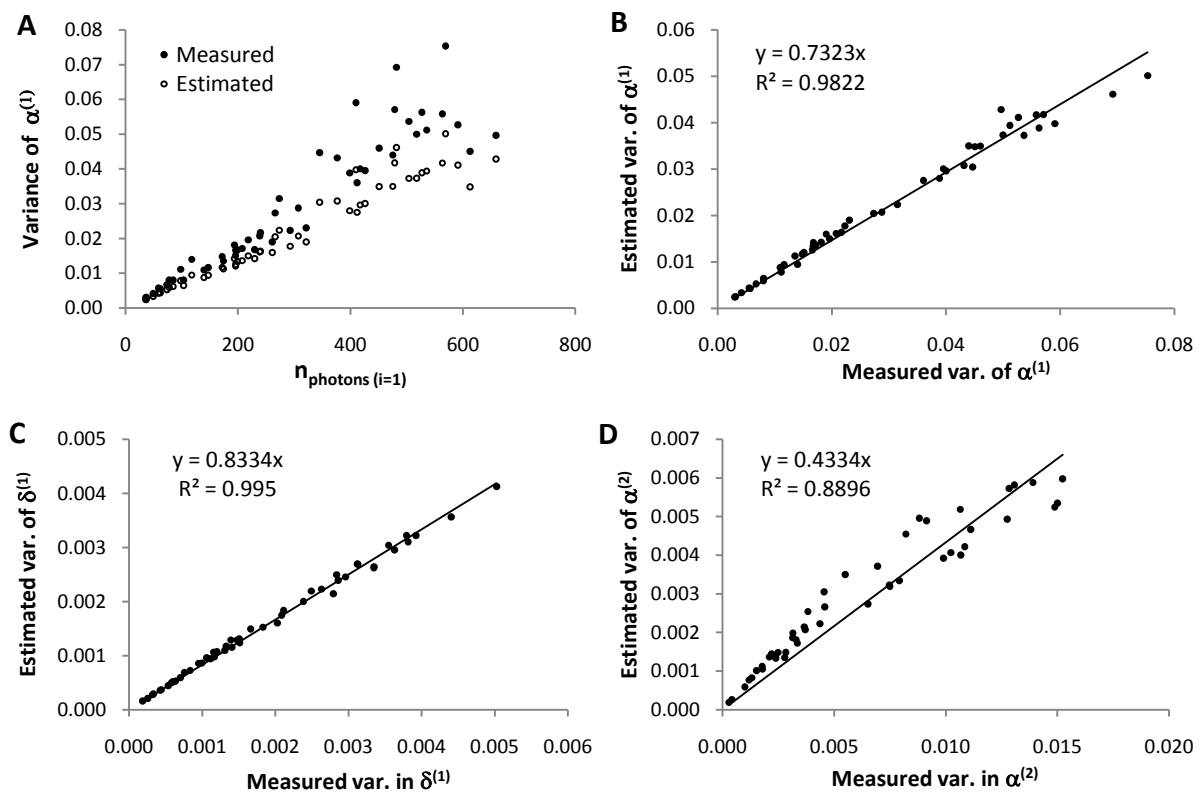


Figure 3.13 | Measured and estimated variance of the unmixed apparent concentrations. Panel A illustrates the measured and estimated variance of $\alpha^{(1)}$ as a function of the total number of photons collected. Panel B indicates the strong correlation of these two variances (a squared coefficient equal to 0.98). Panel C indicates the strong correlation between the measured and estimated variance of $\delta^{(1)}$ (a squared coefficient equal to 0.995). Panel D shows the correlation of the estimated and measured variance of $\alpha^{(2)}$, with a squared correlation coefficient, R^2 , equal to 0.89.

3.9 Use of error propagation to predict SNR^2 of FRET estimators.

3.9.1 FRET imaging of an Epac-based cAMP sensor

Two confocal images of N1E-115 cells expressing a Cerulean-Epac-Citrine FRET sensor were acquired with 458nm and 488nm excitation, respectively, each over 8 emission channels. These images were first brought into register. Then the apparent concentrations of cerulean, the donor, and citrine, the acceptor, at each pixel were determined by non-negatively constrained linear unmixing using previously determined reference spectra. With these apparent concentrations, as well as some

calibration constants, the luxFRET quantities defined in eqs. 1.37 - 1.40 were computed, resulting in images representing the spatial distribution of these quantities. A ratiometric FRET estimator, the 550/485nm emission ratio, was also computed using selected emission channels from the 458nm excitation fluorescence acquisitions. The resulting images are presented in Fig 3.14. The left column (panels A and B) represent the raw data, which are the sum of the emission collected in the two acquisitions (top panel, A) and the 550/485nm emission ratio derived in a way similar to that of Miyawaki et al 1999 (lower panel, B). The total emission is expressed in terms of the number of collected photons by dividing the fluorescence intensity by the apparent single photon signal, s' , derived from equations 1.41. The top panel, C, of the center column shows the quantity Ep_d' , calculated according to equation 1.37 or its simplified form equation 1.40 (the two are equivalent). These quantities are based on the measurement of acceptor fluorescence only, comparing sensitized emission ($\alpha^{(1)}$) with directly excited emission ($\alpha^{(2)}$). It is quite obvious that these images contain more noise than the images of the emission ratio. The bottom panel of the center column, panel D, shows the quantity Ep_a according to equation 2. The right column shows Ep_a according to equation 3 with $i=1$ (top panel, E) and for $i=2$ (bottom panel, F). The first version ($i=1$) is very similar to the simple emission ratio (panel B), except that it is calibrated in terms of Ep_a and that the emissions have been obtained by spectral decomposition rather than from two suitable spectral windows. The SNR is better than that of the acceptor based analysis (panel C) but not quite as good as that of the plain ratio. Finally the second version with $i=2$ (panel E) calculates the ratio of directly excited acceptor emission over directly excited donor emission. It definitely has the lowest SNR and also some bias.

In the images produced from analysis modes that require information from two excitations (figure 3.14 panels C, D, and F) there are frequent edge effects due to slight, often sub-pixel, mis-registration. Apart from that, the mean FRET efficiency is reasonably uniform throughout the entire cell. However, as will be discussed in greater detail later, the noise varies between regions due to differences in the amount of the sensor and the number of collected photons.

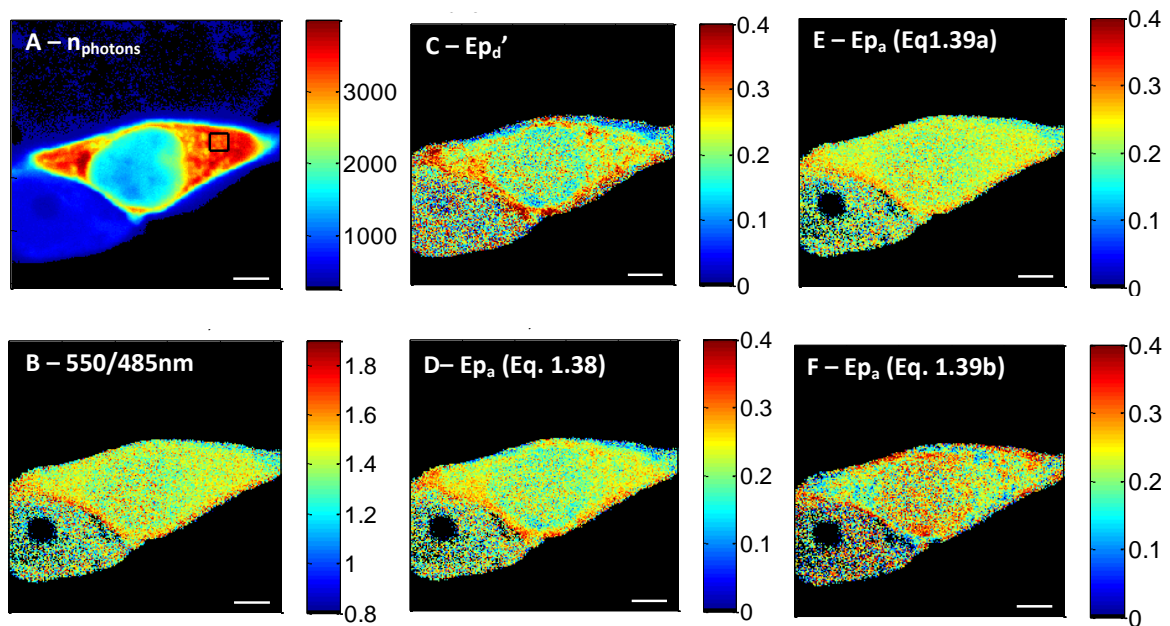


Figure 3.14 | Comparison of images analysis methods. Confocal images of N1E-115 cells expressing an EPAC based cytosolic cAMP FRET sensor were analyzed with the various luxFRET and ratiometric methods. **A)** The apparent single photon signal was used to estimate the number of photons detected during a sequence of 2 excitations. This number detected within the ROI, shown as a black box, was found to be 3,736 photons per pixel. **B)** The YFP to CFP emission ratio was estimated as the ratio of emission in the $550\pm 21\text{nm}$ and $485\pm 21\text{nm}$ spectral windows. **C)** Using information from two image acquisitions, with excitation wavelengths 458nm and 488nm, Ep_d' was calculated using equation 1.37 or equation 1.40, the two are equivalent. **D)** Ep_a was calculated from dual excitation measurements according to equation 1.38. **E)** Ep_a was calculated from a single acquisition using equation 1.39 with $i = 1$, and R^t as a calibration constant. **F)** Ep_a was also calculated from the two-excitation wavelength measurement using equation 1.39 with $i = 2$. To allow for comparison of the luxFRET quantities to the ratiometric measurement the color scales were adjusted appropriately. Scale bars represent $5\mu\text{m}$.

Figure 3.15 provides a quantitative analysis of the SNR of the images of figure 3.14. A small region of interest was selected (shown as a black box in figure 3.14 A) and the mean of pixel values as well as the variance between pixels was calculated. Subsequently the signal-to-noise ratio was determined. This is a dimensionless and scale invariant quantity. It allows us to directly compare the level of noise present in each measurement, if the quantities analyzed are sufficiently constant over the ROI. The mean estimated per pixel photon count (Figure 3.14) within the selected ROI is 3,167 photons (see methods). Although the signal is not completely uniform within this ROI, the non-

uniform concentration should not affect the variance measurement for the derived quantities since they involve only ratios of two quantities, each of which scales with signal strength. The SNR values sampled from the quantities illustrated in figure 3.14 are compared in Figure 3.15. This shows, as was concluded from figure 3.14, that eq. 1.39 ($i=1$) provides the best SNR of the luxFRET quantities and that the 550/485nm emission ratio provides the overall best SNR in this example. Differences between the different analysis modes will be discussed in greater detail later.

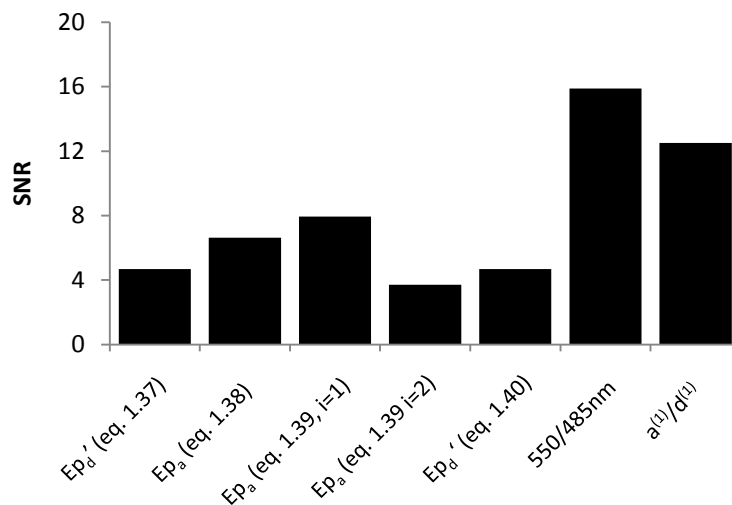


Figure 3.15 | Comparison of the FRET indicators. The SNR measured from corresponding ROIs of the quantities imaged in Figure 3.14 are shown in this bar graph. The results indicate that the 550/485 nm ratio provides a more favorable SNR than any of the luxFRET quantities. The luxFRET quantity with the most favorable SNR is Ep_a calculated with Eq. 1.39 ($i=1$).

3.9.2 Dependence of SNR^2 of FRET estimators on the number of detected photons & FRET efficiency.

To develop the relationship between the SNR^2 of our luxFRET quantities and the excitation intensities, we performed multiple measurement of a CFP-YFP tandem construct at varied excitation intensities. The measured SNR^2 of the apparent concentrations, $\alpha^{(1)}$, $\alpha^{(2)}$, and $\delta^{(1)}$, were fit as linear functions of the estimated number of detected photons (see figure 3.12). These values were compared to those determined with eqs. 1.43-1.45 and were found to be in good agreement in figure 3.13.

A thought-experiment was then performed, in which the values for $\delta^{(1)}$ and $\alpha^{(i)}$ were taken from the measurement shown in Figure 3.14 (with an Ep_o of 0.23, $n_1 = 1,456$ photons collected in 458nm excitation acquisition and $n_2 = 1,711$ photons collected during the 488nm excitation acquisition) and calculated the SNR^2 -values according to equation 1.48. We simulated changes in excitation intensity by varying proportionally the number of photons collected. In these calculations the $\delta^{(1)}$ and $\alpha^{(1)}$ values were assumed to be constant (since they are normalized for intensity changes) and their CV^2 -values to vary according to the above mentioned linear fitting.

The results of these calculations are shown in figure 3.16 panel A. As would be expected, the SNR^2 of Ep_o increases with the number of detected photons for both excitations. Interestingly, this figure suggests that the number photons collected during the respective excitations do not contribute equally to the SNR of Ep_o . The contour plotted across the surface in figure 3.16 panel A represents the predicted SNR^2 of Ep_o for all measurements in which a total of 3,167 photons are collected during the two excitations. The maximum of this contour, illustrated as the point atop the solid vertical line, occurs when approximately 63% of the total photons are collected during the 458nm excitation. The open circle, together with the dotted vertical line, represents the measured SNR^2 of Ep_o sampled from figure 3.14 panel D. In that experiment only 46% of total photons were collected during the short wavelength. This figure suggests that the SNR^2 of Ep_o could have been improved by approximately 12% by increasing excitation 1 at the expense of excitation 2. There is a second reason why it may be advantageous to use lower intensity in the long wavelength excitation, particularly at high FRET efficiencies. This relates to the fact that the acceptor is subject to bleaching during both excitations and, therefore, its bleaching may be limiting. This point will be addressed in more detail in the discussion.

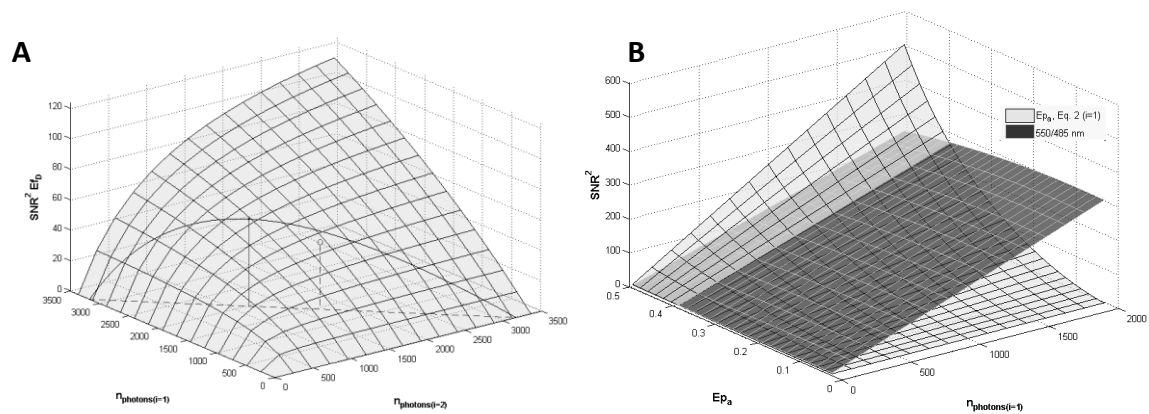


Figure 3.16 | Dependence of SNR^2 of FRET indicators on the total number of detected photons and FRET efficiency. Fluorescence data were obtained using a CFP-YFP tandem construct and expectations for the SNR^2 were calculated from the error propagation analysis. **A)** SNR^2 of the 2-excitation dependent Ep_a calculated from Eq. 2 with error propagation calculated using equation 13. The contour plotted across the surface in figure 3A represents the predicted SNR^2 of Ep_a for all measurements in which a total of 3,167 photons are collected during the two excitations. The maximum of this contour, illustrated as the point atop the vertical line, occurs when approximately 63% of the total photons are collected during the 458nm excitation. The open circle represents the SNR^2 of Ep_a measured when 45% of the 3,167 photons were collected during the short wavelength excitation. **B)** Comparison of the SNR^2 of Ep_a and the SNR^2 of the 550/485nm emission ratio for different FRET efficiencies and numbers of detected photons. These results show that the SNR^2 of the ratiometric measurement exceeds that of the luxFRET quantity for the FRET efficiencies expected from most FRET sensors. However, this figure proposes that at relatively high FRET efficiencies, above approximately 0.38, the SNR^2 of Ep_a will begin to exceed that of the 550/485nm ratio.

To determine the effect of changes in FRET efficiency on the SNR^2 of the measurements, we estimated the SNR^2 for the hypothetical case in which the FRET efficiency of a sensor changes at constant total acceptor to total donor ratio. If we change the value of $\alpha^{(1)}$ while keeping $\alpha^{(2)}$ constant, the value of $\delta^{(1)}$ must change in order to maintain the constant ratio according to equation 1.26. These new apparent concentrations correspond to a new FRET efficiency. This iteration was repeated such that apparent concentrations corresponding to a range of FRET efficiencies were determined. These apparent concentrations were used along with eq. 1.39 ($i=1$) to calculate the gray semi-transparent surface in Figure 3.16 panel B, illustrating the relationship between the SNR^2 of Ep_a and the total number of detected photons. The linear relationship between SNR^2 -values of the apparent concentrations and the number of collected photons, as above, was also used (this

neglects small changes in noise, which may result from various degrees of spectral overlap). The same relationship for the SNR^2 of the 550/485nm emission ratio measurement is illustrated as a semi-transparent dark gray surface with a white grid. We present these two quantities since they were found to have among the highest SNR^2 (figure 3.15) and because they can both be determined from single excitation measurements. The figure clearly shows that the SNR^2 of both Ep_a and the ratio increase with an increase in the number of photons detected. For the majority of the figure the SNR^2 of the 550/485 ratio is greater than that of Ep_a . However, at relatively high FRET efficiency, greater than approximately 38%, the SNR^2 of Ep_a begins to exceed that of the ratio.

3.9.3 Time series measurements of select FRET estimators

As previously mentioned, Ep_a , from Eq. 1.39 ($i = 1$) and the 550nm/485nm emission ratio only require a single excitation acquisition, making them especially well suited for measuring dynamic changes in FRET. It should be reiterated that Ep_a (Eq. 1.39, $i=1$) does require the knowledge of R^t , which can only be obtained by a two excitation measurement. R^t , the ratio of total donor and total acceptor concentration, should however be constant for a given tandem construct, except for possible differential bleaching. Therefore, in order check for such consistency, we performed two-excitation measurements preceding and following multiple single excitation measurements, as described in Methods. Figure 3.17 illustrates such a measurement performed on the same cells expressing the cerulean-EPAC-Citrine cAMP sensor, as shown in Figure 3.14. Forskolin, a membrane permeable activator of adenylyl cyclase (AC), was applied at a final concentration of 10 μM at $t = 200\text{s}$. The increase in [cAMP] resulting from the forskolin induced activation of AC is shown in figure 3.17 as a decrease in the measured Ep_a from approximately 0.23 to 0.11 (dark trace, left ordinate). Correspondingly, the decrease in donor quenching and acceptor sensitization results in a decrease in the 550nm/485nm emission ratio from approximately 1.43 to 1.09 (light trace, right ordinate).

In this example the initial R^t , which is used as a calibration constant throughout the time series, equals 1.82. The value of R^t computed following the time series equals 1.77, suggesting

relatively little differential bleaching. The total acceptor concentration, A^t , changes from 1.17 to 1.09, indicating that approximately 7% of the 60% change measured in Ep_a results from acceptor bleaching. The total donor concentration changes from 0.64 to 0.62 fold that of the donor reference concentration throughout the course of the measurement and only influences Ep_a indirectly through the differential bleaching present in R^t .

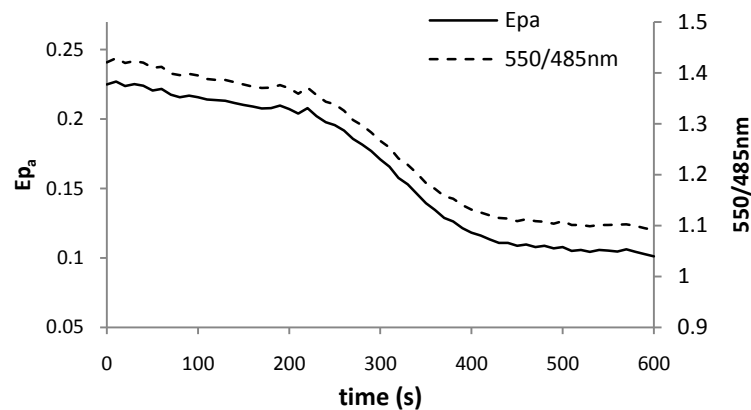


Figure 3.17 | Time course of Ep_a and the 550/485nm emission ratio. Multiple single excitation measurements of cells expressing the cerulean-EPAC-citrine cAMP sensor shown in figures 1 and 2 were performed after an initial two-excitation measurement. Forskolin was applied to a final concentration of $10\mu\text{M}$ at $t = 200$ seconds. **A)** The values calculated for Ep_a and the 550/485nm ratio are plotted over time as solid and dashed lines, respectively. Note the different scales for the two quantities.

3.9.4 Effect of FRET change and bleaching on Ep_a and its SNR^2

During the course of the measurement shown in figure 3.17, not only is there a decrease in FRET efficiency resulting from the increase in [cAMP], but there is also a gradual decrease in the number of detected photons resulting from the photobleaching of both the donor and acceptor fluorophores. Intuitively, both of these factors will contribute to a decrease in the SNR^2 of Ep_a . The error propagation analysis presented in figure 3.16 allows one to predict this effect. In figure 3.18, a subsection of the $\text{SNR}^2 Ep_a$ surface in figure 3.16 is presented as a light gray semi-transparent surface with a black grid. The solid black points in this figure represent the measured SNR^2 of Ep_a at the corresponding values of Ep_a and mean detected photons. The open circles represent the projection

of each sampled measurement onto the prediction surface. Twelve equally spaced samples from the time course measurement are plotted to illustrate the trend. This figure shows that the decrease both in FRET efficiency and in the number of detected photons over time, results in a decreased SNR^2 of E_{p_o} that is quite well predicted by theory.

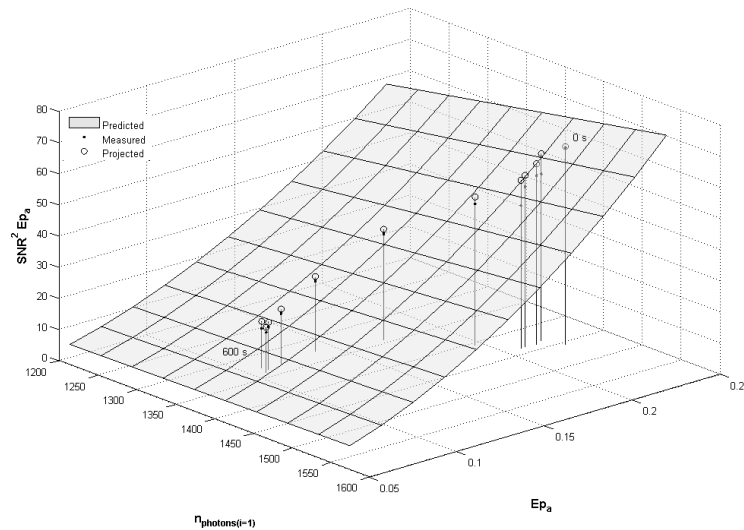


Figure 3.18 | Change in SNR^2 of E_{p_a} over multiple measurements. Twelve points were sampled, in fifty second intervals, from the E_{p_o} measurements presented in Panel A. The SNR^2 of these measurements were plotted as solid points against the corresponding FRET efficiency and number of detected photons. The gray surface is a subsection of the surface presented in figure 4B and represents the relationship between SNR^2 of E_{p_o} , FRET efficiency, and number of detected photons as predicted from the error propagation analysis. The open circles represent the projection of each sampled measurement onto the prediction surface.

3.9.5 Estimation of Ligand concentration

Measurements, such as those presented thus far, are often used only to indicate relative changes in the concentration of a ligand, in this case [cAMP]. However, it is possible to estimate the absolute ligand concentration from measurements, if the maximum and minimum FRET efficiencies (E_{max} and E_0), corresponding to the sensor in its free and bound states are known, together with the Hill coefficient and the dissociation constant. Likewise, [cAMP] can be calculated from the simple emission ratio, if the corresponding maximum and minimum ratios are known (Gryniewicz et al. 1985). Literature values for the K_d of this construct vary greatly (Ponsioen et al. 2004; Salonikidis et

al. 2008), so no absolute estimate was made. From now on $[cAMP]/K_d$ will be designated as $[cAMP]^*$. For the following discussion we assume, for simplicity, that $p_{a,i} = 1$ and bleaching to be negligible. In the case of the Cerulean-EPAC-Citrine FRET sensor, $E_{free} = 0.23$, $E_{bound} = 0.45$, and Hill coefficient $n = 0.99$ (Salonikidis et al submitted). The 550/485nm emission ratios expected on our microscope that correspond to the free and bound states of the sensor were determined from the corresponding FRET efficiencies and found to be 1.44 and 0.95, respectively. The error propagation resulting from the conversion of FRET efficiency into ligand concentration is described by eq. 1.50. Eq. 1.51 describes the error propagation resulting from the conversion of emission ratio into ligand concentration. Maps of $[cAMP]^*$ were computed from the Ep_a and 550/485nm ratio maps. The SNR^2 was calculated as previously discussed.

The mean $[cAMP]^*$ can be calculated in two ways. We can either convert individual pixel values from Ep_a (or 550/485nm) to $[cAMP]^*$ and subsequently take the average of the ROI or we can take the mean Ep_a (or 550/485nm) and convert it to $[cAMP]^*$. In figure 3.19 panel A, we show the time-course of $[cAMP]^*$ calculated by the both these strategies. The black line represents the $[cAMP]^*$ calculated from the individual Ep_a values and the gray line represents that calculated from the individual 550/485nm emission ratio. Both these traces show an increase in $[cAMP]$ to approximately 3 fold the K_d value. The dashed trace illustrated in panel A represents the $[cAMP]^*$ value calculated from the latter method (from the mean Ep_a). This trace suggests that $[cAMP]$ only increases to 2.25 fold of the K_d value. In panel B we show the SNR^2 of $[cAMP]^*$ using the former strategy in which individual per pixel values of $[cAMP]^*$ are calculated from Ep_a , (black trace) and from 550/485nm (gray trace). This figure shows that the SNR^2 begins to increase as the emission ratio or Ep_a begins to diverge from the ligand free value, as equations 1.50 and 1.51 would suggest. However, over time the SNR^2 of $[cAMP]^*$ decreases dramatically due to bleaching, the decrease in FRET efficiency, and convergence upon the fully bound FRET estimator value. Interestingly, even though the SNR^2 of the 550/485nm ratio is significantly greater than that of Ep_a , the SNR^2 of the $[cAMP]^*$ estimation from these two quantities are essentially equivalent.

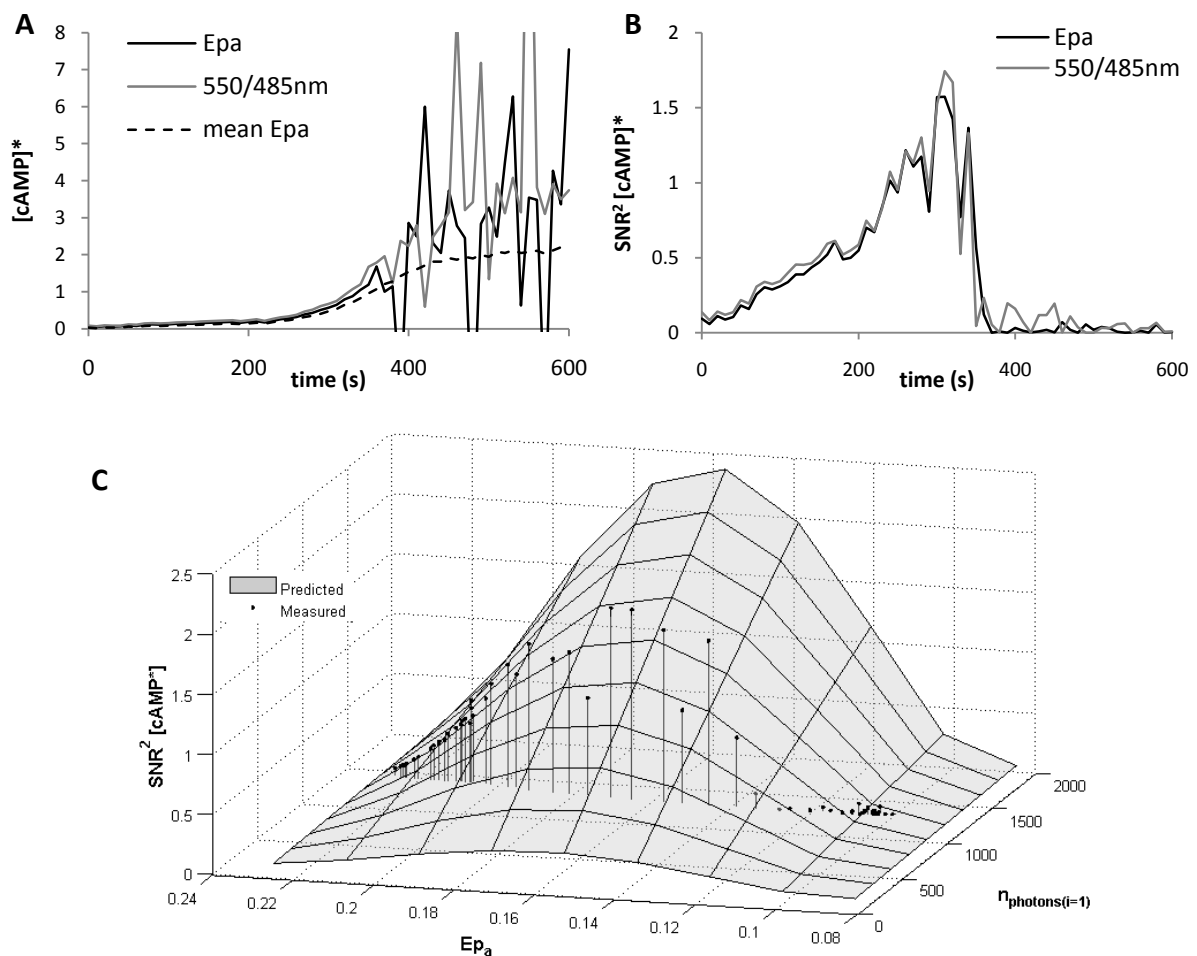


Figure 3.19 | Time course of the estimated cAMP concentration. With the knowledge of certain calibration parameters the absolute ligand concentration can be readily calculated. **A)** The solid black line represents the mean of the per pixel [cAMP]* values, derived from the per pixel Ep_o values. The dashed line corresponds to a similar measurement with the [cAMP]* map calculated from the per pixel 550/485nm ratio values. The solid gray line represents a case in which error propagation is neglected and the mean [cAMP]* calculated using the mean Ep_o . **B)** The solid and dashed lines represent the SNR^2 of the measurements from the [cAMP]* maps based on Ep_o and 550/485nm emission ratio, respectively, over time. **C)** The relationship between the SNR^2 of the [cAMP]*, the FRET efficiency of the sensor, and the number of detected photons is represented by the gray surface. The black points indicate the individual estimates from the measurements of the time series. This figure shows, similarly to figure 4B, that the error propagation model accurately predicts the expected SNR^2 .

Part C of the figure shows the relationship between the number of detected photons, the FRET efficiency of the sensor, and the SNR^2 of the [cAMP]* estimate, derived from our error

propagation analysis using eq. 1.50. The black points indicate the time course of our measurement. This figure shows, similarly to figure 3.18 that our error propagation model accurately predicts the expected SNR^2 . It clearly shows the increase in SNR^2 of the [cAMP]* estimate as the FRET efficiency decreases from that of the ligand free state. As equation 1.50 suggests, this figure also shows that the SNR^2 ($1/\text{CV}^2$) decreases to 0 when FRET efficiency begins to approach that of the bound state. Also, as would be expected, the model indicates the coordinated decrease of the SNR^2 of [cAMP]* with that of the number of detected photons.

3.9.6 Biasing resulting from Error propagation

In figure 3.19 we see that the apparent running average of the mean [cAMP]* measured from the per pixel conversion is greater than the [cAMP]* converted from the mean $E\rho_0$. The reason for this discrepancy was not immediately clear, so a closer look was taken. It is reasonable to assume that negative [cAMP]* values could be calculated due to error propagation, although negative concentration is not physically possible. If these pixels were not allowed in the analysis and set to zero or neglected, the mean calculated over the ROI would be greater and contain less noise than it should. To show that negative values are in fact allowed and used in the computation of mean [cAMP]*, the distributions of pixel [cAMP]* values are presented for multiple time points (and FRET efficiencies) in figure 3.20.

Not only do these distributions show that negative pixels are used in the computation of mean [cAMP]* but they also clearly indicate the increase in noise over time. The shape of the distributions indicate that either there is a low [cAMP]* cut-off (possibly resulting from intensity thresholding) or there is a significant skew in the distributions. No cut-off was used in the analysis. Furthermore the cut off required to explain the shape of the distribution seems to change over time suggesting that the distributions are rather skewed.

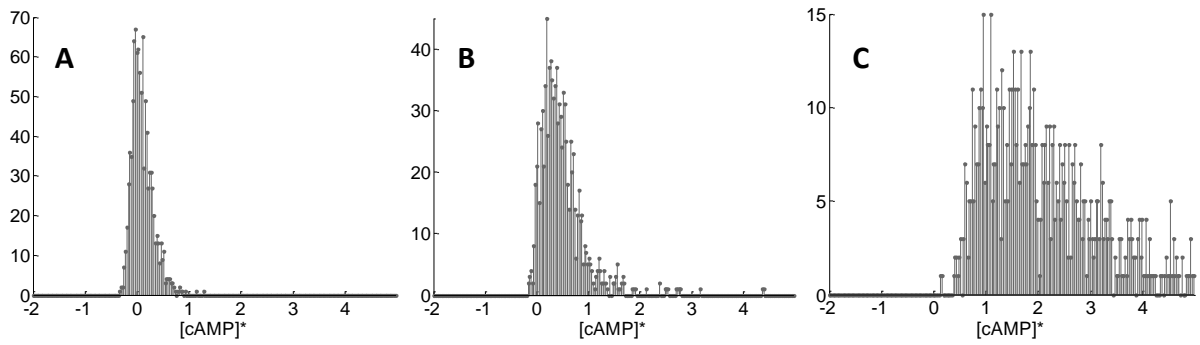


Figure 3.20 | Distribution of [cAMP]* values within the sampled ROI. Histograms of per pixel values are plotted from the same ROI used in the previous analysis. Panel A represents the [cAMP]* distribution at 100 seconds when Ep_o is approximately 0.22. This distribution shows that negative values exist and are used in the computation of mean and error of [cAMP]* within the ROI. Panel C represents the [cAMP]* distribution at 600s when Ep_o is approximately 0.11. The intermediate panel (B) illustrates the [cAMP]* distribution at $t = 300s$.

The values of Ep_o and the 550/485nm ratio are relatively normally distributed (not shown). The conversion from Ep_o to [cAMP]* must then somehow skew the distribution. Equation 3.4, describes how the conversion from E (or Ep_o) to [cAMP] is performed.

$$[cAMP] = K_d \left(\frac{E - E_{Free}}{E_{Bound} - E} \right) \quad 3.4$$

This conversion is non-linear, and accordingly a linear conversion of distributed data should not be expected. Figure 3.21 illustrates this relationship (eq. 3.4) as dark line. This relationship indicates that negative values may occur beyond the ‘free’ and ‘bound’ FRET efficiencies indicated as the vertical dashed lines at $Ep_o = 0.24$ and $Ep_o = 0.04$, respectively. This figure also shows two simulated distributions which represent Ep_o values similar to those measured before (mean $Ep_o = 0.22$) and after activation of AC (mean $Ep_o = 0.12$).

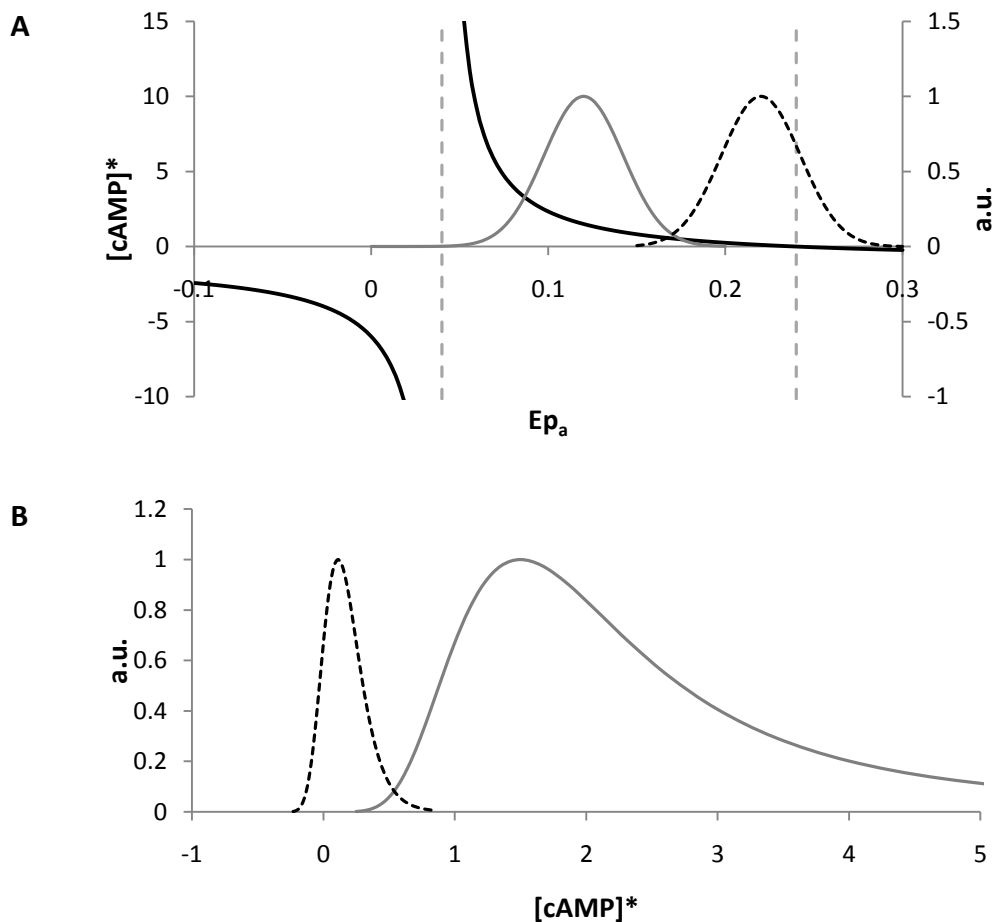


Figure 3.21 | Conversion from Ep_a to [cAMP]*. A) The dark black trace indicates the [cAMP]* as a function of E described by Eq. 3.5 (left ordinate). The dashed vertical lines at $Ep_a = 0.04$ and $Ep_a = 0.24$ correspond the 'bound' and 'free' state Ep_a values, respectively. The dashed distribution simulates the Ep_a expected at low concentrations of [cAMP] with the mean $Ep_a = 0.22$. The gray distribution simulates the expected Ep_a distribution of Ep_a at elevated [cAMP] when the mean $Ep_a = 0.12$. B) The dashed and gray [cAMP]* distribution correspond to the dashed and gray Ep_a distribution in the previous figure.

By projecting the Ep_a distributions in figure 3.21 onto the line representing the E to [cAMP]* conversion we can convert them to corresponding distributions of [cAMP]*. Figure 3.21 panel B shows that this conversion skews normally distributed E data from figure 3.21 panel A. This is most apparent with the gray distribution which corresponds to low Ep_a (high [cAMP]). The greater skew in the high [cAMP]* arises from the overlap of the low Ep_a distribution with a more non-linear region of the conversion function. In the case of a linear conversion we would expect an increase or decrease the standard deviation corresponding to a change in units however no skew in the data should

occur. It should be noted that these distributions correspond quite well with those measured at comparable Ep_a values (first and last panels of figure 3.20).

3.9.7 Comparison of dynamic range to noise

The ability of Ep_a and the 550/485nm ratio to be converted to [cAMP]* with the same SNR suggests that either the error propagation for Ep_a is more favorable than that of the emission ratio or that the SNR of these parameters insufficiently characterizes their ability to resolve changes in FRET. In such a case the SNR of these quantities would not directly comparable. The equations used to convert Ep_a and the emission ratio to [cAMP] were derived analogously and propagate error accordingly. Comparing the Ep_a and 550/485nm images in figure 3.14 the images appear to have similar levels of noise, with the color bars appropriately and proportionally scaled. However, we see in figure 3.15 that the SNR measured from the images differ greatly with SNR of Ep_a equal to 7.95 and the SNR of the emission ratio equal to 15.89. As was discussed earlier, SNR is unitless and scale invariant, it is not however offset invariant. If the amount of noise in two quantities is similar but one quantity has a higher basal level or offset it will also have a higher SNR, regardless of the response amplitude or dynamic range. In the case of the 550/485nm emission ratio, at $E = 0$, a signal of approximately 0.8 is measured. In this case what becomes important is not the amount of noise relative to the basal level or even absolute value, but the amount of noise relative to response from a change in FRET.

The relative change in a parameter can be calculated by dividing the deviation from the parameters mean initial value by this mean initial value. This normalizes all quantities to an initial value of one and allows us to more appropriately compare the relative dynamic ranges of each computed quantity. When this normalization is performed on a per pixel basis, using the mean initial value defined from a region of interest, it allows for the quantification of noise relative to this normalized value. This calculation was performed for the 550/485nm emission ratio, the apparent concentration ratio, and Ep_a in the example of the change in [cAMP]* shown above. A mean of these quantities was sampled from the same ROI used in the previous examples. Figure 3.22 below

shows that, as is expected, the mean relative change in Ep_a is the greatest. The change in the apparent concentrations is greater than in the emission ratio because the apparent concentrations are bleed-through corrected representations of the acceptor and donor. The acceptor component of the emission ratio, 550nm, still contains significant fluorescence from CFP. The variance of these quantities were also computed and are shown in figure 3.22 panel B to be relatively time invariant. As would be expected the noise in the calibrated measurement, Ep_a , is the greatest. Surprisingly, although it is computed with less photons the 550/485 nm ratio has a lower variance than the ratio of the apparent concentrations.

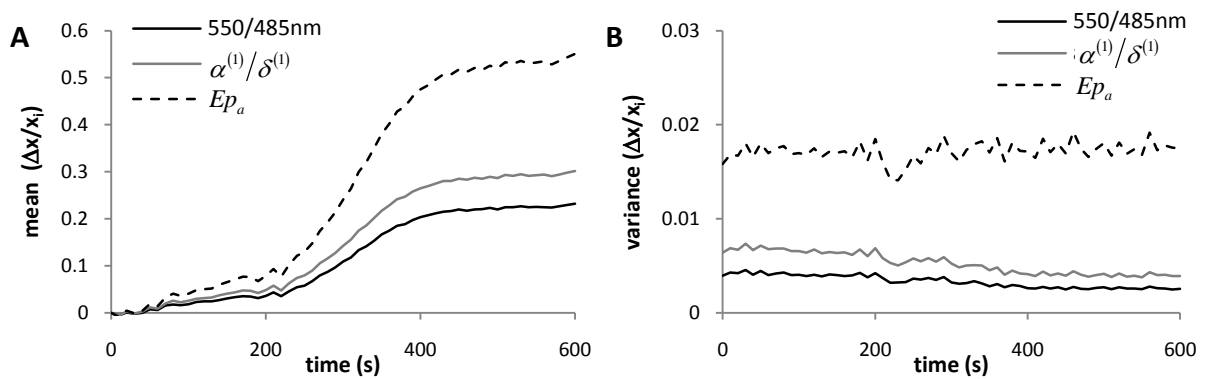


Figure 3.22 | Mean and variance of offset corrected FRET estimators. A) The ROI means of the relative changes in Ep_a , α^1/δ^1 , and the 550/485 nm ratio are plotted over time. B) The ROI variance of these quantities is shown to be relatively invariant over time.

When taking into consideration the relative dynamic range and the noise of a FRET estimator we can characterize its ability to resolve changes in FRET. When we compute the SNR of the relative change in these three FRET estimators, we see that they are all nearly equally well suited for identifying changes in FRET efficiency. Figure 3.23 indicates that although Ep_a does contain more noise, assumedly due to the error propagation resulting from the calibration of the apparent concentration ratio, its greater dynamic range resulting from directly characterization of the physical

parameter that is changing, E, the signal to noise is not much different than the FRET estimators that have much more favorable apparent noise levels.

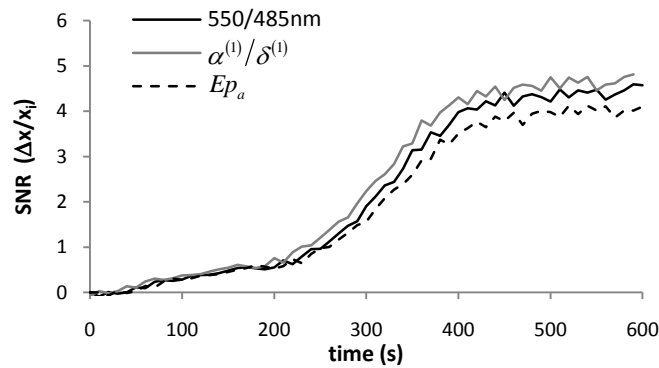


Figure 3.23 | Signal to noise of the relative changes in the FRET estimators. By measuring the signal to noise of the relative change in the FRET estimators we can quantify a measure of their ability to detect changes in FRET efficiency.

3.10 Optimization of additional imaging parameters

3.10.1 Optimal localization of emission channel boundaries

The error propagation analysis validated above provides a platform upon which the influence of additional imaging parameters on the SNR of FRET estimators can be predicted. This additional analysis that will be presented below, allows us to evaluate the feasibility of performing measurement on other platforms with different excitation wavelengths or spectral channels. Several of the error propagations equations introduced and validated above characterize the noise in the FRET estimators as directly proportional to the sum of the CV^2 of the apparent concentrations used. We have also demonstrated that the noise in the apparent concentration can be reasonably predicted by eqs. 1.43 - 1.45 with only knowledge of the reference spectra and an example of the sample spectra. By binning spectrally resolved sample and reference spectra and estimating the noise in the apparent concentrations, we can investigate the influence of channel number and location on the signal to noise of the luxFRET quantities calculated.

To separate the contributions to fluorescence from two fluorescent species, two channels are sufficient. To measure the optimal placement for the border of these two channels, simulated measurements were performed using high spectral reference (CFP and YFP) and sample (CFP-YFP) measurements acquired from 450 to 650nm in one nm increments. These spectra were then binned into two channels with the shared border placement ranging from 451-649nm. The error of the apparent concentrations for each simulation was predicted by eqs. 1.43 – 1.45. The normalized inverse of the sum of the CV^2 of the apparent concentrations was calculated and is shown as a function of the shared border location in figure 3.24. The inverse of the sum of the CV^2 is plotted because the maximum of this quantity clearly identifies the placement for optimal SNR of the FRET estimators. Plotting the normalized sum of the CV^2 of the apparent concentration (the quantity that is directly proportional to the CV^2 of the FRET estimators) results in a broad trough, from which the absolute minimum is difficult to identify. The maximum of the computed quantity is located at 509nm. This may seem trivial, as the optimal placement and separation of important spectral features is intuitive, however suggests that this method is valid and can be expanded for higher spectral resolutions.

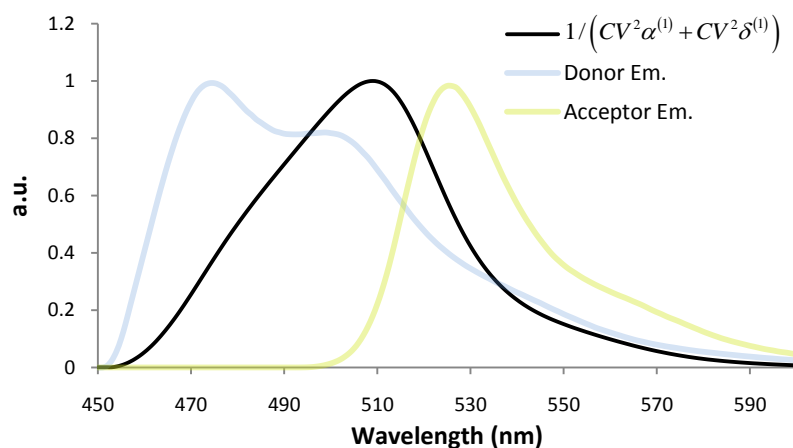


Figure 3.24 | Optimal location of window border for two emission windows. The inverse of the sum of the CV^2 of the unmixed apparent concentrations is maximized when the shared border of two sampling windows is located at 509nm. The normalized emission spectra of CFP and YFP are shown for comparison of optimal window border location and spectral features.

Similar simulations were performed for the case of three channels spanning the same emission range, 450-650nm. Figure 3.25 shows a map representing the normalized inverse of the sum of the CV^2 of the apparent concentrations for varied channel 1 and channel 2 widths. Although this figure only expresses the width of two channels, the width of the third is implied from the simulation's fixed bounds. This figure shows that, similarly to the optimization of two channels, optimal unmixing is performed with a border near 510nm (with a channel 1 width of 60nm or with the sum of the widths of channel 1 and 2 equal to 60nm).

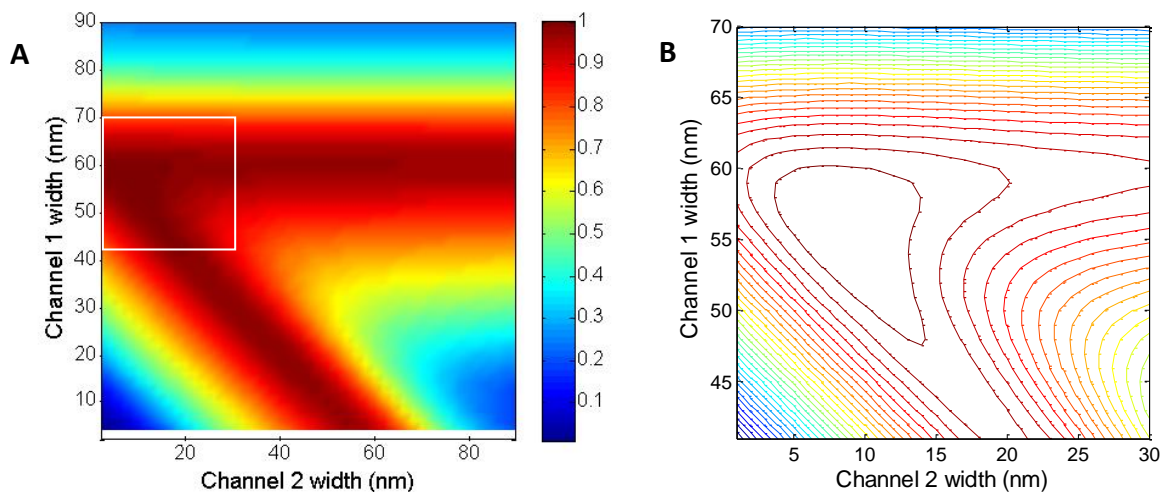


Figure 3.25 | Optimal location of window border for three emission windows. The normalized inverse of the sum of the CV^2 of the donor and acceptor apparent concentrations is shown as a function of the width of channel 1 and channel 2 in a three emission channel measurement. The total window is bound by 450nm and 650nm so the third emission channel is not a free parameter. Part A illustrates that, generally, a maximum inverse sum of apparent concentration CV^2 is achieved either with the channel 1-2 border near 510nm (450nm lower bound plus 60nm Channel 1 width) or with the channel 2-3 border near 510nm. The contour plot illustrated in panel B is of the region bound by the white square in panel A. This figure shows that an absolute maximum inverse sum of apparent concentration CV^2 is achieved with channel 1 collecting only CFP photons emitted between 450-507nm, channel 3 collecting primarily the YFP emission as well as the CFP bleed-through emitted between 516-650nm, and the middle channel collecting photons in a relatively small channel near the intersection of the emission spectra.

Closer examination of the figure in panel B indicates that an overall optimal three channel configuration would be achieved with two channels similar to those characterized above with a relatively small channel, 10nm, collecting photons from the area of strongest spectral overlap. This figure also implies that even with the oversampling of the spectral resolution, the placement of the channels is of great importance in the efficient separation of apparent concentrations. Shifting the border of any of the channels more than 20nm significantly increases the summed CV^2 and thus decreases the SNR of the FRET indicator.

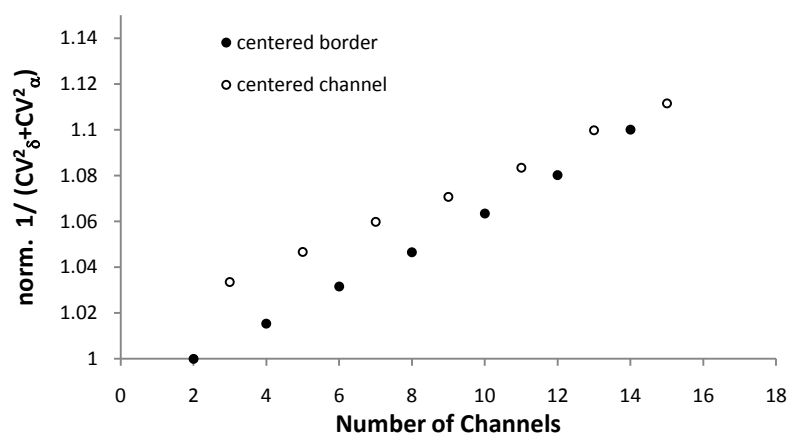


Figure 3.26 | The normalized inverse of summed CV^2 of the apparent concentrations as a function of the number of channels used to sample the fluorescence. Two channels are sufficient for the decomposition of donor and acceptor fluorescence. Increasing this quantity proportionally increases the SNR^2 of most luxFRET quantities. Further dividing the optimal two channels, shown in figure 3.24, increases the SNR^2 of the measurements (solid circles). Similarly by increasing the spectral resolution while maintaining the centered channel suggested by figure 3.25 results in the increase in SNR^2 of the luxFRET quantities indicated by the empty circles.

Overall global optimization for these simulations four or more channels was found not to be trivial. Multiple local maxima and minima prevented the accurate fitting of channel widths for minimal summed CV^2 apparent concentration. Thus the effect of increased spectral resolution was estimated in two ways. The first approach implemented, maintained the optimal two channel border and further increased the spectral resolution by subdividing the two channels into equal parts. The second method similarly increased resolution; however it maintained the optimal 'middle' channel

defined by the three channel optimization. Figure 3.26 shows the $1/\Sigma CV^2$ relative to the optimal two channel measurement. This figure clearly indicates an increase in the SNR of the FRET estimators with increased spectral resolution, with the centered border and centered channel estimates converging when more than 10 channels are used (at a spectral resolution of 20nm/channel). However, surprisingly, the increase is only approximately 1% SNR^2 per additional channel. This is relatively low compared to the decrease in SNR^2 resulting from the misplacement of the channel border in the two channel measurement.

3.10.2 Optimization of excitation wavelengths

Noise propagation through the spectral FRET analysis was also investigated through Monte Carlo simulations. Emission from a sample with a given FRET efficiency was simulated through the use of measured reference spectra and equation 1.12. Noise was added to the sample corresponding to shot noise from a given number of collected photons. These simulations allow for predictions similar to those made by the error propagation analysis. Additionally these simulations provide a method through which other predictions can be made.

One advantageous feature of the spectral analysis presented above is the ability of the method to be applied without additional corrections for or absolute criteria for excitation crosstalk. Other quantitative spectral methods require a long wavelength excitation that does not excite any donor molecules. This is not a problem for CFP-YFP. However, with other FRET pairs an appropriate excitation source may not be available. Although luxFRET allows for virtually any excitation wavelengths to be used, we have shown that the use of certain excitation wavelengths can simplify the analysis performed, generally through the assumption of negligible donor excitation with the long-wavelength excitation, allowing one to set $r^{ex,2}$ equal to 0. It is reasonable to assume that, although the analysis is possible and may yield the correct results at any pair of excitation wavelengths, that the noise may be affected. To further explore this we used the discussed simulations to predict the SNR^2 of E_{f_D} and E_{f_A} for a range of paired excitation wavelengths. To do

this, however, the ratio of extinction coefficients, which are usually determined empirically in the calibration steps of the luxFRET analysis, and for which measured values were used in the initial evaluation of the simulations, must be estimated. Reasonable estimates for these ratios can be gathered from literature, however, due to the impracticality of accurately characterizing the spectral properties of one's excitation source they should not be used in place of empirically determined values when available.

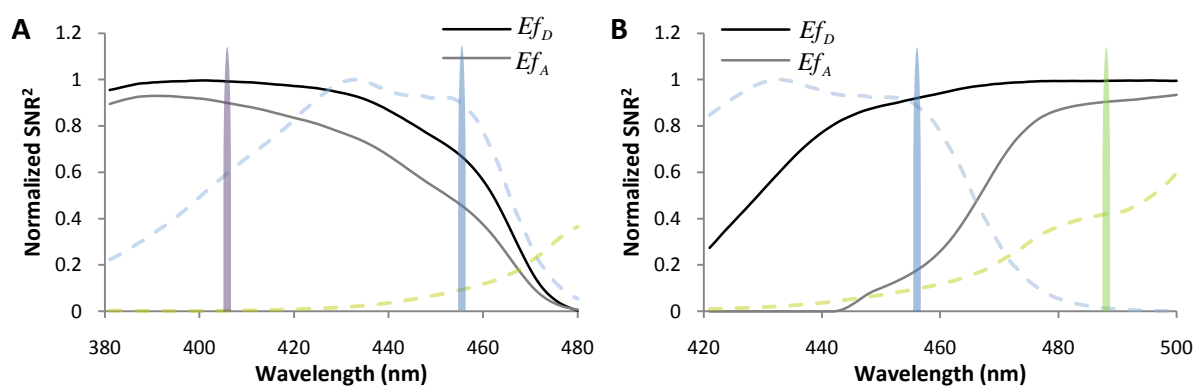


Figure 3.27 | SNR^2 of luxFRET quantities as functions excitation wavelength. A) SNR^2 of apparent FRET efficiencies as functions of short wavelength excitation position with long excitation wavelength at 488nm. B) SNR of luxFRET apparent FRET efficiencies as functions of long wavelength excitation position with short excitation wavelength at 405nm. In each panel the normalized excitation spectral for CFP and YFP are represented as blue and yellow semi-transparent dashed lines. The vertical lines represent the location of common excitation wavelengths.

Simulations were performed for varied short wavelength excitation position with the long wavelength excitation fixed at 488nm. Similar simulations were performed with the short wavelength excitation fixed at 405nm and varied long excitation wavelength position. In these simulations the total number of photons simulated was held constant. These simulations do not take into consideration the loss of emission detection as excitation wavelength impinges upon and begins to overlap the emission spectra. Of course as the excitation wavelength begins to overlap with that of the emission, collection of emission will be lost to prevent collection of scattered excitation. It is

reasonable to assume that as the excitation wavelength shown in figure 3.27 approaches the onset of CFP emission, approximately 450nm, that a steeper decrease in actual SNR^2 would occur. Of course this would not be due to the value of excitation ratio, $r^{\text{ex},1}$, but rather due to the loss in collected photons due to appropriate emission channel placement. As was shown in the error propagation analysis, the SNR^2 of Ef_D is greater than that of Ef_A . As would be expected the SNR of these two quantities vary differently with either excitation wavelength. Ef_A is determined completely from acceptor emission. Figure 3.27 panel B clearly shows that as the excitation 2 wavelength decreases and a contribution to fluorescence from CFP is measured the SNR of Ef_A rapidly decreases. This contribution to fluorescence from CFP (non-negligible δ^2) results in a decreased SNR of α^2 . As neither Ef_D nor Ef_A are functions of δ^2 , neither quantity increase in SNR with shorter wavelength excitation 2 measurements.

The results of the simulations were verified with measurements performed at three different wavelengths. 10 N1E cells expressing the CFP-YFP tandem construct were imaged at 405nm, 458nm, and 488nm. Three sets of FRET estimators were calculated with each combination of the three excitations. Figure 3.27 panel A shows the SNR^2 of the 405nm/488nm measurement as a function of the corresponding 458nm/488nm measurement. Cells with different concentrations and varied excitation intensities were used such that the total collected photons measured varied between 618 and 2,834, resulting in a spread in the data. The data was fit with a linear regression indicating that the SNR^2 of Ef_D when using 405nm as the short excitation is 1.37 fold of that when using 458nm as a short excitation wavelength. Interestingly, even though the SNR of $\alpha^{(1)}$ can be assumed to be less due to a lesser degree of direct excitation, the use of 405nm as the excitation 1 wavelength results in an even more augmented SNR^2 of Ef_a (1.74 fold). One can postulate that this is due to the greater fraction of α^1 resulting from sensitized emission, and thus containing more direct information about the FRET efficiency. Comparing these data to those predicted we see that the general relationship between the values is the same however the simulations predicted even larger increases in SNR^2 for Ef_D and Ef_A , 1.6 and 2.2 fold, respectively.

The simulations predict that the use of 458nm would result in a SNR^2 of E_{fD} of 94% that of the same measurement with excitation 2 at 488nm. The measurements are in good agreement, with the SNR^2 of E_{fD} with long wavelength excitation at 458nm being 92% that of at 488nm. The predictions for E_{fA} do not match the measurements as accurately. The simulations predict that the use of 458nm as the long wavelength excitation would decrease the SNR^2 of E_{fA} to only 23% that of the case in which 488nm is used. The measurements indicate that the decrease is much more severe, with the SNR^2 effectively equal to zero for all measurements.

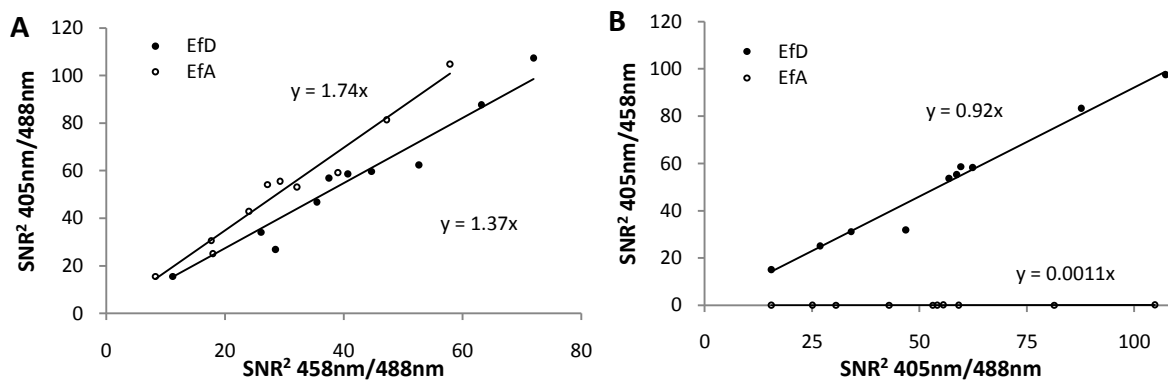


Figure 3.28 | Comparison of resulting SNR^2 of apparent FRET efficiencies with varied Ex1 and Ex2 wavelengths. A) In the case that 405nm is used as the short wavelength excitation, rather than 458nm, an increase in the SNR^2 of E_{fD} of 1.37 fold is measured. In the case of the SNR^2 of E_{fA} an increase of 1.74 is measured. B) In the case that 458nm is used as the long wavelength excitation, rather than 488nm, a decrease of 0.92 fold is expected for the SNR^2 of E_{fD} . The SNR^2 of E_{fA} for all of the the 405/458nm measurements are more or less equal to 0.

4 Discussion

4.1 Implementation and validation of a novel spectral FRET method

In the preceding a method for spectral analysis of FRET-signals was presented. The equations derived to characterize FRET take into consideration both the contributions of unpaired donor and acceptor fluorophores and the influence of incomplete labeling of the interacting partners. In this method the contributions to fluorescence from a FRET sample measured at two different excitation wavelengths are separated using linear unmixing with donor and acceptor reference spectra. The weights of these reference spectra defined during the unmixing procedure, denoted apparent concentrations, are used along with calibration constants to determine two apparent FRET efficiencies. These apparent FRET efficiencies correspond to those measured from donor quenching and acceptor sensitization-type experiments. In addition to the apparent FRET efficiencies we also determine the FRET-corrected total donor and total acceptor concentrations (as factors of the reference concentrations). These total concentrations are used to determine the FRET-corrected total acceptor to total donor ratio. Furthermore these derivations suggest that spectral analysis of intermolecular FRET cannot yield accurate values of the Förster energy transfer efficiency E , unless one of the interactors is in large excess and perfectly labeled. In the case of imperfect labeling or intermolecular FRET with free donor and acceptors spectral analysis yield the products Ef_D and Ef_A where f_D and f_A represent the fraction of donor or acceptors participating in the FRET complex, also referred to as fractional occupancies.

To verify that the values determined by the presented method were accurate, a CFP-YFP tandem construct was used as a FRET standard and luxFRET measurements were compared to those from established methods. The first method used to verify the apparent FRET efficiency determined by the luxFRET analysis was acceptor photobleaching. This method directly compares the fluorescence intensity of quenched donor in presence of acceptor with the intensity of the free donor by removing the acceptor in the same sample through photobleaching. The effect of donor

quenching due to energy transfer can thus be directly calculated. Donor quenching was also measured by quantifying the excited state lifetime of the FRET construct as well as that of the free donor through time correlated single photon counting. Unlike the intensity of fluorescence emission used in the acceptor photobleaching measurements, the excited state lifetime is concentration independent so measurements can be performed on two different samples. The apparent FRET efficiencies reported from these two methods (figure 3.3) as well as the proposed method (figure 3.2) were shown to be in good agreement.

A closer look was taken at the underlying factors which contribute to the fractions included within the apparent FRET efficiencies. It was concluded that these fractions are composed of the products $f_d p_a$ and $f_a p_d'$, with $p_{a,d}$ denoting the probability that a given donor/acceptor interactor molecule is labeled with an appropriate and functional fluorophore. The prime in p_d' serves as a reminder that this quantity also depends on the folding/labeling state of the tandem construct used in the calibration procedure (see eq. 1.36). In the case of fluorescent proteins the probabilities of correct folding have been shown to depend on temperature and other ambient factors and have been estimated to vary between 50 – 90% (Sugiyama et al. 2005; Yasuda et al. 2006). Most fluorescent proteins must also undergo a post-translational maturation before they become functional (Ogawa et al. 1995). This implies a time dependency of these probabilities. Differences in the maturation half time between donor and acceptor molecules can lead to a time dependent stoichiometry upon which a measured apparent FRET efficiency would depend.

4.2 Considerations for fluorophore bleaching and protonation

One problem that is not present in spectroscopy, as much as it is in microscopy, is photobleaching. This photo-destructive process leads to time dependent changes in p_a and p_d' . The equations derived in luxFRET suggest that each of the apparent FRET efficiencies measured is susceptible to photobleaching of one of the species. Figure 3.4 show in the case of acceptor bleaching that the quantity $E f_d p_a$ decreases over time while $E f_a p_d$ remains constant. Accordingly the total acceptor to

total donor ratio decreases over time with increased bleaching. One advantage of the proposed methods is that it allows one to quantify the total acceptor concentration of the FRET sample (relative to the reference), from which the relative change in p_a can be quantified. Using this, it is shown in figure 3.4 panel D that the estimated Ep_a can be corrected for any time dependent changes in p_a and the quantity $Ep_{a,0}$, where $p_{a,0}$ is the initial time-independent labeling probability, can be determined. This provides a basis upon which photobleaching dependent change in the apparent FRET efficiencies can be corrected.

Others have proposed methods for correcting FRET measurements for acceptor bleaching (Zal and Gascoigne 2004). Among the methods proposed, is the characterization of bleaching kinetics from reference acceptor samples as well as the use of direct excitation of the acceptor in a FRET sample to follow the decrease in concentration. This group as well as others takes into consideration sensitized bleaching and FRET dependent acceptor bleaching kinetics and make suggestions according to the type of experiment being performed (Mekler et al. 1997; Zal and Gascoigne 2004). Although direct acceptor excitation measurements will provide sufficient information for correcting Ef_D , it may be the case that direct excitation without excitation crosstalk and emission bleed-through is not possible. In such a case, the detected emission would not necessarily characterize the decrease in acceptor concentration. The calculation of the FRET corrected total acceptor concentration, as performed in the luxFRET analysis, still allows for bleaching correction with excitation crosstalk and emission bleedthrough.

Most of the GFP variants have been shown to exist in a balance between protonated and non-protonated states. In the case of YFP, protonation has been shown to alter the fluorescent properties of the chromophore such that its absorption spectrum is blue shifted with a peak near 390nm (McAnaney et al. 2005). Absorption is shifted to such an extent that there is neither overlap with the excitation wavelengths used nor with the donor emission spectrum. The protonated form of YFP can be considered to exist in a dark state in the measurements performed herein. The pKa of

the protonation reaction is near physiological pH (Miyawaki et al. 1999), further complicating the use of YFP in biological samples. This dependence has been shown to influence FRET measurements such that quantitative calibrations may vary greatly between samples (Salonikidis et al. 2008). Figure 3.5 shows, similarly to the acceptor photobleaching experiments, that the quantity $E_{f_a p_d}$ is nearly independent of the pH dependent changes in YFP fluorescence, while $E_{f_d p_a}$ and R^t are affected. At lower pH the fluorescence of CFP is influenced (Llopis et al. 1998) and would affect this $E_{f_a p_d}$ and R^t , however this occurs at an extreme for physiological pH so it is generally negligible in biological samples. Although the pH dependence of GFP and its variants have found some use (Heim and Tsien 1996; Miesenbock et al. 1998; Abad et al. 2004; Esposito et al. 2008), in most FRET measurements this dependence is unwanted and can prevent quantitative measurements. However, with a dependent and independent quantity defined by luxFRET, not only is it possible to monitor the FRET state of the system, but ambient factors to which one fluorophore is sensitive can be monitored simultaneously.

4.3 Identification of intermolecular interaction

In the measurements performed thus far, only a CFP-YFP tandem construct has been used as a FRET standard. Not only can the presented method also be applied to intermolecular FRET systems, but the additional quantities it characterizes are pertinent to quantitatively assessing the level of interaction between two species of molecules. The apparent FRET efficiencies that this and other steady state methods quantify, are composed of the characteristic efficiency of energy transfer as well as fractional occupancy of donor with acceptor, f_D , or that of acceptor with donor, f_A . These fractional occupancies are in turn dependent on the relative abundances of donor and acceptor present in the sample. Thus simultaneous characterization of both the apparent FRET efficiency as well as some measure of the relative amounts of donor and acceptor (ratio or fraction) are necessary to appropriately address questions regarding degrees of interaction.

To illustrate the application of this method to the identification of intermolecular interaction, measurements were performed on three sets of receptors. CD-86 and CD-28 were used as monomeric and dimeric membrane receptor controls, respectively (James et al. 2006; Dorsch et al. 2009). The 5HT_{1A} receptor was the sample for which interaction was being investigated. Biochemical assays as well as some FRET measurements have suggest that this receptor forms homo-oligomers in the plasma membrane (Kobe et al. 2008; Woehler et al. 2009). To compare measurements between these samples, the apparent FRET efficiencies were plotted as functions of the corresponding donor fraction measured in each sample in figure 3.6. As the fractional occupancy terms contained within the apparent FRET efficiencies are dependent on the relative abundance of acceptors and donors, comparison of efficiencies at the same expression ratio (or fraction) is essential.

The apparent FRET efficiency measured from the samples expressing the monomeric control, CD86, suggest a significant amount of stochastic interaction. This stochastic interaction is dependent on the total concentrations. Assuming that the total concentration of CFP and YFP tagged receptors is equivalent in all samples, the apparent FRET efficiencies measured from 5HT_{1A}-CFP and 5HT_{1A}-YFP suggest that the degree of interaction does surpass that of the expected stochastic interaction. These measurements also provide evidence that high affinity constitutive dimerization of 5HT_{1A} is unlikely. The increase in apparent FRET efficiency above the level measured for stochastic interaction for the covalently dimerized CD28 is more than double that of the 5HT_{1A} receptor. It is possible that the higher apparent FRET measured between the CD28 tagged constructs could be due to a higher characteristic FRET efficiency from the adoption of a more FRET-favorable conformation. This could arise from a closer interaction radius or a more favorable orientation of the fluorescent proteins. With no reason to believe that these factors are not equivalent between the CD28 and 5HT_{1A} constructs, it can be concluded there is some self association between 5HT_{1A} receptors, however with a substantial portion existing in a monomeric configuration.

One complication in the interpretation of intermolecular FRET measurements arises from non-specific or stochastic interaction of molecules in a crowded environment such as the plasma membrane. The apparent FRET efficiency measured from the samples expressing the monomeric control, CD86, suggested the presence of a significant amount of stochastic interaction of membrane localized proteins at the expression levels reached from transient transfection. Relatively early in the application of FRET investigations to biological samples it had been shown that FRET can occur due to stochastic interaction in crowded environments (Wolber and Hudson 1979). It was also shown that localization in membrane microdomains can increase the effective density of the proteins being investigated (Kenworthy and Edidin 1998; Varma and Mayor 1998; Zacharias et al. 2002). In some cases this stochastic interaction has been shown to result in measured apparent FRET efficiencies similar to measurements from which oligomerization has been interpreted (Herrick-Davis et al. 2006; Meyer et al. 2006). Care should be given when investigating FRET though the over expression of proteins in the plasma membrane and ideally negative and positive controls as similar to the protein of interests, i.e. with same number of transmembrane domains and posttranslational modifications, should be used when available. This has been a challenge in the characterization of GPCR oligomerization as many oligomerization positive receptors have been proposed (Terrillon and Bouvier 2004) but no clear negative controls have emerged (James et al. 2006).

Not only do many investigations seek to identify interaction surpassing the expected stochastic interaction, but they aim at characterizing the stoichiometry of interacting donor and acceptor molecules. Models exist which propose to estimate the order of interaction (Veatch and Stryer 1977) from FRET measurements of homo-oligomers. These models predict a linear relationship between the donor fraction and the apparent FRET efficiencies for dimeric interaction. At concentrations in which stochastic interaction begins to yield a measurable FRET efficiency, the interaction that will first occur is between one donor and one acceptor. As the concentration is increased it can be assumed that the stoichiometry of this interaction will change. Never the less, low FRET efficiency stochastic interaction will be fit by these models as a dimeric reaction with a low

characteristic FRET efficiency. Furthermore this model (Veatch and Stryer 1977) was based on the assumption that energy transfer from a donor molecule was independent of the number of acceptors present. This assumption has, on many occasions, been shown to be incorrect (Fung and Stryer 1978; Wolber and Hudson 1979; Thaler et al. 2005). Ultimately, this model does not afford the user the ability to distinguish between stochastic interaction and dimerization, nor does it allow for the characterization of interaction surpassing dimerization. The Veatch/Stryer model does allow for the identification higher order oligomers, however this can be determined qualitatively through identification of nonlinearity in the relationship between apparent FRET efficiency and donor or acceptor fraction.

4.4 Application to microscopy and consideration for noise propagation

While it has been shown that this method can be applied successfully to measurements performed on a spectrofluorometer, its transfer to microscopy has many advantages. Microscopy allows for both spatial and temporal dynamics to be investigated with greater resolution. This in turn opens the door to a broader set of investigations to which this method can be applied. Figure 3.7 illustrates how the experimental framework applied to spectroscopy above is applied to spectral imaging. With the Zeiss LSM 510 Meta, emission can be collected over eight channels allowing for spectral reconstruction with up to 10.7nm resolution. We show that this is sufficient for the efficient separation of CFP and YFP emission and that by performing measurements at two wavelengths the previously discussed luxFRET quantities can be computed on a per pixel basis at confocal resolution. As in the evaluation of the method on the spectrofluorometer, the CFP-YFP tandem construct FRET reference verifies that this method provides values that are in line with the previous measurements.

Not all differences between the approaches favor microscopy. The signal to noise ratio of a spectral acquisition from the spectrofluorometer, as used in the experiments presented, can easily be on the order of $10^2 - 10^3$ (Jacobs 1978; Froehlich 1989). The SNR of confocal images is typically an order of magnitude less (Pawley 2006). Furthermore, when performing nonlinear computation of

measured quantities with inherent noise, such as FRET analysis requires, small changes in the level of uncertainty of a variable can have large effect on the level of uncertainty of the defined function. For this reason the propagation of photon and detection noise through the equations often used to analyze fluorescence collected from FRET samples was investigated. Specifically, different luxFRET analysis modes as well as the 550/485nm emission ratio often used for ratiometric methods with CFP and YFP (Grynkiewicz et al. 1985; Miyawaki et al. 1999) were considered. In the theoretical considerations it was pointed out that for a tandem construct, FRET estimators can be calculated from any ratio of the three apparent fluorophore concentrations of a lux-FRET measurement (eqs. 1.39 – 1.40). Figure 3.14 presents images of the quantities resulting from these analysis modes. Figure 3.15 shows the SNR measured from these images. The best performing luxFRET analysis mode was found to be the mode based on the emission ratio after donor excitation (Eq.1.39 $i=1$), which is quite similar to the standard emission ratio method. Surprisingly the analysis mode, which is based on the two best resolved signals, $\delta^{(1)}$ and $\alpha^{(2)}$, performed relatively poorly, assumedly due to very unfavorable error propagation and lower FRET information content.

In order to execute these measurements in a manner in which cross platform inferences could be drawn, the setup was calibrated such that the amount of collected emission was determined in numbers of photon rather than in arbitrary detector units. This was performed by determining the apparent single photon signal from the relationship between the mean and variance of the fluorescence signal (Neher and Neher 2004; Dalal et al. 2008). This was performed for multiple detector gains such that a gain with an appropriate photon detection dynamic range could be selected. The results presented in figures 3.10 - 3.11 show that with the acquisition settings used in the presented measurements allowed as many as 500 photons to be detected per emission channel before saturation.

Models relating the signal-to-noise ratio of FRET estimator to the number of photons collected were presented in eqs. 1.46 and 1.49. The dependence of the relatively high SNR two

excitation dependent luxFRET quantity, Ep_o calculated from eq. 1.38 on the number of photons collected in each respective acquisition was characterized. The preliminary, and fairly intuitive, conclusion regarding SNR optimization had been that one should maximize the number of photons collected from the two measurements within the limits of bleaching. A close look at figure 3.16 indicates that aiming at equal numbers of collected photons during the two excitations does not provide for optimal SNR^2 of Ep_o . The majority of the photons collected in the long-wavelength acquisition are emitted from the acceptor, such that the information contained within the signal is minimally degraded by spectral overlap. During the short-wavelength excitation, however, both donor and acceptor molecules significantly contribute to emission and the spectral unmixing of their contributions leads to a loss of information. This suggests that an optimum SNR^2 for Ep_o would be achieved by favoring the detection of photons in the first acquisition at the expense of photon detection during the second acquisition. In figure 3.16, it is demonstrate that at the optimum SNR^2 of Ep_o , approximately 63% of the total photons would be collected during the first acquisition. The SNR^2 of Ep_o corresponding to the measurement illustrated in figure 3.14, panel D, is approximately 44 and was achieved with only 45% of the total photons being collected during the short wavelength excitation. This figure suggests that a SNR^2 of $Ep_o = 49$ could be achieved by altering excitation intensities such that the measurement is moved to the maximum of the contour.

When comparing the investigated luxFRET and ratiometric quantities, two analysis modes were identified which are especially well suited for measuring dynamic changes in FRET efficiency: The 550/485nm emission ratio and the luxFRET quantity, Ep_o derived from Eq. 1.39 with $i=1$. These two methods had the highest SNR^2 (figure 3.15) and they can be performed with a single excitation. Through the error propagation analysis, it was shown that the SNR^2 of ratiometric measurements exceeds that of the luxFRET quantities for the expected FRET efficiencies of most FRET sensors. Interestingly, our analysis suggests that above approximately $E = 0.38$, the SNR^2 of Ep_o will begin to exceed that of the 550/485nm ratio. Time series of measurements of a cerulean-EPAC-citrine FRET sensor were performed during which an increase in intracellular cAMP concentration was induced

through the activation of adenylyl cyclase with the membrane permeable agonist forskolin. Both analysis modes similarly reported the relative change in the ratio of free and bound sensors. In figure 3.18 the SNR^2 of Ep_a measured during this experiment is plotted as a function of the number of detected photons and the measured apparent FRET efficiency. A surface predicted by the error propagation model is also illustrated. Comparison of the measured and predicted values indicates that the model performs quite well when predicting changes in SNR^2 due to changes in FRET efficiency and with the decrease in the number of detected photons.

The ultimate utility of the measurements of Ep_a or the 550/485nm emission ratio from a FRET sensor is to provide an estimation of the absolute ligand concentration in the FRET sample. This conversion can be readily performed with the appropriate calibration information. However, it further amplifies error. An unexpected finding of this investigation was that, although the SNR^2 550/485nm exceeds that of the SNR^2 of Ep_a , these two quantities perform similarly when estimating the absolute ligand concentration. The mean ligand concentration of a region of interest was calculated in two ways: (1) the mean Ep_a or 550/485nm emission ratio from a ROI was measured and converted to $[cAMP]^*$, and (2) conversion from Ep_a or the 550/485nm emission ratio to $[cAMP]^*$ was performed on a per pixel basis and the mean $[cAMP]^*$ of the ROI was computed. Figures 3.19 panel A compares these results of these approaches. The figure shows that the estimates based on the per pixel conversion begin to fluctuate greatly over time as $[cAMP]$ increases while the other estimate stably increases and plateaus. Figures 3.19 panel B shows that the SNR^2 of the per pixel approaches increase as E diverges from the E_{free} value and decreases as E converges upon the E_{bound} value from eq. 1.51. Panel C of figure 3.19 illustrates, similarly to figure 3.18, that the error propagation analysis model performs well in predicting the SNR of $[cAMP]^*$ for a given FRET efficiency and number of collected photons.

When comparing the results of the two approaches a bias was noticed. Figures 3.20 and 3.21 illustrate that this bias is due to the skewing of the data that occurs during the conversion. This

skewing becomes most prominent as the sensor approaches its fully bound state. This would suggest that, while it is possible to determine ligand concentration on a per pixel basis from FRET data, it should be performed with caution and care should be taken to ensure that the relative fluctuations in the FRET signal and the nonlinearity of the conversion are not dominating the estimated ligand concentration.

The SNR^2 of the ligand concentration determined by these two methods, presented in figure 3.19 panel B, was found to be essentially equal. This is interesting, considering the SNR of the emission ratio was twice that of E_{p_a} , as shown in figure 3.15. This suggests that either the error propagation when converting E_{p_a} to $[\text{cAMP}]^*$ is favored over that of the emission ratio or that the SNR of these parameters insufficiently characterizes their ability to resolve changes in FRET over noise and are they not directly comparable. The equations used to convert E_{p_a} and the emission ratio to $[\text{cAMP}]$ are analogous and propagate error accordingly, so there should not be any favor of one over the other. Furthermore comparing the E_{p_a} and 550/485nm images in figure 3.14 the images appear to have similar levels of noise, with the color bars proportionally scaled. In the case of the 550/485nm emission ratio, at $E = 0$, a signal of approximately 0.8 is measured. When quantities have different offsets what becomes important is not the amount of noise relative to the basal level or even absolute value, but the amount of noise relative to the response to a change in FRET.

An offset invariant quantity characterizing the relative change in a parameter can be calculated by dividing the difference from the parameters mean initial value by this mean initial value. This calculation was performed on a per pixel for the 550/485nm emission ratio, the apparent concentration ratio, and E_{p_a} in the example of the change in $[\text{cAMP}]^*$ shown above. A mean of these quantities was sampled from the same ROI used in the previous examples. Figure 3.22 shows that, as would be expected, the mean relative change in E_{p_a} is the greatest. The change in the apparent concentration ratio is greater than in the emission ratio because it is bleed-through corrected representation of the acceptor to donor ratio. The acceptor component of the emission

ratio, 550nm, still contains significant fluorescence from CFP. The variances of these quantities were also computed and are shown in figure 3.22 panel B to be relatively time invariant. As would be expected the noise in the calibrated measurement, Ep_a , is the greatest. Surprisingly, although it is computed with less photons the 550/485 nm ratio has a lower variance than the ratio of the apparent concentrations. The real 'figure of merit' of these quantities is the SNR indicated in figure 3.23.

Overall, however, the SNR^2 of both estimates of ligand concentration are much lower than those of the raw FRET signals. It should also be noted that ratiometric measurements are generally instrument-dependent and that the calibration required for absolute ligand concentration measurements may not be trivial to perform on all instruments. Quantitative measurements of FRET efficiency, however, are not instrument-dependent. As these two analysis mode perform similarly in estimating the absolute ligand concentration, the use of Ep_a is advantageous, when cross platform calibration is required.

4.5 Optimization of spectral resolution and excitation wavelength

Several of the error propagations equations, introduced and validated above, characterize the CV^2 of the FRET estimators as directly proportional to the sum of the CV^2 of the apparent concentrations used in their computation. Figure 3.12 suggest that equations 1.43 – 1.45 can be used to provide a rough estimate for the CV^2 of the apparent concentrations with only a single set of reference and sample spectra. With the use of highly resolved reference and sample spectra the effect of binning fluorescence into channels on the SNR of the FRET quantities was investigated. Spectrally resolved emission spectra spanning 450 nm to 650nm (encompassing the complete CFP and YFP emission) were first binned into two channels. The border between these two channels was varied between over the entire emission range, the fluorescence was binned and the CV^2 of the apparent concentrations was computed from equation 1.43 – 1.45. The inverse of the sum of the CV^2 values was used in figure 3.24 because plotting the sum of the CV^2 values resulted in a relatively broad

trough, from which a global minimum was not visually apparent. Also the inverse of the sum of the squared CV^2 is directly proportional to the SNR^2 of many of the luxFRET quantities. Figure 3.24 shows that the optimal location for the border between two emission channels from which contributions from CFP and YFP are to be determined exists around 509nm. Of course, this will vary with FRET efficiency and the relative abundances of CFP and YFP. This may seem quite intuitive and the same conclusion can be drawn from a visual inspection of the spectra, however, it verifies a method that can be applied to the optimization of the placement of more channels.

Similar simulations were performed with three channels bound by the same spectral range. Figure 3.25 illustrates the normalized inverse sum of the CV^2 of the donor and acceptor apparent concentrations as a function of the first (short wavelength) and middle channel widths. The width of the third channel can be computed considering the fixed spectral range. This figure indicates that even with more channels than are sufficient for the separation of donor and acceptor contributions that channel placement remains important, although to a lesser degree. In general, a maximum in the inverse sum of the CV^2 's is obtained when either the channel 1-2 border or the channel 2-3 border is located near 509 nm. This figure also suggests that overall optimized separation of CFP and YFP with three channels is achieved with the use of a relatively small (10nm) center channel. Within this region the peak is relatively broad. Accordingly, it would be reasonable to assume that the quality of CFP and YFP separation would be less sensitive to changes in the spectral overlap resulting from changes in FRET or the relative abundances. Similar simulations were performed for 4 and more channels, however, global optimization of these simulations was not possible, as there were many local maxima and minima. Figure 3.26 illustrates two ways in which greater spectral resolution was explored. This figure shows that increasing spectral resolution while maintaining a border or smaller channel centered at 510nm does result in an increase in the SNR of the luxFRET quantities. However, this increase is relatively small, at only about 1% per additional channel.

It is noteworthy that the increase in SNR resulting from increasing the spectral resolution is small relative to the decrease resulting from misplacement of the channel borders. This has been previously reported in the general case of separation of fluorescent species using linear unmixing (Neher and Neher 2004). Although these results may suggest that spectral resolution is less important it should be kept in mind that in a system where the relative abundances of fluorophores changes or there are large changes in FRET the optimal borders are not static. The advantage of using higher spectral resolution, 8 channels in our case, is that the probability of a border residing near the optimal location is significantly increased.

These results would seem to suggest that the conclusions reached regarding the SNR of FRET estimators with respect to the measured FRET efficiency and number of photons collected is not restricted to the setup upon which the presented measurements were performed. This new data would suggest that the same relationships relating the SNR to the number of collected photons would be maintained with only a small decrease in the SNR with decreases spectral resolution. In the case of 3-cube methods, the decrease SNR from the reduced spectral resolution would almost certainly be compensated for by the higher quantum efficiency of emCCD, which in these approaches are often used (Zal and Gascoigne 2004). Of course this transition from confocal to widefield would also come at a loss of axial resolution.

One advantage of luxFRET over the other spectral methods discussed is that corrections for excitation crosstalk are inherent in the method. The only requirement of this method is that the short wavelength must provide direct donor excitation and the long wavelength excitation must directly excite acceptor molecules. The absolute values of the luxFRET quantities should be independent of excitation crosstalk. However, the same cannot be said about the SNR of the quantities. Other methods require at least selective direct excitation of the acceptor, and provide some corrections for short wavelength acceptor excitation. This is not a problem with CFP and YFP,

as both 488nm and 514nm laser lines are sufficient for long wavelength selective YFP excitation. However, such appropriate excitation may not be available for other possible FRET pairs.

Optimization of excitation wavelength has been performed in the past based on the requirement of former methods requirements of selective direct excitation (Karpova et al. 2003; van Rheenen et al. 2004). However, with regards to luxFRET it may be the case that optimal excitation is found at different wavelengths. For example, it could be the case that some direct acceptor excitation provided by the short wavelength excitation would result in a more resolved acceptor apparent concentration, $\alpha^{(1)}$, and thus reduce the noise propagated to the luxFRET quantities. Because a variable wavelength excitation source was not readily available on the setup used in these measurements, simulations were performed. In these simulations fluorescence emission from equal amounts of donor and acceptor molecules were estimated from normalized measured emission and excitation spectra and extinction coefficients and quantum efficiencies from literature. The excitation ratios $r^{ex,i}$ for a given pair of excitation locations were determined from the literature extinction coefficient values and the spectra were combined considering energy transfer with an efficiency of 25%. These spectra were then sampled similarly to the channels of the setup used in the previously discussed FRET measurements. An appropriate amount of noise was added to account for photon detection noise. This procedure was repeated multiple times to build statistics and estimate the SNR of the Ef_D for a given pair of excitation wavelengths. Figure 3.27 illustrates the results of these simulations. Similarly to the conclusions of previous investigations (Karpova et al. 2003; van Rheenen et al. 2004) the SNR of the Ef_D does increase as the short excitation wavelength is decreased and thus the amount of direct acceptor excitation decreases. Van Rheenen et al. suggest that the SNR (or 'resolving power') should decrease below 430nm due to the decrease in CFP absorption. With a fixed excitation intensity this would be the case, however for a fixed amount of emission, as the proposed simulations consider, there is no coordinate decrease in SNR of Ef_D with the CFP excitation spectra.

The results of the simulation were confirmed through measurements of the CFP-YFP FRET standard performed with three excitation wavelengths (405nm, 458nm, and 488nm). E_{f_D} and E_{f_A} were calculated using the three different excitation pairs. The total number of photons collected from each cell varied, so a linear fit to paired measurements is used to estimate the relative performance of one excitation pair against another. These relative performances were also determined from figure 3.27. Although the absolute value of the relative increase or decrease in SNR between the excitation pairs do not exactly match the general trend is confirmed. The use of literature values for the determination of the excitation ratios, $r^{ex,i}$, possibly contributes to the discrepancy in these values. Regardless, these data suggest that the 405nm/488nm excitation pair provide a better SNR in E_{f_D} and E_{f_A} than either of the other two pairs explored. Figure 3.27 suggest that further shifting short excitation towards the blue and the long excitation towards the red may slightly increase the SNR of E_{f_A} , however both of these excitation wavelengths are near the optimal placement in relatively broad peaks.

5 Summary

In the preceding, a novel method for characterizing FRET was presented. This method measures the apparent FRET efficiency and stoichiometry of donor and acceptor molecules present in a sample. These quantities were derived from equations which describe all the factors which contribute to the emission spectra of a fluorescent sample. Using this approach, fluorescence from a system composed of both free and interacting donor and acceptor molecules was considered. By using reference spectra to decompose this signal into contributions from donor and acceptor molecules, many constants and spectral components, which are difficult to characterize, cancel out. This method provides a general solution for donor quenching and acceptor sensitization related apparent FRET efficiencies and FRET corrected total concentration of donor and acceptor molecules (as factors of the reference concentrations). The only two requirements are that: (1) two measurements are taken, each with excitation that directly excited donor and acceptor molecules, respectively and (2) emission from donor and acceptor must be collected in at least two channels. No further corrections for excitation crosstalk and/or emission bleed-through need to be taken as these are accounted for in the analysis.

This method was first implemented using spectrofluorometry, where it was shown to provide accurate estimates for the apparent FRET efficiency. The results of this method were compared to two established methods, acceptor photobleaching and analysis of donor excited state lifetime through time correlated single photon counting, and were found to be in good agreement. From the derivation of the equations it is known that the apparent FRET efficiencies we measure are the product of the characteristic FRET efficiency of the FRET complex multiplied by the fractional occupancy of donor or acceptor with the corresponding FRET partner. Through partial bleaching of acceptor molecules it was demonstrated that there is a coordinated decrease in E_{f_D} and the total acceptor to total donor ratio, while E_{f_A} remains constant. This is consistent with the definitions of the derived quantities. It is also shown, that similarly to the effect of bleaching, that the protonation

of YFP can be observed in the value of E_{f_D} and R^t while E_{f_A} remains insensitive. Whereas ambient sensitivities of fluorophores have been considered as impediments to quantitative FRET measurements, this data suggests that quantitative measurement of apparent FRET as well as the ambient factor can be measured simultaneously.

Next it was demonstrated that this method is applicable to microscopy. Several popular microscope configurations were considered with regards to the ability to alternate between excitation wavelengths and measure emission over multiple channels simultaneously. Different analysis modes were derived such that quantitative measurements can be performed on setups with ranging configurations. In microscopy, generally less photons are collected than in spectrofluorometry, thus the SNR of the measurements was also be considered. The propagation of photon shot noise through the computation required by this method was investigated. Through Gaussian Error Propagation analysis of the luxFRET equations, models were developed to predict the SNR of the various analysis modes based of the number of collected photon during each excitation and the FRET efficiency.

One of the analysis modes proposed only requires the use of a single excitation wavelength and is thus more suitable than the others for measuring dynamic changes in FRET efficiency. With the use of a cerulean-citrine based [cAMP] sensor it was shown that the model developed for this analysis mode accurately predict the changes in SNR of the FRET measurement resulting from changes in the number of collected photons as well as changes in FRET efficiency. Quantitative comparison of the SNR of the different analysis modes was performed. It was concluded that the most commonly used FRET estimator, the acceptor to donor emission ratio, provides the best apparent SNR. However when noise is compared to the dynamic range of the FRET estimator, the emission ratio and the apparent FRET efficiency perform equally well.

Additional optimization was also performed. The placement and spectral resolution of emission channels was investigated. The rather intuitive conclusion that channel placement greatly

affects the quality with which donor and acceptor fluorescence is separate was demonstrated. Unexpectedly, however, it was also shown that once optimal channel placement has been performed, increasing spectral resolution results in only small increases in the ability to effectively separate fluorescence. This suggests that this method is applicable, with little loss in SNR, to a broader assortment of platforms than the spectrofluorometer and the relatively high spectral resolution microscope to which it was originally applied.

This work demonstrated that the proposed FRET analysis method, luxFRET, is quantitative, efficient, and broadly applicable. It is quantitative in calculated quantities are clearly defined and directly assay the physical properties of interest (FRET and fractional occupancy). This approach provides sufficient information about a FRET system to appropriately compare intermolecular measurements, and correct for photobleaching and individual fluorophore ambient sensitivities. This method provides efficient use of photons when resolving changes in FRET over noise. It performs nearly as well as ratiometric measurements, with only a slight degradation from error propagation. Finally, it was demonstrated that this method does not require high spectral resolution or highly specific excitation wavelengths and as such is applicable to a variety of imaging platforms.

6 References

- Abad, M. F., G. Di Benedetto, et al. 2004. Mitochondrial pH monitored by a new engineered green fluorescent protein mutant. *J Biol Chem* 279(12): 11521-11529.
- Becker, W., A. Bergmann, et al. 2004. Fluorescence lifetime imaging by time-correlated single-photon counting. *Microsc Res Tech* 63(1): 58-66.
- Boehning, D., R. L. Patterson, et al. 2003. Cytochrome c binds to inositol (1,4,5) trisphosphate receptors, amplifying calcium-dependent apoptosis. *Nat Cell Biol* 5(12): 1051-1061.
- Bouvier, M., N. Heveker, et al. 2007. BRET analysis of GPCR oligomerization: newer does not mean better. *Nat Methods* 4(1): 3-4; author reply 4.
- Cario, G. and J. Franck. 1922. Über Zerlegung von Wasserstoffmolekülen durch angeregte Quecksilberatome. *Zeitschrift für Physik A Hadrons and Nuclei* 11(1): 161-166.
- Chen, H., H. L. Puhl, 3rd, et al. 2006. Measurement of FRET efficiency and ratio of donor to acceptor concentration in living cells. *Biophys J* 91(5): L39-41.
- Clegg, R. 2006. The History of Fret. *Reviews in Fluorescence*. C. Geddes and J. Lakowicz. New York, Springer: 1-45.
- Clegg, R. M. 1996. *Fluorescence resonance energy transfer (FRET) in Imaging Spectroscopy and Microscopy*. New York, John Wiley & Sons.
- Dalal, R. B., M. A. Digman, et al. 2008. Determination of particle number and brightness using a laser scanning confocal microscope operating in the analog mode. *Microsc Res Tech* 71(1): 69-81.
- Dale, R. E., J. Eisinger, et al. 1979. The orientational freedom of molecular probes. The orientation factor in intramolecular energy transfer. 26(2): 161-193.
- Dorsch, S., K. N. Klotz, et al. 2009. Analysis of receptor oligomerization by FRAP microscopy. *Nat Methods* 6(3): 225-230.
- Eisinger, J. and R. E. Dale. 1974. Interpretation of intramolecular energy transfer experiments. *Journal of Molecular Biology* 84(4): 643-647.
- Erickson, M. G., B. A. Alseikhan, et al. 2001. Preassociation of calmodulin with voltage-gated Ca(2+) channels revealed by FRET in single living cells. *Neuron* 31(6): 973-985.
- Esposito, A., M. Gralle, et al. 2008. pHlameleons: a family of FRET-based protein sensors for quantitative pH imaging. *Biochemistry* 47(49): 13115-13126.
- Förster, T. 1946. Energiewanderung und Fluoreszenz. *Naturwissenschaften*(6): 166-175.
- Förster, T. 1948. Zwischenmolekulare Energiewanderung und Fluoreszenz. *Annalen der Physik* 437(1-2): 55-75.

Förster, T. 1993. *Intermolecular energy migration and fluorescence In.*: New York, American Institute of Physics.

Froehlich, P. 1989. Understanding the sensitivity specification of spectrofluorometers. *International Laboratory* 19: 42-45.

Fung, B. K. and L. Stryer. 1978. Surface density determination in membranes by fluorescence energy transfer. *Biochemistry* 17(24): 5241-5248.

Gadella, T. W., Jr. and T. M. Jovin. 1995. Oligomerization of epidermal growth factor receptors on A431 cells studied by time-resolved fluorescence imaging microscopy. A stereochemical model for tyrosine kinase receptor activation. *J Cell Biol* 129(6): 1543-1558.

Gaviola, E. and P. Pringsheim. 1924. Über den Einfluss der Konzentration auf die Polarisation der Fluoreszenz von Farbstofflösungen. *Z. Physik* 24: 24-36.

Gerritsen, H. C., M. A. Asselbergs, et al. 2002. Fluorescence lifetime imaging in scanning microscopes: acquisition speed, photon economy and lifetime resolution. *J Microsc* 206(Pt 3): 218-224.

Giordano, L., T. M. Jovin, et al. 2002. Diheteroarylethenes as thermally stable photoswitchable acceptors in photochromic fluorescence resonance energy transfer (pcFRET). *J Am Chem Soc* 124(25): 7481-7489.

Graham, D. L., P. N. Lowe, et al. 2001. A method to measure the interaction of Rac/Cdc42 with their binding partners using fluorescence resonance energy transfer between mutants of green fluorescent protein. *Anal Biochem* 296(2): 208-217.

Greene, J. L., G. M. Leytze, et al. 1996. Covalent dimerization of CD28/CTLA-4 and oligomerization of CD80/CD86 regulate T cell costimulatory interactions. *J Biol Chem* 271(43): 26762-26771.

Griesbeck, O., G. S. Baird, et al. 2001. Reducing the environmental sensitivity of yellow fluorescent protein. Mechanism and applications. *J Biol Chem* 276(31): 29188-29194.

Griffin, B. A., S. R. Adams, et al. 1998. Specific covalent labeling of recombinant protein molecules inside live cells. *Science* 281(5374): 269-272.

Grynkiewicz, G., M. Poenie, et al. 1985. A new generation of Ca²⁺ indicators with greatly improved fluorescence properties. *J Biol Chem* 260(6): 3440-3450.

Gu, Y., W. L. Di, et al. 2004. Quantitative fluorescence resonance energy transfer (FRET) measurement with acceptor photobleaching and spectral unmixing. *J Microsc* 215(Pt 2): 162-173.

Hailey, D. W., T. N. Dams, et al. 2002. Fluorescence resonance energy transfer using color variants of green fluorescent protein. *Methods in Enzymology*. G. Christine and R. F. Gerald, Academic Press. Volume 351: 34-49.

Heim, R. and R. Y. Tsien. 1996. Engineering green fluorescent protein for improved brightness, longer wavelengths and fluorescence resonance energy transfer. *Curr Biol* 6(2): 178-182.

Herrick-Davis, K., B. A. Weaver, et al. 2006. Serotonin 5-HT_{2C} receptor homodimer biogenesis in the endoplasmic reticulum: real-time visualization with confocal fluorescence resonance energy transfer. *J Biol Chem* 281(37): 27109-27116.

Hoppe, A., K. Christensen, et al. 2002. Fluorescence resonance energy transfer-based stoichiometry in living cells. *Biophysical Journal* 83(6): 3652-3664.

Jacobs, S. F. 1978. *Handbook of Optics*. New York McGraw-Hill Book Co.

James, J. R., M. I. Oliveira, et al. 2006. A rigorous experimental framework for detecting protein oligomerization using bioluminescence resonance energy transfer. *Nat Methods* 3(12): 1001-1006.

Kallmann, H. and F. London. 1928. Über quantenmechanische Energieübertragungen zwischen atomaren System. *Z. Physik. Chem.* B2: 207-243.

Karpova, T. S., C. T. Baumann, et al. 2003. Fluorescence resonance energy transfer from cyan to yellow fluorescent protein detected by acceptor photobleaching using confocal microscopy and a single laser. *J Microsc* 209(Pt 1): 56-70.

Kenworthy, A. K. 2001. Imaging protein-protein interactions using fluorescence resonance energy transfer microscopy. *Methods* 24(3): 289-296.

Kenworthy, A. K. and M. Edidin. 1998. Distribution of a glycosylphosphatidylinositol-anchored protein at the apical surface of MDCK cells examined at a resolution of <100 Å using imaging fluorescence resonance energy transfer. *J Cell Biol* 142(1): 69-84.

Kobe, F., U. Renner, et al. 2008. Stimulation- and palmitoylation-dependent changes in oligomeric conformation of serotonin 5-HT_{1A} receptors. *Biochim Biophys Acta* 1783(8): 1503-1516.

Lakowicz, J. R. 2006. *Principles of Fluorescence Spectroscopy*, Springer, New York.

Lazar-Molnar, E., S. C. Almo, et al. 2006. The interchain disulfide linkage is not a prerequisite but enhances CD28 costimulatory function. *Cell Immunol* 244(2): 125-129.

Lippincott-Schwartz, J., E. Snapp, et al. 2001. Studying protein dynamics in living cells. *Nature Reviews Molecular Cell Biology* 2(6): 444-456.

Llopis, J., J. M. McCaffery, et al. 1998. Measurement of cytosolic, mitochondrial, and Golgi pH in single living cells with green fluorescent proteins. *Proceedings of the National Academy of Sciences of the United States of America* 95(12): 6803-6808.

Llopis, J., S. Westin, et al. 2000. Ligand-dependent interactions of coactivators steroid receptor coactivator-1 and peroxisome proliferator-activated receptor binding protein with nuclear hormone receptors can be imaged in live cells and are required for transcription. *Proceedings of the National Academy of Sciences of the United States of America* 97(8): 4363-4368.

McAnaney, T. B., W. Zeng, et al. 2005. Protonation, photobleaching, and photoactivation of yellow fluorescent protein (YFP 10C): a unifying mechanism. *Biochemistry* 44(14): 5510-5524.

Mekler, V. M., A. Z. Averbakh, et al. 1997. Fluorescence energy transfer-sensitized photobleaching of a fluorescent label as a tool to study donor-acceptor distance distributions and dynamics in protein

assemblies: studies of a complex of biotinylated IgM with streptavidin and aggregates of concanavalin A. *J Photochem Photobiol B* 40(3): 278-287.

Meyer, B. H., K. L. Martinez, et al. 2006. Covalent labeling of cell-surface proteins for in-vivo FRET studies. *FEBS Lett* 580(6): 1654-1658.

Meyer, B. H., J. M. Segura, et al. 2006. FRET imaging reveals that functional neurokinin-1 receptors are monomeric and reside in membrane microdomains of live cells. *Proc Natl Acad Sci U S A* 103(7): 2138-2143.

Miesenbock, G., D. A. De Angelis, et al. 1998. Visualizing secretion and synaptic transmission with pH-sensitive green fluorescent proteins. *Nature* 394(6689): 192-195.

Millington, M., G. J. Grindlay, et al. 2007. High-precision FLIM-FRET in fixed and living cells reveals heterogeneity in a simple CFP-YFP fusion protein. *Biophys Chem* 127(3): 155-164.

Miyawaki, A., O. Griesbeck, et al. 1999. Dynamic and quantitative Ca²⁺ measurements using improved cameleons. *Proc Natl Acad Sci U S A* 96(5): 2135-2140.

Neher, R. and E. Neher. 2004. Optimizing imaging parameters for the separation of multiple labels in a fluorescence image. *J Microsc* 213(Pt 1): 46-62.

Neher, R. A. and E. Neher. 2004. Applying spectral fingerprinting to the analysis of FRET images. *Microscopy Research and Technique* 64(2): 185-195.

Ng, T., A. Squire, et al. 1999. Imaging Protein Kinase C Activation in Cells. *Science* 283(5410): 2085-2089.

Ogawa, H., S. Inouye, et al. 1995. Localization, trafficking, and temperature-dependence of the Aequorea green fluorescent protein in cultured vertebrate cells. *Proc Natl Acad Sci U S A* 92(25): 11899-11903.

Patterson, G. H., D. W. Piston, et al. 2000. Forster distances between green fluorescent protein pairs. *Anal Biochem* 284(2): 438-440.

Pawley, J. 2006. *Handbook of biological confocal microscopy*, Springer.

Periasamy, N., S. Bicknese, et al. 1996. Reversible photobleaching of fluorescein conjugates in air-saturated viscous solutions: singlet and triplet state quenching by tryptophan. *Photochem Photobiol* 63(3): 265-271.

Perrin, F. 1926. Polarisation de la lumière de fluorescence. Vie moyenne des molécules dans l'état excité. *J. Phys. Radium* 7(12): 390-401.

Perrin, F. 1933. Interaction entre atomes normal et activite. Transferts d'activation. Formation d'une moleculle activitee. . *Ann. Institut Poincare*(3): 279-318.

Peter, M., S. M. Ameer-Beg, et al. 2005. Multiphoton-FLIM quantification of the EGFP-mRFP1 FRET pair for localization of membrane receptor-kinase interactions. *Biophys J* 88(2): 1224-1237.

- Ponsioen, B., J. Zhao, et al. 2004. Detecting cAMP-induced Epac activation by fluorescence resonance energy transfer: Epac as a novel cAMP indicator. *EMBO Rep* 5(12): 1176-1180.
- Salonikidis, P. S., A. Zeug, et al. 2008. Quantitative measurement of cAMP concentration using an exchange protein directly activated by a cAMP-based FRET-sensor. *Biophys J* 95(11): 5412-5423.
- Sansom, D. M., C. N. Manzotti, et al. 2003. What's the difference between CD80 and CD86? *Trends Immunol* 24(6): 314-319.
- Sekar, R. B. and A. Periasamy. 2003. Fluorescence resonance energy transfer (FRET) microscopy imaging of live cell protein localizations. *J. Cell Biol.* 160(5): 629-633.
- Shaner, N. C., P. A. Steinbach, et al. 2005. A guide to choosing fluorescent proteins. *Nat Methods* 2(12): 905-909.
- Song, J., G. Hagen, et al. 2002. Interactions of the mast cell function-associated antigen with the type I Fcepsilon receptor. *Mol Immunol* 38(16-18): 1315-1321.
- Sorkin, A., M. McClure, et al. 2000. Interaction of EGF receptor and grb2 in living cells visualized by fluorescence resonance energy transfer (FRET) microscopy. *Curr Biol* 10(21): 1395-1398.
- Su, W. W. 2005. Fluorescent proteins as tools to aid protein production. *Microb Cell Fact* 4(1): 12.
- Sugiyama, Y., I. Kawabata, et al. 2005. Determination of absolute protein numbers in single synapses by a GFP-based calibration technique. *Nat Methods* 2(9): 677-684.
- Terrillon, S. and M. Bouvier. 2004. Roles of G-protein-coupled receptor dimerization. *EMBO Rep* 5(1): 30-34.
- Thaler, C., S. V. Koushik, et al. 2005. Quantitative multiphoton spectral imaging and its use for measuring resonance energy transfer. *Biophys J* 89(4): 2736-2749.
- Tramier, M., T. Piolot, et al. 2003. Homo-FRET versus hetero-FRET to probe homodimers in living cells. *Biophotonics, Pt A*. San Diego, Academic Press Inc. 360: 580-597.
- Van Der Meer, B. W., Cocker, I.G. and Chen, S. 1994. *Resonance Energy Transfer: Theory and Data*, VCH, New York
- van Rheenen, J., M. Langeslag, et al. 2004. Correcting confocal acquisition to optimize imaging of fluorescence resonance energy transfer by sensitized emission. *Biophys J* 86(4): 2517-2529.
- Varma, R. and S. Mayor. 1998. GPI-anchored proteins are organized in submicron domains at the cell surface. *Nature* 394(6695): 798-801.
- Veatch, W. and L. Stryer. 1977. The dimeric nature of the gramicidin A transmembrane channel: conductance and fluorescence energy transfer studies of hybrid channels. *J Mol Biol* 113(1): 89-102.
- Wallrabe, H. and A. Periasamy. 2005. Imaging protein molecules using FRET and FLIM microscopy. *Curr Opin Biotechnol* 16(1): 19-27.
- Weigert, F. 1920. *Verh. d. D. Ges.* 23(100).

Wlodarczyk, J., A. Woehler, et al. 2008. Analysis of FRET signals in the presence of free donors and acceptors. *Biophys J* 94(3): 986-1000.

Woehler, A., J. Wlodarczyk, et al. 2009. Specific oligomerization of the 5-HT1A receptor in the plasma membrane. *Glycoconj J* 26(6): 749-756.

Wolber, P. K. and B. S. Hudson. 1979. An analytic solution to the Forster energy transfer problem in two dimensions. *Biophys J* 28(2): 197-210.

Wouters, F. S., P. I. Bastiaens, et al. 1998. FRET microscopy demonstrates molecular association of non-specific lipid transfer protein (nsL-TP) with fatty acid oxidation enzymes in peroxisomes. *EMBO J* 17(24): 7179-7189.

Xia, Z. and Y. Liu. 2001. Reliable and global measurement of fluorescence resonance energy transfer using fluorescence microscopes. *Biophys J* 81(4): 2395-2402.

Yasuda, R., C. D. Harvey, et al. 2006. Supersensitive Ras activation in dendrites and spines revealed by two-photon fluorescence lifetime imaging. *Nat Neurosci* 9(2): 283-291.

Youvan, D. C., Silva, C.M., Bylina, E.J., Coleman, W.J., Dilworth, M.R., Yang, M.M. 1997. Calibration of Fluorescence Resonance Energy Transfer in Microscopy Using Genetically Engineered GFP Derivatives on Nickel Chelating Beads. *Biotechnology* 3: 1-18.

Zacharias, D. A., J. D. Violin, et al. 2002. Partitioning of lipid-modified monomeric GFPs into membrane microdomains of live cells. *Science* 296(5569): 913-916.

Zal, T. and N. R. Gascoigne. 2004. Photobleaching-corrected FRET efficiency imaging of live cells. *Biophys J* 86(6): 3923-3939.

Zhang, J., R. E. Campbell, et al. 2002. Creating new fluorescent probes for cell biology. *Nature Reviews Molecular Cell Biology* 3(12): 906-918.

7 Appendices

7.1 Appendix 1 – Abbreviations and symbols

Abbreviations

5-HT	5-hydroxytryptamine, Serotonin
AC	Adenylate cyclase
cAMP	Cyclic adenosine monophosphate
CD (i.e. CD28)	Cluster of differentiation
CFP	Cyan fluorescent protein
CV	Coefficient of variation
DPBS	Dulbecco's phosphate buffered solution
DMEM	Dulbecco's modified Eagle's medium
Epac	Exchange protein directly activated by cAMP
FCS	Fetal calf serum
FRET	Förster resonance energy transfer
GPCR	G protein coupled receptor
MAD	Microscope analog-digital units
SNR	Signal to noise ratio
TC	Tandem construct
TCSPC	Time correlated single photon counting
V	Volts
YFP	Yellow fluorescent protein

Symbols

f_A	ratio of FRET complexes over total acceptor, considering intact fluorophores only
f_D	ratio of FRET complexes over total donor, considering intact fluorophores only
f_a	fraction of acceptor-type molecules participating in complexes, irrespective of their labeling state
f_d	fraction of donor-type molecules participating in complexes, irrespective of their labeling state
[A]	concentration of free acceptor fluorophores

$[D]$	concentration of free donor fluorophores
$[DA]$	concentration of complexes carrying both intact donor and acceptor fluorophore
$[a], [d], [da]$	'chemical' concentrations of free acceptor, free donor and complexes, irrespective of their labeling state
$[A^{ref}]$	concentration of intact acceptor fluorophore in the calibration samples
$[D^{ref}]$	concentration of intact donor fluorophore in the calibration samples
$[A^t]$	total concentration of labeled acceptors with intact fluorophore
$[D^t]$	total concentration of labeled donor with intact fluorophore
$p_{a,tc}, p_{d,tc}$	labeling probabilities of donors and acceptors within the tandem construct
p_d'	abbreviation for $p_d \cdot p_{a,tc} / p_{d,tc}$ (see above)
α^i	apparent relative acceptor concentrations
δ^i	apparent relative donor concentrations
$F^i(\lambda)$	measured spectrum (linear combination of $F_D^{i,ref}$ and $F_A^{i,ref}$)
$F_A^{i,ref}$	reference fluorescence emission spectra of pure acceptor
$F_D^{i,ref}$	reference fluorescence emission spectra of pure donor
$r^{ex,i}$	scaling factor reflecting the excitation ratios of two fluorophores at the given excitation wavelength
E	characteristic FRET efficiency
E_{TC}	FRET efficiency of the tandem construct
K_d	dissociation constant
$\varepsilon_A^i, \varepsilon_D^i$	extinction coefficients of acceptor and donor
Q_A, Q_D	quantum yields of acceptor and donor
$e_A(\lambda), e_D(\lambda)$	standard emission spectra of the two fluorophores normalized to unit area
$I^{i,ref}$	excitation intensity
$\eta^i(\lambda)$	detection efficiencies of the instrument used

7.2 Appendix 2 – Full derivation of error propagation equations

Gaussian error propagation equations

Gaussian error propagation was used to define the variance of the luxFRET quantities, the emission ratio, and the ligand concentration. Using the original equation and derived variance the CV² of the quantities was solved.

Error propagation through equation 1.37: Derivation of equation 1.46

With

$$Ep_d' = R_{TC} \frac{\alpha^{(2)} - \alpha^{(1)}}{\alpha^{(1)} r^{ex,2} - \alpha^{(2)} r^{ex,1}}, \quad (A1)$$

we can define the variance of Ep_d' from Gaussian error propagation as,

$$\text{var}(Ep_d') = \frac{R_{TC}^2 (\Delta r)^2}{(\alpha^{(1)} r^{ex,2} - \alpha^{(2)} r^{ex,1})^4} \left((\alpha^{(2)})^2 \text{var}(\alpha^{(1)}) + (\alpha^{(1)})^2 \text{var}(\alpha^{(2)}) \right). \quad (A2)$$

By defining the squared coefficient of variation of each variable,

$$CV_{Ep_d'}^2 = \frac{\text{Var}(Ep_d')}{Ep_d'^2}, \quad CV_{\alpha^{(1)}}^2 = \frac{\text{Var}(\alpha^{(1)})}{(\alpha^{(1)})^2}, \quad \text{and} \quad CV_{\alpha^{(2)}}^2 = \frac{\text{Var}(\alpha^{(2)})}{(\alpha^{(2)})^2}. \quad (A3-5)$$

we can substitute the error propagation into CV² of Ep_d' and simplify to obtain the final form.

$$\begin{aligned} \text{var}(Ep_d') &= \frac{(R_{TC} \Delta r)^2}{(\alpha^{(1)} r^{ex,2} - \alpha^{(2)} r^{ex,1})^4} \left((\alpha^{(1)})^2 (\alpha^{(2)})^2 CV_{\alpha^{(1)}}^2 + (\alpha^{(1)})^2 (\alpha^{(2)})^2 CV_{\alpha^{(2)}}^2 \right) \\ \text{var}(Ep_d') &= \frac{(\alpha^{(1)} \alpha^{(2)} R_{TC} \Delta r)^2}{(\alpha^{(1)} r^{ex,2} - \alpha^{(2)} r^{ex,1})^4} (CV_{\alpha^{(1)}}^2 + CV_{\alpha^{(2)}}^2) \\ CV_{Ep_d'}^2 &= \frac{(\alpha^{(1)} \alpha^{(2)} R_{TC} \Delta r)^2}{(\alpha^{(1)} r^{ex,2} - \alpha^{(2)} r^{ex,1})^4} \cdot \frac{(\alpha^{(1)} r^{ex,2} - \alpha^{(2)} r^{ex,1})^2}{R_{TC}^2 (\alpha^{(2)} - \alpha^{(1)})^2} (CV_{\alpha^{(1)}}^2 + CV_{\alpha^{(2)}}^2) \\ CV_{Ep_d'}^2 &= \frac{(\alpha^{(1)} \alpha^{(2)} \Delta r)^2}{(\alpha^{(1)} r^{ex,2} - \alpha^{(2)} r^{ex,1})^2 (\alpha^{(2)} - \alpha^{(1)})^2} (CV_{\alpha^{(1)}}^2 + CV_{\alpha^{(2)}}^2) \end{aligned} \quad (A6)$$

Error propagation through equation 1.39: Derivation of equation 1.47

With

$$Ep_a = \frac{\frac{\alpha^{(i)}}{\delta^{(1)}} - R^t}{\frac{\alpha^{(i)}}{\delta^{(1)}} + r^{ex,i}}, \quad (A7)$$

we can define the variance of Ep_a from Gaussian error propagation as,

$$\text{var}(Ep_a) = \frac{(r^{ex,i} + R^t)^2}{(\alpha^{(i)} + \delta^{(1)} r^{ex,i})^4} \left((\delta^{(1)})^2 \text{var}(\alpha^{(i)}) + (\alpha^{(i)})^2 \text{var}(\delta^{(1)}) \right). \quad (A8)$$

By defining the squared coefficient of variation of each variable,

$$CV_{Ep_a}^2 = \frac{\text{Var}(Ep_a)}{Ep_a^2}, \quad CV_{\alpha^{(i)}}^2 = \frac{\text{Var}(\alpha^{(i)})}{(\alpha^{(i)})^2}, \quad CV_{\delta^{(1)}}^2 = \frac{\text{Var}(\delta^{(1)})}{(\delta^{(1)})^2}, \quad (A9-11)$$

we can substitute the error propagation into CV^2 of Ep_a and simplify to obtain the final form.

$$\text{var}(Ep_a) = \frac{(r^{ex,i} + R^t)^2}{(\alpha^{(i)} + \delta^{(1)} r^{ex,i})^4} \left((\delta^{(1)})^2 (\alpha^{(i)})^2 CV_{\alpha^{(i)}}^2 + (\delta^{(1)})^2 (\alpha^{(i)})^2 CV_{\delta^{(1)}}^2 \right)$$

$$\text{var}(Ep_a) = \frac{(r^{ex,i} + R^t)^2 (\delta^{(1)})^2 (\alpha^{(i)})^2}{(\alpha^{(i)} + \delta^{(1)} r^{ex,i})^4} (CV_{\alpha^{(i)}}^2 + CV_{\delta^{(1)}}^2)$$

$$\frac{\text{var}(Ep_a)}{Ep_a^2} = \frac{(r^{ex,i} + R^t)^2 (\delta^{(1)})^2 (\alpha^{(i)})^2}{(\alpha^{(i)} + \delta^{(1)} r^{ex,i})^4} \cdot \frac{\left(\frac{\alpha^{(i)}}{\delta^{(1)}} + r^{ex,i} \right)^2}{\left(\frac{\alpha^{(i)}}{\delta^{(1)}} - R^t \right)^2} (CV_{\alpha^{(i)}}^2 + CV_{\delta^{(1)}}^2)$$

$$CV_{Ep_a}^2 = \frac{(r^{ex,i} + R^t)^2 (\delta^{(1)})^2 (\alpha^{(i)})^2}{(\delta^{(1)})^4 \left(\frac{\alpha^{(i)}}{\delta^{(1)}} + r^{ex,i} \right)^2} \cdot \frac{1}{\left(\frac{\alpha^{(i)}}{\delta^{(1)}} - R^t \right)^2} (CV_{\alpha^{(i)}}^2 + CV_{\delta^{(1)}}^2)$$

$$CV_{Ep_d}^2 = \frac{(\alpha^{(i)})^2 (\delta^{(1)})^2 (r^{ex,i} + R^t)^2}{(\alpha^{(i)} + \delta^{(1)} r^{ex,i})^2 (\alpha^{(i)} - \delta^{(1)} R^t)^2} (CV_{\alpha^{(i)}}^2 + CV_{\delta^{(1)}}^2). \quad (A12)$$

Error propagation through equation 1.40: Derivation of equation 1.48.

With

$$Ep_d' = \frac{R_{TC}}{r^{ex,1}} \left(\frac{\alpha^{(1)}}{\alpha^{(2)}} - 1 \right), \quad (A13)$$

we can define the variance of Ep_d' from Gaussian error propagation as,

$$\text{var}(Ep_d) = \frac{R_{TC}^2}{(r^{ex,1})^2 (\alpha^{(2)})^4} \left((\alpha^{(2)})^2 \text{var}(\alpha^{(1)}) + (\alpha^{(1)})^2 \text{var}(\alpha^{(2)}) \right) \quad (A14)$$

By defining the squared coefficient of variation of each variable,

$$CV_{Ep_d}^2 = \frac{\text{Var}(Ep_d)}{Ep_d^2}, \quad CV_{\alpha^{(1)}}^2 = \frac{\text{Var}(\alpha^{(1)})}{(\alpha^{(1)})^2}, \quad \text{and} \quad CV_{\alpha^{(2)}}^2 = \frac{\text{Var}(\alpha^{(2)})}{(\alpha^{(2)})^2} \quad (A15-17)$$

we can substitute the error propagation into CV^2 of Ep_d' and simplify to obtain the final form.

$$\text{var}(Ep_d) = \frac{R_{TC}^2}{(r^{ex,1})^2 (\alpha^{(2)})^4} \left((\alpha^{(1)})^2 (\alpha^{(2)})^2 CV_{\alpha^{(1)}}^2 + (\alpha^{(1)})^2 (\alpha^{(2)})^2 CV_{\alpha^{(2)}}^2 \right)$$

$$\text{var}(Ep_d) = \frac{(\alpha^{(1)})^2 (\alpha^{(2)})^2 R_{TC}^2}{(r^{ex,1})^2 (\alpha^{(2)})^4} (CV_{\alpha^{(1)}}^2 + CV_{\alpha^{(2)}}^2)$$

$$CV_{Ep_d}^2 = \frac{(\alpha^{(1)})^2 (\alpha^{(2)})^2 R_{TC}^2}{(r^{ex,1})^2 (\alpha^{(2)})^4} \cdot \frac{(r^{ex,1} \alpha^{(2)})^2}{R_{TC}^2 (\alpha^{(1)} - \alpha^{(2)})^2} \cdot (CV_{\alpha^{(1)}}^2 + CV_{\alpha^{(2)}}^2)$$

$$CV_{Ep_d}^2 = \frac{(\alpha^{(1)})^2}{(\alpha^{(1)} - \alpha^{(2)})^2} (CV_{\alpha^{(1)}}^2 + CV_{\alpha^{(2)}}^2). \quad (A18)$$

Error propagation through emission ratio analysis

With

$$R = \frac{F_2}{F_1}, \quad (\text{A19})$$

we can define the variance of R from Gaussian error propagation as,

$$\text{Var}(R) = \left(\frac{F_2}{F_1^2} \right)^2 \text{var}(F_1) + \left(\frac{1}{F_1} \right)^2 \text{var}(F_2). \quad (\text{A20})$$

This simplifies to the form

$$CV_R^2 = CV_{F_1}^2 + CV_{F_2}^2. \quad (\text{A21})$$

Error propagation through ligand concentration estimation: Derivation of equation 1.51 (analogous to equation 1.50 for FRET efficiency).

With

$$X = K_d \left(\frac{R - R_o}{R_{\max} - R} \right) \frac{S_{f,2}}{S_{b,2}}, \quad (\text{A22})$$

we can define the variance of X from Gaussian error propagation as,

$$\text{Var}(X) = \left(K_d \frac{S_{f,2}}{S_{b,2}} \right)^2 \frac{(R_{\max} - R_o)^2}{\left(R_{\max} - \frac{F_1}{F_2} \right)^4} \left(\frac{\text{var}(F_1)}{F_2^2} + \frac{F_1^2 \text{var}(F_2)}{F_2^4} \right) \quad (\text{A23})$$

This simplifies to the form

$$CV_X^2 = \left(\frac{R}{(R - R_o)} \cdot \frac{(R_{\max} - R_o)}{(R_{\max} - R)} \right)^2 (CV_{F_1}^2 + CV_{F_2}^2). \quad (\text{A24})$$

Acknowledgements

I would like to express my sincerest gratitude to my supervisors Prof. Dr. Erwin Neher and Prof. Dr. Evgeni Ponimaskin, not only for the opportunity to perform this work, but also for their invaluable guidance, discussions, feedback, challenges, criticism, and support throughout its completion.

I would also like to thank Prof. Dr. D. Schild for his suggestions and help in steering this project from his position on my thesis committee. My many thanks go out to Prof. Dr. Michael Hörner and Ms. Sandra Drube for their help and support over my time in Göttingen. I am also grateful to the Study Committee of the Neurosciences program for the opportunity of performing my graduate studies in Göttingen.

I would like to thank the past and present members of the Department of Neuro and Sensory Physiology for the particularly positive working environment. I am grateful to Dr. Ute Renner, Dr. Andre Zeug, Gaby Klaen, and Dagmar Crzan for all the help over the past few years. I am especially grateful to Dr. Petrus Salonikidis, Dr. Jakub Wlodarczyk and Fritz Kobe for their close friendship and the frequent coffee breaks.

I am fortunate to have found myself studying, working, and living with among the most interesting and incredible people I have met. I owe a tremendous debt of gratitude to Natalia, Adema, Marija, Regis, Victorija, Achim and Katharina for the ceaseless encouragement and inspiration.

None of this would have been possible without my parents, Craig and Linda Danielson, my grandparents, Rodney and Margaret Danielson and my brother William. I am eternally grateful for their unquestioning love, unending sacrifice and constant support.

Curriculum Vitae

Education

2005 – Present **PhD Student - International Max Planck Research School - Neurosciences Graduate Program, Georg August University Göttingen, Germany.**

Quantitative analysis of Förster resonance energy transfer from spectral fluorescence measurements. Supervisors - Prof. Erwin Neher and Prof. Evgeni Ponimaskin

1999 – 2004 **B.S.E. Bioengineering - Harrington Department of Bioengineering, Arizona State University.** Magna Cum Laude, GPA 3.7.

Design and Development of a System for the Controlled Electrical Neural Stimulation of Epileptic Rats. Supervisor - Prof. Leon Iasemidis, ASU Brain Dynamics Lab, Barrow Neurological Institute.

Honors Thesis - Barrett Honors College, Arizona State University

Nonlinear Dynamical Systems and Chaos Theory Application to Human Physiology.

Professional Experience

2004 – 2005 Quality Engineer, General Electric Company, Bio-Sciences, Molecular Diagnostics, Chandler, AZ

2002 – 2003 Product Development Engineering Intern, Alliance Medical Corporation, Phoenix, AZ

2003 – 2004 Academic Tutor - Arizona State University, Learning Resource Center. Tempe, Arizona

2003 Program Coordinator - Arizona State University, Center for Outreach and Recruitment. Tempe, Arizona.

Awards

2006 – 2008 George-Christoph-Lichtenberg-Stipendium, awarded by the State of Lower Saxony, Germany

2005 – 2006 Graduate Stipend - International Max Planck Research School, Germany

1999 – 2004 Arizona Regents Scholarship and ASU Presidential Scholarships

Publications

Woehler A, Wlodarczyk J, Neher E. 2010. Signal to Noise Analysis of FRET-Based Sensors. *Submitted*.

Woehler A, Ponimaskin EG. 2009. G protein – mediated signaling: same receptor, multiple effectors. *Curr Mol Pharmacol* 2(3):237-48.

Woehler A, Wlodarczyk J, Ponimaskin EG. 2008. Specific oligomerization of the 5-HT1A receptor in the plasma membrane. *Glycoconj J*. 26(6):749-56.

Kobe F, Renner U, **Woehler A**, Wlodarczyk J, Papusheva E, Bao G, Zeug A, Richter DW, Neher E, Ponimaskin E. 2008. Stimulation- and palmitoylation-dependent changes in oligomeric conformation of serotonin 5-HT1A receptors. *Biochim Biophys Acta*. 1783(8):1503-16.

Wlodarczyk J, **Woehler A**, Kobe F, Ponimaskin E, Zeug A, Neher E. 2008. Analysis of FRET signals in the presence of free donors and acceptors. *Biophys J*. 94(3):986-1000.

Conference Presentations

Woehler A, Wlodarczyk J, Kobe F, Renner U, Neher E, Ponimaskin E. (2008) FRET Investigations of 5HT1A receptor Oligomerization using two wavelength excitation. Presentation given at 87th Annual Deutsche Physiologische Gesellschaft in the News and Notable from Young Physiologists Symposium. Cologne, Germany.

Woehler A, Wlodarczyk J, Zeug A, Neher E, Ponimaskin E. (2007) FRET Investigations of 5HT1A Receptor Oligomerization. Poster Presented at Focus on Microscopy 2007. Valencia, Spain.